Numerical Analysis of Interfacial Stress Distributions and Adhesion Behaviour of Fibrillar Surfaces

Dissertation

zur Erlangung des Grades

des Doktors der Ingenieurwissenschaften

der Naturwissenschaftlich- Technischen Fakultät III

Chemie, Pharmazie, Bio- und Werkstoffwissenschaften

der Universität des Saarlandes

von

Ram Gopal Balijepalli

Angefertigt am INM – Leibniz-Institut für Neue Materialien

Programmbereich Modellierung und Simulation

Saarbrücken

März 2016

Tag des Kolloquiums:	22. Juli 2016
Dekan:	Prof. Dr. -Ing. Dirk Bähre
Vorsitzender:	Prof. Dr. -Ing. Dirk Bähre
Berichterstatter:	Prof. Dr. Eduard Arzt Prof. Dr. Stefan Diebels
Akad. Mitarbeiter:	Dr. -Ing. Michael Marx

Contents

Acknowledgements V

Abbreviations and symbols VI

Abstract XI

Kurzzusammenfassung XII

1 Introduction & motivation 1

2 Theoretical background 4

2.1 Stress-strain relations 4

2.2 Fracture mechanics 5

2.2.1 Energy approach 5

2.2.2 The stress intensity approach: 7

2.3 Introduction to the finite element method (FEM) 9

2.4 Plane strain approximation 10

2.5 Aim of the thesis 11

3 Numerical simulation of the edge stress singularity and the adhesion strength for compliant mushroom fibrils adhered to rigid substrates 13

3.1 Introduction 13

3.2 Analytical solution for the corner singularity 15

3.3 Results 22

3.3.1 Mushroom fibril 22

3.4 Adhesion strength 31

3.5 Discussion 41

3.5.1 Improved shape for a fibril having a mushroom cap 44

3.6 Conclusion 49

4 Adhesion and stress singularities for composite fibrils with soft tip layers 51

4.1 Introduction 51

4.2 Numerical and experimental methods 53

4.2.1 Numerical simulations 53

4.2.2 Fibril fabrication 55

4.2.3 Adhesion experiments 57

4.3 Results 57

4.3.1 Numerical results 57

4.3.2 Adhesion strength 69

4.3.3 Experimental results 72

4.4 Discussion 73

4.5 Conclusion 76

Appendix A: Asymptotic analysis of the stress in a stiff adherent axisymmetric cylindrical fibril with a thin compliant layer at its tip 77

Appendix B: Plane strain and axisymmetric results 86

5 Summary 101

List of figures 104

List of tables 109

References 110

Acknowledgements

I am indebted to Prof. E. Arzt for his constant support, guidance, expertise and patience. I thank Prof. E. Arzt for offering me this work at INM-Leibniz Institute for New Materials, Saarbrucken, and for boosting up my morale throughout my thesis tenure. I am extremely thankful and express gratitude to Prof. R M. McMeeking, University of California, Santa Barbara (UCSB), for his guidance, valuable hints, suggestions and active involvement during the period of my thesis work. He has been a wonderful teacher who not only improved my understanding of mechanics but also had a positive impact on my personality. I thank Prof. M. Begley, University of California, Santa Barbara (UCSB) for allowing me to use the facilities of his department and for helping me during my research visit to UCSB. I would like to extend my gratitude to Dr. R. Hensel for supporting me in the last years and his involvement in steering the project. I express my heartfelt thanks to Dr. E. Kroner, Dr. A. Schneider and Dr. G. Nathalie for their encouragement. I would also thank Dr. S.N. Khaderi for his help in setting up the model and the discussions. I would like to acknowledge S.C.L. Fischer for performing the experiments. I would like to thank GRADUS, Faculty 8.4. Natural Sciences, of Saarland University for partially funding my research visit to the University of California, Santa Barbara. All this would not have been possible without the help of Prof. R. Bennewitz, who has opened the doors for my PhD journey at INM. I acknowledge the kind help of Dr. N. Goswami for referring me to INM. I thank M. Groh and Dr. K. Kruttwig for their help in writing abstract in German.

My PhD journey wouldn't have been so exciting without wonderful INM colleagues, office mates and friends whom I would like to thank. I take this occasion to thank my dearest friends Balakrishna and Novaf who were always there through the ups and downs of my journey.

Last but not the least, I am obliged to my parents R. P. Balijepalli and S. V. S Balijepalli, my brother S. K. Balijepalli and my late grandparents without whose blessings and love I would not have been what I am today. I would also like to acknowledge my parents in law (G. J. Yanamandra and S. Komerla) for their motivation and support. I must acknowledge my wife Archana; without her love and motivation I would not have finished this thesis. I am grateful to my Grandfather (Mr. AV.L Das) who believed in me and encouraged me right from my early years. Finally I take this opportunity to thank all my friends for their support and help.

Abbreviations and symbols

$3D$	Three dimensional
$2D$	Two dimensional
FEM	Finite element method
PDMS	Polydimethylsiloxane
MPa	Mega Pascal
kPa	Kilo Pascal
FI	Flat interface
CI	Circular interface
EI	Elliptical interface
SHP	Straight homogeneous punch
CPE4RH	Linear quadrilateral hybrid elements for plane strain
CAX4RH	Linear quadrilateral hybrid elements for axial symmetry
PEGdma	Poly(ethyleneglycol) dimethacrylate
PU	Polyguss

σ	Normal stress
$\sigma_x, \sigma_y, \sigma_z$	Normal stress in respective direction x, y and z
ε	Normal strain
$\varepsilon_x, \varepsilon_y, \varepsilon_z$	Normal strain in respective direction x, y and z
τ, τ_{xy}	Shear stress
γ	Shear strain
$\gamma_{xy}, \gamma_{yz}, \gamma_{zx}$	Shear strains in respective direction planes
E	Young's modulus
ν	Poisson's ratio
G	Energy release rate
G_C	Critical Energy release rate
$2a$	Crack length
σ_f^2	Failure stress
a_C	Critical crack length
P	Applied load
K_I, K_{II}	Mode I and Mode II stress-intensity factors

K_{IC}	Critical stress intensity
B	thickness
H_1	Amplitude of singularity
X_1, X_2	Directions
σ_{22}	Normal stress
σ_{12}	Shear stress
r	distance from the fibril edge
σ_A	Applied stress
D	Diameter of the stalk
D_f	Diameter of the mushroom flange
σ_I	Average interface stress
a_1	Calibration coefficient of straight punch
$\tilde{a}$	Calibration coefficient of mushroom fibril
h	Thickness of mushroom cap
ζ	Distance from the crack tip
l	length of defect

W	Adhesion energy
S^I	Adhesive strength of mushroom fibril
S^{punch}	Adhesive strength of straight punch
S^C	Cohesive Strength
S^S	Adhesion strength for edge initiated detachment
S_C^S	Cohesive Strength with an arbitrary position
σ_{Peak}	Peak stress
k	Stress concentration factor
S^P	Predicted strength
$\bar{S}^I$	Adhesion strength for detachment initiated at the edge of the mushroom cap
$\bar{S}^P$	Adhesion strength for detachment caused by a defect at the location of high stress under the edge of the fibril stalk
$S^I/S^{punch}\ Wedge$	Adhesion strength for wedge shaped mushrooms fibrils
$\tilde{a}_{fillet}$	Calibration coefficient for mushrooms fibrils with fillet radius
S_{fillet}^I/S^{punch}	Adhesion strength for mushrooms fibrils with filet radius
R	Radius of curvature

E_1	Young's modulus of a stiff material
E_2	Young's modulus of a soft material
L	Total height of fibril
L_1	Height of stiff material
L_2	Height of soft material
A	Apparent contact area
μ	Shear modulus
$\tilde{r},\theta,\tilde{z}$	Cylindrical polar coordinates
$\tilde{\sigma}_{rr},\tilde{\sigma}_{\theta\theta},\tilde{\sigma}_{zz}$	Stress components in cylindrical polar coordinates
$\tilde{u}_r,\tilde{u}_z$	Axial displacements
$\tilde{p}$	Pressure
Δ	Upward displacement
$O(\delta)$	Deviatoric stress term
c_1	Constant

Abstract

The climbing abilities of geckos have inspired many researchers to develop reusable, reversible adhesives. The fabrication of such synthetic adhesives has been well investigated. However, a full theoretical description is still lacking.

The objective of the thesis is to improve the theoretical understanding of the mechanics of fibrillar adhesion and also to uncover the various factors influencing the adhesion of the compliant fibrils adhered to a rigid surface using finite element analysis. The effect of fibril geometry on the adhesion was examined. Straight punch and mushroom fibrils were examined numerically and it was found that mushroom fibrils show better adhesion compared to straight punch. Mushroom fibrils with higher stalk to cap ratio and smaller flap height show better adhesion when the corner singularity is considered as driving force for delamination. For these fibrils the detachment will begin from centre instead of corner. Some other shapes were also studied by introducing a fillet radius at the corner joining stalk and the cap.

We propose a novel composite fibril with a stiff stalk and a softer tip to replicate the benefits shown by mushroom fibrils but with reduced manufacturing complications. The influence of Young's modulus and tip height were studied along with different interfacial shapes joining the stiff stalk and soft tip. It is found that higher Young's modulus ratio and smaller soft tip height result in higher adhesion strength. The results support the rational optimization of synthetic micropatterned adhesives.

Kurzzusammenfassung

Geckos besitzen die Fähigkeit sich auf glatten sowie rauen Oberflächen fortzubewegen. Davon inspiriert sind wiederverwendbare, reversibel haftende Haftoberflächen Gegenstand aktueller Forschung. Die experimentelle Herstellung und Untersuchung solcher Haftoberflächen wurden zahlreich belegt, allerdings mangelt es an einer vollständigen theoretischen Beschreibung der zugrunde liegenden Haftmechanismen.

Ziel dieser Arbeit ist es, das theoretische Verständnis über die Kontaktmechanik fibrillärer Haftstrukturen zu vertiefen und den Einfluss der Gestaltung des Kontaktbereichs sowie die Variation von Materialeigenschaften auf die Adhäsion zu untersuchen. Hierfür wurde ein numerisches Modell entwickelt, um die Spannungsverteilung in der Kontaktfläche von elastischen Fibrillen auf einem steifen Substrat zu untersuchen. Es konnte festgestellt werden, dass Fibrillen mit einem verbreiterten Kontaktbereich, sogenannte Mushroom-Fibrillen, eine bessere Haftung im Vergleich zu Fibrillen ohne Verbreiterung aufweisen. Alternativ zur Querschnittsverbreiterung im Kontaktbereich wurde in dieser Arbeit eine neue Verbundfibrille entwickelt, die aus zwei unterschiedlich elastischen Materialien besteht. Der Einfluss des Elastizitätsmoduls und die Dicke der Schicht im Kontaktbereich wurden zusammen mit verschiedenen Grenzflächenkrümmungen, die das steifere mit dem weicheren Material verbindet, untersucht. Es wurde festgestellt, dass höhere Elastizitätsmodulverhältnisse und dünnere weiche Schichten im Kontaktbereich zu höheren Haftfestigkeiten führen. Die Ergebnisse dieser Arbeit unterstützen insgesamt die Optimierung von synthetischen mikrostrukturierten Haftoberflächen.

1 Introduction & motivation

Nature is a good source of knowledge and innovation: many researchers these days are getting inspired by the animals, birds and plants. The interest in developing biomimetic structures has enormously increased in the past fifteen years; this can be prominently seen in the fields of biology, materials science and robotics. A group of researchers from Massachusetts Institute of Technology (MIT) got inspired by the Cheetah's capability to run fast and adapt its spine according to the speed and body motion. They developed a moving four armed robot weighing 33 kg which can run at the speed of 22 km/h (Seok et al., 2015). Researchers from Virginia tech got the motivation from Moon Jelly and developed a robot which is capable of swimming by using its artificial muscles powered by a renewable energy source (Alex et al., 2013). MIT and RWTH Aachen improved the efficiency of a solar plant by 20% by changing the geometry of the solar panels similar to the layout of sunflower florets (Noone et al., 2012). The hydrophobicity or famously called lotus effect of several plant leaves caught the interest of researchers to develop water repellent coatings or sprays (Guo et al., 2008; Guo et al., 2005; Lafuma and Quere, 2003; Neinhuis and W., 1997).

Recently, much interest has been focused on the development of reusable, reversible adhesives using the physical mechanisms deployed on the feet of animals (beetles, flies, spiders and geckos etc.). Geckos have been at the centre of research on adhesion for two reasons; the first one is that geckos are the heaviest among the category of animals which can adhere to different surfaces. The heavier the animals are, the smaller are the setae which will allow them to increase the contact area, hence increasing the adhesion (Arzt et al., 2003). The second is that they have dry adhesion which means they leave no traces on the adhered body after detaching from the surface. Such natural dry adhesives consist of millions of hierarchically structured hairs and fibrils with sizes ranging from millimetre to nanometre, which enable them to adhere to a wide range of surfaces (Autumn et al., 2000). Arzt et.al (Arzt et al., 2002; Arzt et al., 2003), Jagota et.al (Jagota and Bennison, 2002; Jagota et al., 2000; Jagota and Hui, 2011) Autumn et.al (Autumn et al., 2006a; Autumn et al., 2000; Autumn et al., 2006b; Autumn and Peattie, 2002; Autumn et al., 2002) and others have done extensive research on this topic to understand the mechanism behind the gecko adhesion. Experiments revealed that either inter-molecular van der Waals forces

(Autumn et al., 2002) or surface capillary forces (Huber et al., 2005b) or both play a major role in the adhesion mechanism. Adhesion varies depending on several parameters like structural instabilities, misalignment of loads, tip geometry and backing layer thickness etc. Due to the flexibility shown by Polydimethylsiloxane (PDMS) in adapting to different surfaces it has frequently been used in the fabrication of the structures. The fabrication of such synthetic adhesives on the micrometre and nanometre scale is well established and different parameters such as structure aspect ratio, radius or cap shape are well investigated. Experimental investigations revealed that the patterned surfaces (Hui et al., 2004; Sitti and Fearing, 2003; Yurdumakan et al., 2005) exhibit better adhesion strength when compared to the unpatterned surfaces when tested against same glass substrate. The geometry of the fibril cap contributes most to the adhesion, which is dominated by mushroom caps (del Campo et al., 2007) followed by spherical and flat caps. The dimensions and the aspect ratio of fibrils play an important role in controlling the adhesion strength (Greiner, 2008; Greiner et al., 2007).

However, there is still a gap in theoretical models which is required for a better understanding of the adhesive interactions. Some researchers have developed analytical models to understand the mechanics of the gecko adhesion (Gao et al., 2005; Glassmaker et al., 2004; Glassmaker et al., 2005; Hui et al., 2004; Yao and Gao, 2006). Numerical simulations help us to improve the understanding and thanks to the modern computers have paved the way to computationally examine the complicated problems. There were some efforts by researchers to model the gecko adhesion: Spuskanyuk et.al (Spuskanyuk et al., 2008) presented the influence of shape on adhesion and detailed the reason for mushroom tips for showing better adhesion. Aksak et.al (Aksak et al., 2011) demonstrated the influence of aspect ratio on adhesion and in another study they presented on how the edge angle of the mushroom fibril caps influence the adhesion by using Dugdale cohesive zone model (Aksak et al., 2014). Carbone and Pierro (Carbone and Pierro, 2012) studied different mushroom cap geometries and suggested an optimal shape for better adhesion.

The aim of the thesis is to understand the influence of contact geometry and materials properties in improving adhesion. We use finite element analysis to solve for stresses, strains and deformations in compliant fibrils attached to a rigid substrate. The major findings of the thesis are discussed in the results section as mentioned below in the following format: In Chapter 2, the

basic concepts related to thesis are explained. In Chapter 3, a discussion on the influence of mushroom cap geometry (thickness and width) on stress singularity along the interface of the compliant fibril and the rigid substrate is presented. The remote stress σ_A was applied on the free end of the fibril and the stress distribution along the interface was calculated for straight punch (reference) and for mushroom fibrils. Abaqus V 6.11 (Abaqus6.11, 2011) was used for all the numerical simulations. In Chapter 4 we propose a new concept of using composite fibrils made of two materials with a stiff and a soft elastomer layer. It reduces the manufacturing difficulties involved in making of the mushroom fibrils as an alternative to enhance adhesion strength. Three different interfacial joining shapes of the stiff and soft elastomer within the composite structure were examined which includes flat, circular and elliptical interfaces. We have also checked the influence of Young's modulus ratio and thickness of each composite layer on adhesion. Finally, a comparison is made with some of the recent experimental results.

2 Theoretical background

2.1 Stress-strain relations

When structures or components are subjected to external forces (static, continuous, impact, fatigue and fluctuation etc.) internal forces will be generated. These loads will result in two important parameters called stress and strain. Depending on the type of loading, it can either be a tensile, compressive or shear loading. The strain which does not involve an angle change is called normal strain (ε) and the corresponding stress as normal stress (σ). When the normal load is replaced with tangential load it results in shear stress (τ) and shear strain (γ). The material is said to be elastic when it returns to its original shape upon removal of the load. Stress is proportional to strain in this elastic regime. This linear relation between stress and strain is described by Hooke's law. The simplest form of Hooke's law can be represented as follows.

$$\sigma = E \,.\, \varepsilon \qquad 2.1$$

where E is Young's modulus.

If a three dimensional ($3D$) body is subjected to normal load simultaneously in x, y and z directions, the resultant strains are represented as:

$$\varepsilon_x = \frac{1}{E}\left[\sigma_x - \nu\left(\sigma_y + \sigma_z\right)\right] \qquad 2.2$$

$$\varepsilon_y = \frac{1}{E}\left[\sigma_y - \nu(\sigma_x + \sigma_z)\right] \qquad 2.3$$

$$\varepsilon_z = \frac{1}{E}\left[\sigma_z - \nu(\sigma_x + \sigma_y)\right] \qquad 2.4$$

where ν is the Poisson's ratio, it is defined as the ratio of the transverse contraction to the longitudinal elongation when subjected to an external load with in the elastic limit.

These equations are valid for all the three-dimensional ($3D$) solids or bodies. It is very expensive to treat all bodies in $3D$ either analytically or computationally. In order to reduce the complexity

of the problem it is possible to reduce the $3D$ solid in to a two-dimensional $(2D)$ solid, which in turn saves time and resources.

2.2 Fracture mechanics

Fracture is a complicated procedure, which is a combination of material response to defects (cracks, voids etc.) ranging from micro to macro scale. Defects are one of the major setbacks which reduce the material strength under load; these defects can be formed for several reasons such as manufacturing defects, material impurities, surface defects, interfacial defects and mechanical defects etc. Fracture mechanics answers several questions about fracture and its dependency on material properties, external loading conditions etc. Applied stress, flaw size and fracture toughness are the three important variables in the fracture mechanics approach. The material offers resistance, which assists in restricting the extension of a crack. The crack will be arrested till the energy available for its growth reaches a certain value. There are two approaches to study the fracture, one is energy approach and the other is the stress intensity approach.

2.2.1 Energy approach

The energy approach was introduced in 1921 by Griffith (Griffith, 1921) which was further modified in 1956 by Irwin (Irwin and Naval Research Lab, 1956) to develop the concept of the energy release rate G. For a linear elastic material the change in potential energy in accordance with the crack is called the energy release rate. Let us consider an infinite plate under the influence of tensile load with a crack whose length is $2a$ as shown in Figure 2.1. The energy release rate is then given as follows:

$$G = \frac{\pi \sigma_A^2 a}{E} \qquad 2.5$$

σ_A = remotely applied stress,
a = half crack length,
G = Energy release rate,

G_C = Critical Energy release rate

At $G = G_C$ the above equation gives the critical combinations of stress and crack size for failure.

$$G_C = \frac{\pi \sigma_f^2 a_C}{E} \qquad 2.6$$

When G_C is constant the failure stress σ_f is dependent on crack length and changes with $1 / \sqrt{a}$

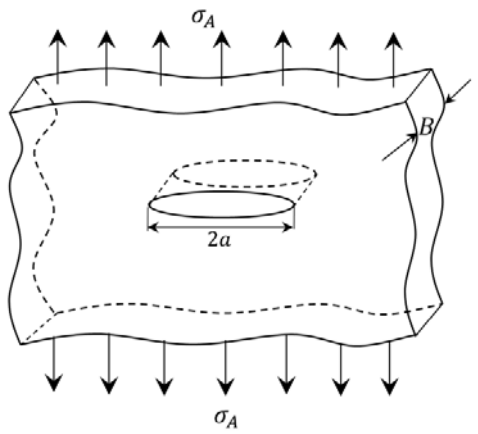

Figure 2.1: Penny crack in an infinite plate subjected to remote tensile load (Shi and Polycarpou, 2005).

From the strength of materials point of view which considers the relation between the load, stresses and materials parameters such as yield stress etc., the applied load will generate stresses in the body and will act as the driving force for the crack. In the fracture mechanics point of view, the energy release rate G is considered as the driving force for fracture, where G_C is the resistance offered by the material to fracture. In fracture mechanics, it is defined that the fracture toughness is a measure of critical energy release rate G_C and is independent of the size and geometry of the crack or the size of the body. The entire process is controlled by the driving force G as long as this assumption is valid. Only when the material is linear-elastic, it obeys the similitude assumption.

2.2.2 The stress intensity approach:

The work of Westergaard inspired Irwin to develop a single parameter which gives the relation between the stress and displacement near the crack tip. This parameter is now well known as stress-intensity factor 'K_I'. In Figure 2.2, the analysis of the crack tip along with the in-plane stresses acting on it is shown. All these stress components are proportional to K_I and can be characterized for a linear elastic material. The total stress distribution close to the crack tip can be calculated by using the equations:

$$\sigma_x = \frac{K}{\sqrt{2\pi r}} cos\frac{\theta}{2}\left[1 - sin\frac{\theta}{2} sin\frac{3\theta}{2}\right] \qquad 2.7$$

$$\sigma_y = \frac{K}{\sqrt{2\pi r}} \cos\frac{\theta}{2}\left[1 + \sin\frac{\theta}{2} \sin\frac{3\theta}{2}\right] \qquad 2.8$$

$$\sigma_{xy} = \frac{K}{\sqrt{2\pi r}} \sin\frac{\theta}{2}\left[\cos\frac{\theta}{2} cos\frac{3\theta}{2}\right] \qquad 2.9$$

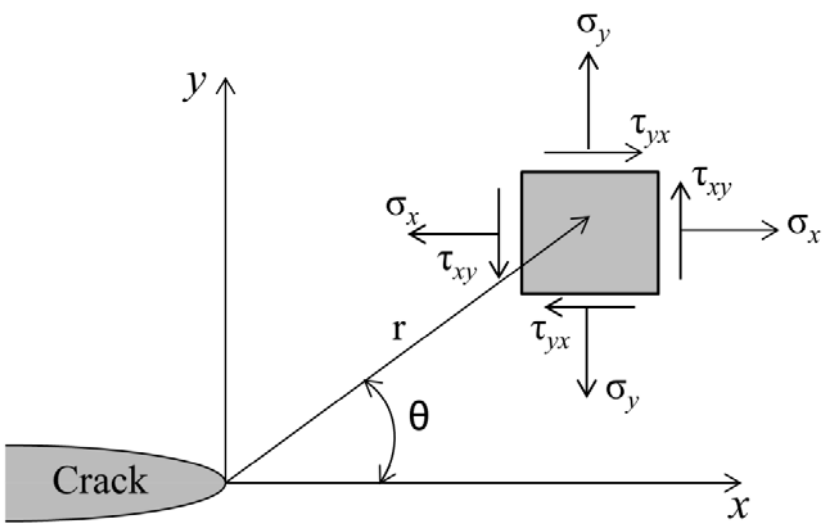

Figure 2.2: Stresses near the tip of a crack in an elastic material (Shi and Polycarpou, 2005)

Under the consideration that the material fails locally, the material has to fail at critical values of stress and strain. The point at which the material fails is called as critical stress intensity 'K_{IC}' and this can be correlated with the fracture toughness.

$$K_I = \sigma\sqrt{\pi a} \qquad 2.10$$

In other words, one can say that fracture occurs when $K_I = K_{IC}$ and a similar analogy can be drawn for driving force G and material resistance G_C to cracking as in energy approach for the stress intensity approach. In the stress intensity approach, the driving force is K_I and the resistance offered by the material is K_{IC}. It is assumed that K_{IC} is a material property which is independent of size. A comparison can be drawn between the energy approach G and the stress intensity approach K_I to obtain the relation between them. By comparing equations 2.5 and 2.10 it can be implied that

$$G = \frac{K_I^2}{E} \qquad 2.11$$

The critical energy release rate 'G_C 'and the critical stress intensity 'K_{IC}' also follow the same relation as the energy release rate 'G 'and stress intensity 'K_I'. For linear elastic materials, the energy approach and the stress intensity approach are equivalent. It is possible to predict the critical crack size which is necessary to disrupt the materials ability to withstand loads or in other words the crack size necessary to cause the complete failure of material. A safety factor can be employed to define the maximum allowable crack length.

2.3 Introduction to the finite element method (FEM)

Differential or integral equations are used to solve a lot of interesting engineering issues. It is not an easy task to find exact solutions to complicated models but approximate solutions are achievable in reasonable time by finite element methods (FEM) (Bathe, 1996; Chandrupatla and Belegundu, 2011; Reddy, 2005; Zienkiewicz and Taylor, 2000). FEM as the name suggests discretizes the continuum body into finite domains or small elements which are joined by nodes. Shape functions use algebraic expressions to interpolate the field variables within the element. Every such element is defined using a group of equations and each element has a finite degree of freedom. Combining such information of all the individual elements in the domain gives rise to the expressions for the global domain which has infinite degrees of freedom. The element size can be varied accordingly based on the amount of information necessary for the system. It is also possible to vary the size of the element (which is also called mesh size) within the domain so that more information can be extracted from the area of interest and computational time is saved without affecting the accuracy of the results. The elements can be chosen based on the complexity of the geometry and also whether the model is 2 dimensional ($2D$) or 3 dimensional ($3D$). Due to the advantages that FEM offers and the availability of computational power one can solve complicated engineering problems. Modern commercial FEM softwares have a user friendly graphic user interface and most of the steps can be performed automatically without much effort. Apart from dealing with linear problems it is also possible to solve nonlinear problems, for example large deformations, buckling and material non linearity etc.

2.4 Plane strain approximation

There are two different basic approximations in order to reduce the three-dimensional model to a two-dimensional one. They are plane strain and plane stress (Chandrupatla and Belegundu, 2011; Quek and Liu, 2003). I will be discussing only the plane strain approximation in this thesis.

Plane Strain: This model is valid in case of a thick body where one dimension is very much larger than the other. For example a three dimensional ($3D$) body, e.g. a cylinder, can be simplified by using a plane strain model. The body is cut by an imaginary section plane as shown in Figure 2.3 and that plane is considered as the newly simplified two dimensional ($2D$) model. This model works with certain approximations such as that the forces will not be acting normal to the section plane and the second assumption is that no strains will be developed normal to the simplified $2D$ plane.

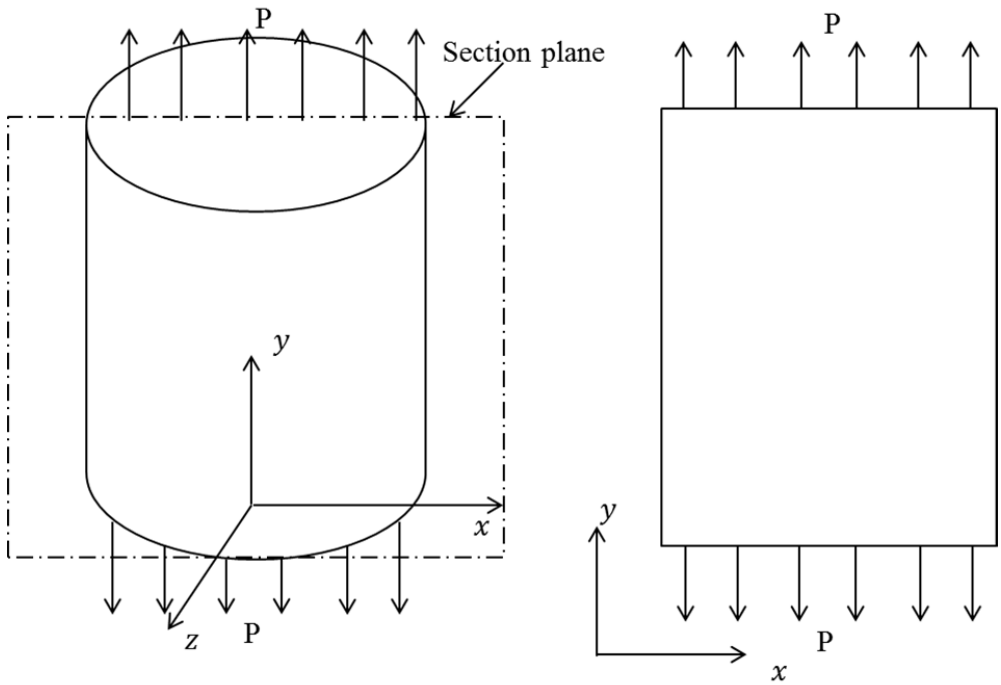

Figure 2.3: Plane strain approximation to simplify the three dimensional body (left) to a two dimensional body (right).

It is defined as a state of strain in which the strain normal to the $x - y$ plane, strain ε_z and the shear strains γ_{zx} and γ_{yz} are assumed to be zero. The plane strain analysis is a little more complex than the plane stress. Substituting $\varepsilon_z = 0$ in the $3D$ Hooke's law gives an expression for σ_z:

$$\sigma_z = \nu(\sigma_x + \sigma_y) \tag{2.12}$$

This can be substituted into the first two equations of the $3D$ Hooke's law to give expressions involving σ_x and σ_y only. The first equation of Hooke's law is simplified as

$$\varepsilon_x = \frac{1}{E'}(\sigma_x - \nu'\sigma_y) \tag{2.13}$$

$$\varepsilon_y = \frac{1}{E'}(\sigma_y - \nu'\sigma_x) \tag{2.14}$$

$$\varepsilon_z = 0 \tag{2.15}$$

where $E' = E/(1 - \nu^2)$, $\nu' = \nu/(1 - \nu)$.

The absence of forces in normal direction to the section plane will lead to zero force in the z direction i.e. shear strains $\gamma_{yz} = \gamma_{zx} = 0$. This means that the shear strain in xy plane (γ_{xy}) is non-zero is given as follows:

$$\gamma_{xy} = \frac{1}{G}\tau_{xy} \tag{2.16}$$

2.5 Aim of the thesis

Fabrication of the artificial adhesive structures has been experimentally investigated for many years by researchers and is very well established. Analytical models explain to some extent the mechanics behind the adhesion and the numerical studies improved this understanding but there is still some gap left. The aim of the thesis is to uncover the facts on how the adhesion strength is dependent on the geometry and material properties and how it can be improved by modifying the

geometry and the material properties of the fibrils. There is still a gap between the experimental results and the theoretical results. Some of these questions are explained in the following chapters:

In Chapter 3 we address the issue as to why the adhesive performance of a mushroom fibril is better than a straight punch.

- Why does the mushroom fibril adhere better than the straight punch?
- How does the height of mushroom cap influence the adhesive strength?
- How does the width of the mushroom cap influence the adhesive strength?
- How is the stress distributed along the mushroom cap?

It is also important to uncover the influence of the material properties on adhesive strength. In Chapter 4 the following questions are addressed:

- Can composite fibrils replicate the effect of mushroom fibril to improve adhesion strength?
- Do composite fibrils pave an alternative way to overcome the difficulties involved in the manufacturing process of mushroom fibrils?
- Does a gradient in Young's modulus have any influence on improving contact and adhesion strength?
- Does the tip height of soft elastomer influence the distribution of the stress and adhesion strength?
- Does the shape of the joining interface of the composite fibrils influence the adhesion strength?

In Chapter 5 a summary of the thesis will be provided.

3 Numerical simulation of the edge stress singularity and the adhesion strength for compliant mushroom fibrils adhered to rigid substrates[1]

3.1 Introduction

Animals in nature possess different hairy contact structures such as straight punches, spherical and conical caps, toroidal suction cups, etc. The climbing abilities of geckos have inspired many researchers to develop reusable, reversible adhesives. Gecko feet are covered with millions of hierarchically structured hairs or setae with sizes ranging from millimetres to nanometres (Autumn et al., 2000; Gorb, 2007; Hiller, 1968). The smallest level of hierarchical structure is patterned with finer fibrils; these observations suggest that finer fibrils are associated with better adhesion (Arzt et al., 2003). This insight has led to formulation of the concept of "contact splitting" (Arzt et al., 2003). The present group (Huber et al., 2007; Huber et al., 2005a; Huber et al., 2005b; Huber et al., 2008; Orso et al., 2006), as well as Autumn et al. (Autumn et al., 2006a; Autumn et al., 2002; Jin et al., 2012) and Jagota et al. (Jagota and Bennison, 2002; Jagota et al., 2000) have done extensive research on this topic to understand the mechanism behind gecko adhesion. Experiments reveal that either intermolecular van der Waals forces (Autumn et al., 2002) or capillary forces (Huber et al., 2005b) play a major role in the adhesion mechanism.

Polydimethylsiloxane (PDMS) is one of the most widely used materials for the fabrication of gecko inspired adhesives. PDMS has a Poisson's ratio close to 0.5 and a Young's modulus ranging from approximately 100 kPa to approximately 10 MPa, depending on the amount of crosslinking. It is chemically inert, non-toxic and during preparation hardens quickly at elevated temperatures. It has been experimentally proven that PDMS surfaces patterned with fibrils offer

---

[1] This chapter was published as a paper: R.G. Balijepalli, M.R. Begley, N.A. Fleck, R.M. McMeeking, E. Arzt, Numerical simulation of the edge stress singularity and the adhesion strength for compliant mushroom fibrils adhered to rigid substrates International Journal of Solids and Structures 85–86, 160-171. http://dx.doi.org/10.1016/j.ijsolstr.2016.02.018
The contributions of the authors were as follows:
- I have participated in planning the project, performed all simulations and wrote the paper.
- R. M. McMeeking was involved in planning the project, gave valuable support throughout the work.
- M.R. Begley provided his valuable feedback to the contents.
- Prof. N. Fleck has contributed to an improvement of the paper and his valuable insights on corner singularity.
- Prof. E. Arzt as the supervisor of my thesis, participated in planning, discussing results and writing the paper.

better adhesion against a stiff smooth substrate than an unpatterned PDMS surface (Greiner et al., 2007; Hui et al., 2004; Sitti and Fearing, 2003; Yurdumakan et al., 2005).

Experiments with artificial patterned structures have shown that contact cap shape plays an important role in improving adhesion; compared to several different contact geometries, the mushroom fibril has generally been found to adhere best (del Campo et al., 2007; Gorb et al., 2007b; Greiner et al., 2007; Kim and Sitti, 2006). Adhesion also depends on other phenomena such as structural instability due to fibril buckling when they are compressed axially (Paretkar et al., 2013), misalignment of the adhering surfaces , surface roughness (Canas et al., 2012; Huber et al., 2007; Persson and Gorb, 2003; Persson and Tosatti, 2001) and backing layer thickness (Kim et al., 2007; Long et al., 2008). In most of the experiments exploring the adhesion of such patterned surfaces, compliant fibrils are pressed against a stiff spherical substrate and adhesive strength is measured during subsequent tensile loading. The fabrication and experimental exploration of such synthetic adhesives at the micrometre and nanometre scale are well established in the laboratory setting, and different parameters such as structure aspect ratio, fibril size and cap shape are well investigated. However, there is still a lack of theoretical models required for a better understanding of the adhesive interactions. The purpose of the present paper is to fill some of the gaps.

There have been on-going efforts by several researchers in the past years to understand the details of gecko adhesion through the development of various analytical models (Gao et al., 2005; Glassmaker et al., 2004; Glassmaker et al., 2005; Hui et al., 2004; Yao and Gao, 2006) and numerical simulations (Aksak et al., 2011; Aksak et al., 2014; Carbone and Pierro, 2012; Khaderi et al., 2015; Spuskanyuk et al., 2008). Spuskanyuk et al. (Spuskanyuk et al., 2008) addressed the influence of shape on adhesion and detailed the reason why mushroom fibrils show better performance than simple punch shapes. Aksak et al. (Aksak et al., 2011) demonstrated the influence of mushroom aspect ratio on adhesion, and Aksak et al. (Aksak et al., 2014) used a Dugdale cohesive zone model for mushroom like fibrils to predict the optimal shape for adhesion. They found that adhesion depends on the edge angle and the ratio of stalk radius to the outer fibril radius. Carbone and Pierro (Carbone and Pierro, 2012) have calculated the dependence of adhesive performance on the mushroom cap geometry and suggested an optimal shape for adhesion. Khaderi et al. (Khaderi et al., 2015) provided a detailed analysis of the corner

stress singularity at the edge of the fibril, its influence on the stress intensity factor for a small interface detachment near that edge, and the resulting influence on the detachment strength for a single compliant flat bottomed cylindrical fibril attached to a compliant or a rigid substrate.

In this work, we consider the corner stress singularity at the edge of a perfectly bonded compliant mushroom fibril on a rigid substrate where sliding of the fibril relative to the substrate is forbidden. In particular, we investigate how the mushroom cap geometry, including its thickness and diameter, influences the adhesive strength. We follow the approach introduced by Akisanya and Fleck (Akisanya and Fleck, 1997) to describe the corner stress singularity to explore the mechanics of detachment of $2D$ and $3D$ fibrils, thus extending the work of Khaderi et al. (Khaderi et al., 2015) to mushroom caps. To evaluate the parameters of the corner stress singularity, we use finite element analysis, utilizing the commercial finite element software Abaqus (Abaqus6.11, 2011), to solve for the stresses, strains and deformations in compliant fibrils adhered to a rigid substrate as shown in Figure 3.1.

3.2 Analytical solution for the corner singularity

We consider a compliant fibril adhered to a rigid substrate without any interfacial crack. The fibril is treated as an incompressible, isotropic elastic solid, and the edge of the fibril always meets the substrate at right angles. The fibril material is forbidden to slide on the substrate at the interface between them. The boundary condition on the compliant material at the interface with the substrate is therefore one where the displacement is zero. When a tensile load is applied to the fibril as shown in Figure 3.1, there will be a stress singularity at the fibril edge where it touches the substrate (Akisanya and Fleck, 1997). We treat both a straight punch fibril without (Figure 3.1 (a)) and with a mushroom cap (Figure 3.1 (b)). In the current paper we focus on this corner stress singularity to determine its strength and amplitude for the fibrils (straight punch and mushroom shape) shown in Figure 3.1. Studies have been performed both for plane strain ($2D$) and axisymmetric cylindrical ($3D$) geometries. In addition, we provide a few results for a variation on the shape shown in Figure 3.1.

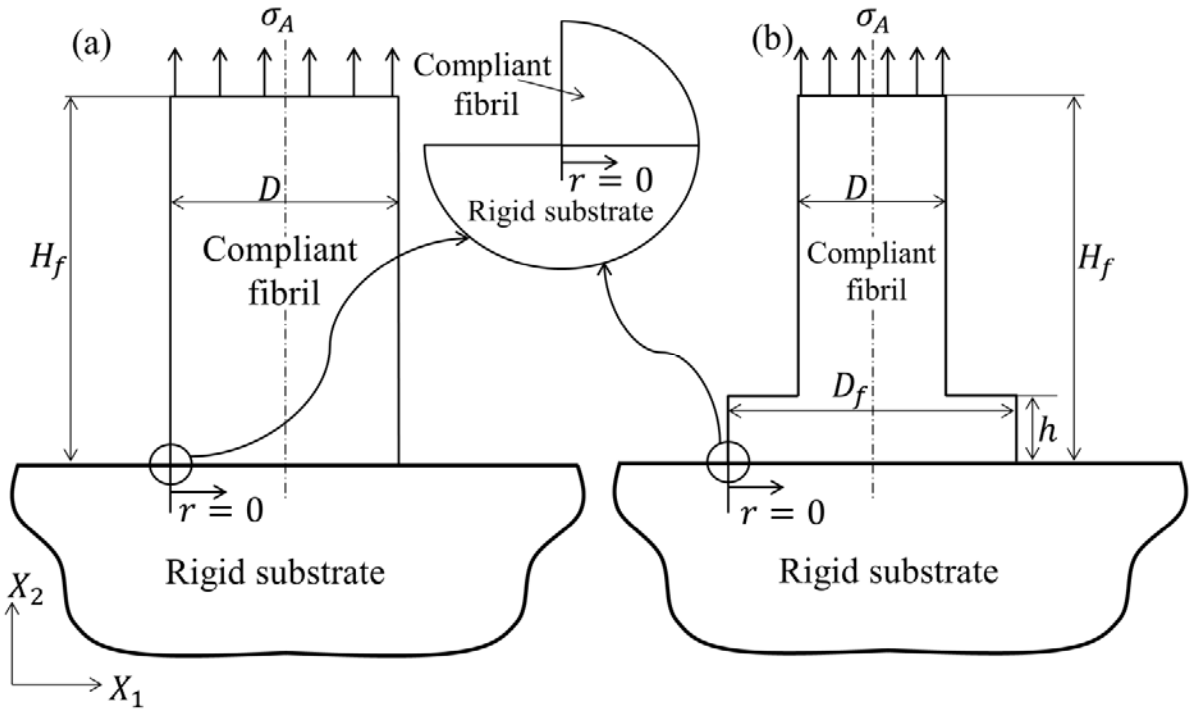

Figure 3.1: Schematics of (a) a straight punch shaped fibril without a mushroom cap and (b) a fibril with a mushroom cap, both adhered to a rigid substrate.

We adopt the method of Akisanya and Fleck. (Akisanya and Fleck, 1997) and Khaderi et al.(Khaderi et al., 2015). The most singular terms in the asymptotic normal (σ_{22}) and shear (σ_{12}) stress components along the interface between a compliant fibril and a rigid substrate (Khaderi et al., 2015) are

$$\sigma_{22} = H_1 r^{-0.406} \qquad 3.1$$

$$\sigma_{12} = 0.505\, H_1 r^{-0.406} \qquad 3.2$$

where r is the distance from the fibril edge, and the directions X_1 and X_2 are shown in Figure 3.1. The amplitude H_1 can be written in terms of the applied stress and one relevant dimension of the fibril. We choose the average stress, σ_I, on the interface between the fibril and the substrate

as the measure of the applied stress and the width or diameter, D_f, of the mushroom flange as the relevant dimension and obtain

$$H_1 = \sigma_I D_f^{0.406} \tilde{a} \qquad 3.3$$

where $\tilde{a}$ is a dimensionless calibration parameter that depends on the geometry of the fibril, including whether it is plane strain or axisymmetric. The amplitude of the singularity scales directly with $\tilde{a}$ as shown in Equation 3.3. We will show that $\tilde{a}$ controls detachment processes at the edge of fibril and that a low value is beneficial for good adhesion. For a mushroom cap fibril, the average interface stress, σ_I, is written as $\sigma_I = \sigma_A\, D/D_f$ for a plane strain slab and $\sigma_I = \sigma_A \left(D/D_f\right)^2$ for axial symmetry, where σ_A is the stress applied to fibril stalk. Note that when the fibril is a plane strain slab, D_f is the width of the mushroom cap and D is the width of the stalk, whereas in the axisymmetric cylinder case D_f is the diameter of the mushroom cap and D is the diameter of the stalk. For convenience we will refer to these parameters throughout as the diameter of the mushroom flange and the stalk even when discussing the plane strain results. We note that in the case of a straight punch without a mushroom cap, $D_f = D$, $\sigma_I = \sigma_A$ and $\tilde{a} = a_1$, where the straight punch is illustrated in Figure 3.1(a), and a_1 is the calibration parameter utilized by Khaderi et al. (Khaderi et al., 2015).

In order to verify our computational methods, we repeat the calculations of Khaderi et al (Khaderi et al., 2015) for the straight punch attached to a rigid substrate. For the finite element mesh we use a total of 123374 and 100501 linear quadrilateral hybrid elements for plane strain (Abaqus terminology element CPE4RH) and axial symmetry (Abaqus terminology element CAX4RH), respectively. A very fine mesh was used close to the corner of the compliant fibril to increase the accuracy of the results there. The finite element results for the normal and shear stress at the interface are plotted in logarithmic form (base 10) in Figure 3.2 for both the plane strain and axisymmetric cases and marked "FEM". According to Khaderi et al. (Khaderi et al., 2015) $a_1 = 0.331$ for the plane strain punch and $a_1 = 0.278$ for the axisymmetric one. In logarithmic form (base 10), the asymptotic solutions for the plane strain case is thus

$$\log(\sigma_{22}/\sigma_A) = -0.480 - 0.406\, log\, (r/D)$$

and

$$\log(\sigma_{12}/\sigma_A) = -0.777 - 0.406 \log(r/D).$$

For axial symmetry it is

$$\log(\sigma_{22}/\sigma_A) = -0.556 - 0.406 \log(r/D)$$

and

$$\log(\sigma_{12}/\sigma_A) = -0.853 - 0.406 \log(r/D)$$

These 4 results are plotted in Figure 3.2 (a) for plane strain and Figure 3.2 (b) for axial symmetry and marked "asymptotic stress." It can be seen that our finite element results agree very well with the asymptotic solution, thereby verifying the accuracy of our computational method.

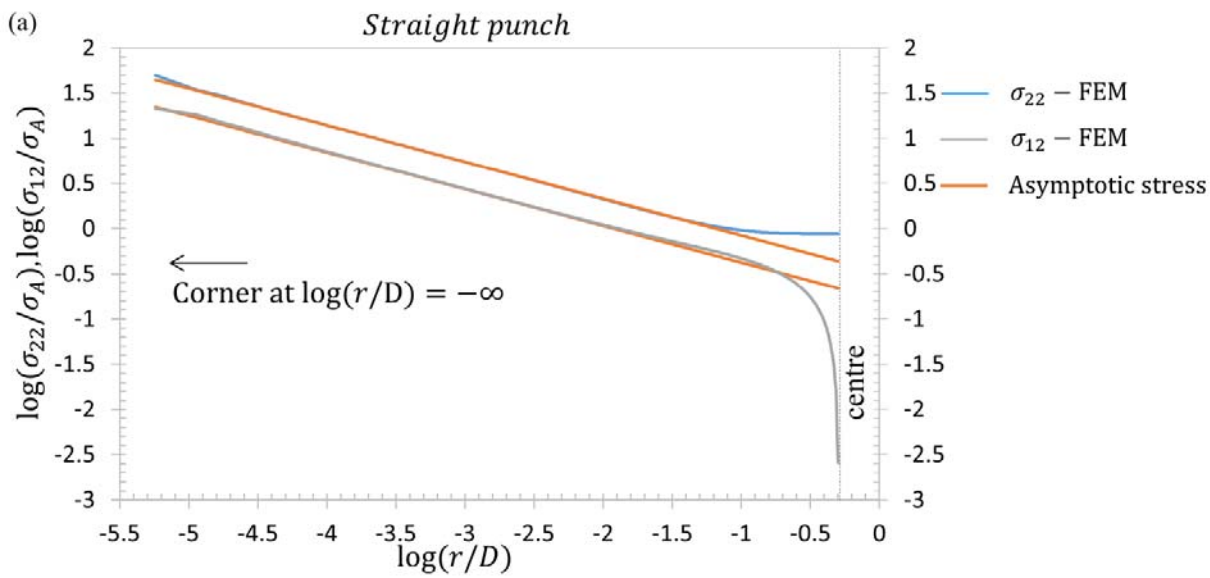

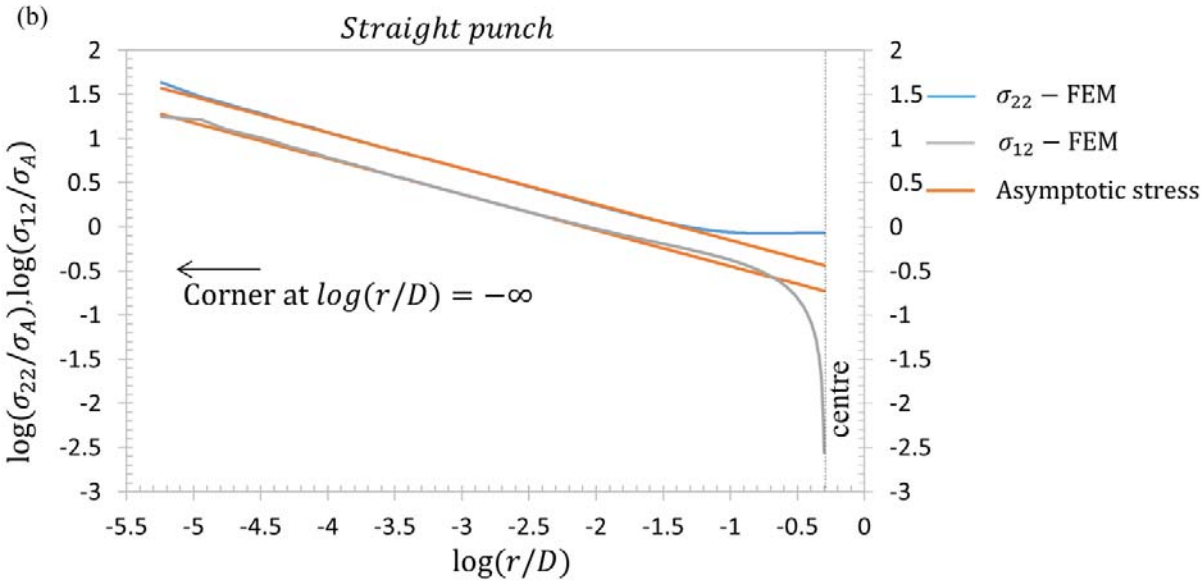

Figure 3.2: Normalised normal (σ_{22}) and shear (σ_{12}) tractions for the straight punch (corner to centre) for (a) plane strain and (b) axial symmetry. The remote applied stress is denoted by σ_A.

With our computational method verified, we concentrate on the corner stress singularity for mushroom fibrils. With the mushroom cap diameter, D_f, held fixed we vary the diameter, D, of the fibril stalk to ascertain the influence of the ratio D_f/D. By proceeding in this way we are able to maintain element structure and size in the finite element mesh adjacent to the interface with the rigid substrate, where the accuracy of the results is most important. The same element types are used for mushroom capped fibrils as are utilized for the straight punches, and between $100{,}000$ and $500{,}000$ elements are used in the finite element models. For each value of D the thickness, h, of the mushroom cap is varied and more than 100 geometric configurations are studied through finite element solutions to quantify the amplitude, $\tilde{a}$, of the corner singularity in each case. The mesh close to the edge of the fibril is always very fine, ensuring the accuracy of the information there in the finite element solutions.

3.2.1.1 Predicting the adhesive strength

We now postulate that there is a small detachment or defect of length l at the edge of the fibril as seen in Figure 3.3 such that the corner stress singularity controls its behaviour.

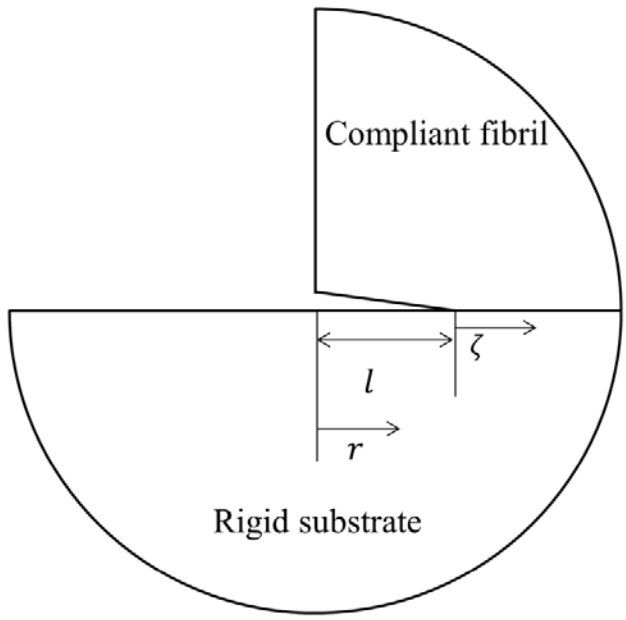

Figure 3.3: Schematic of a small crack along the interface at the corner of the contact.

This detachment can represent in an approximate manner the presence of an edge radius on the fibril due to the shape of the mould in which the fibril is formed. Such a detachment is equivalent to an interface crack having a stress singularity at its front, characterized by Mode I and Mode II stress intensity factors, K_I and K_{II} respectively, such that on the interface ahead of the detachment tip the leading order asymptotic stresses are given by

$$\sigma_{22} = \frac{K_I}{\sqrt{2\pi\zeta}} \text{ and } \sigma_{12} = \frac{K_{II}}{\sqrt{2\pi\zeta}} \qquad 3.4$$

where ζ is the distance from the crack tip as shown in Figure 3.3. The constants necessary to compute the stress intensity factors are adopted from Khaderi et al. (Khaderi et al., 2015) and result in

$$K_I = 2.6H_1 l^{0.094} = 2.6\sigma_I D_f^{0.406}\tilde{a}l^{0.094} \qquad 3.5$$

$$K_{II} = 0.8H_1 l^{0.094} = 0.8\sigma_I D_f^{0.406}\tilde{a}l^{0.094} \qquad 3.6$$

We thus see that at a given location ahead of the detachment, the normal stress is 3.25 times the shear stress, showing that the detachment process is dominated by tension and is therefore almost a Mode I phenomenon. Upon detachment, the energy release rate is

$$G = \frac{1-v^2}{2E}\,(K_I^2 + K_{II}^2) = \frac{3}{8E}(K_I^2 + K_{II}^2) = \frac{2.8\sigma_I^2 D_f^{0.81} l^{0.19}\tilde{a}^2}{\mathrm{E}} \qquad 3.7$$

where E is Young's modulus and v is Poisson's ratio, equal to 0.5 consistent with incompressibility. For detachment initiated at the edge to occur, the energy release rate must be equal to the adhesion energy, W. The value of the latter should be chosen to be consistent with the mode mixity, i.e. the ratio K_{II}/K_I; however, the mixity is the same for all shapes and sizes of fibrils, so the dependence of the adhesion energy on mode mixity will not affect the relative adhesion strength of fibrils having different configurations. Furthermore, since detachment is nearly Mode I, it will be reasonably accurate to use the adhesion energy for purely tensile detachment as the value for W. When we set $G = W$ in equation 3.7, the stress, σ_I, is then equal to the interface strength, S^I, for edge initiated fibril detachment. This strength is thus given by

$$S^I = \frac{0.6\sqrt{EW}}{D_f^{0.406} l^{0.094}\tilde{a}} \qquad 3.8$$

The ratio of strengths of fibrils having the same diameter of mushroom cap and the same edge detachment length is therefore inversely proportional to the ratio of amplitudes of their stress singularities at the fibril edge. Specifically, when a straight punch fibril of diameter $D = D_f$ is compared ceteris paribus with one having a mushroom cap of diameter D_f, their strength ratio for edge initiated detachment is given by

$$\frac{S^I}{S^{punch}} = \frac{a_1}{\tilde{a}} \qquad 3.9$$

where, as noted above, a_1 is the calibration parameter quantified by Khaderi et al.(Khaderi et al., 2015) for the straight punch and S^{punch} is the adhesive strength of the straight punch.

3.3 Results

3.3.1 Mushroom fibril

Figure 3.4 depicts the stress distributions at the interface between a rigid substrate and a fibril with a mushroom cap where the cap diameter is twice that of the stalk ($D_f/D = 2$) and the ratio of the mushroom cap thickness to its diameter (h/D_f) is 0.008. Results are shown both for plane strain (Figure 3.4 (a)) and axial symmetry (Figure 3.4(b)). It is seen that the stresses at the corner are reduced compared to the results in Figure 3.2 at the same distance from the corner, while higher stress magnitudes now appear close to the centre of the fibril. This latter feature is somewhat misleading as the region near the corner has a stress singularity and thus there are extremely high stresses there, but not apparent on the scale encompassed by Figure 3.4. Nevertheless, the fact that the stresses at the fibril centre appear to be the largest present when Figure 3.4 is considered emphasises that the mushroom cap has reduced the amplitude of the corner singularity considerably. Again good agreement with the asymptotic analytical solution is found, except near the fibril centre where the numerical stresses deviate strongly. This indicates that the corner singularity is not dominant at the fibril centre. The calibration coefficient, $\tilde{a}$, is extracted from the finite element stress solutions for the normal stress, σ_{22}, by fitting it to the asymptotic formula in logarithmic (base 10) form $log(\sigma_{22}/\sigma_I) = log\tilde{a} - 0.406\log(r/D_f)$. The particular mushroom fibril shape shown in Figure 3.4,has calibration coefficient of $\tilde{a} = 1.3 \times 10^{-10}$ for a $2D$ plane strain fibril and $\tilde{a} = 1.6 \times 10^{-10}$ for the $3D$ axisymmetric fibril.

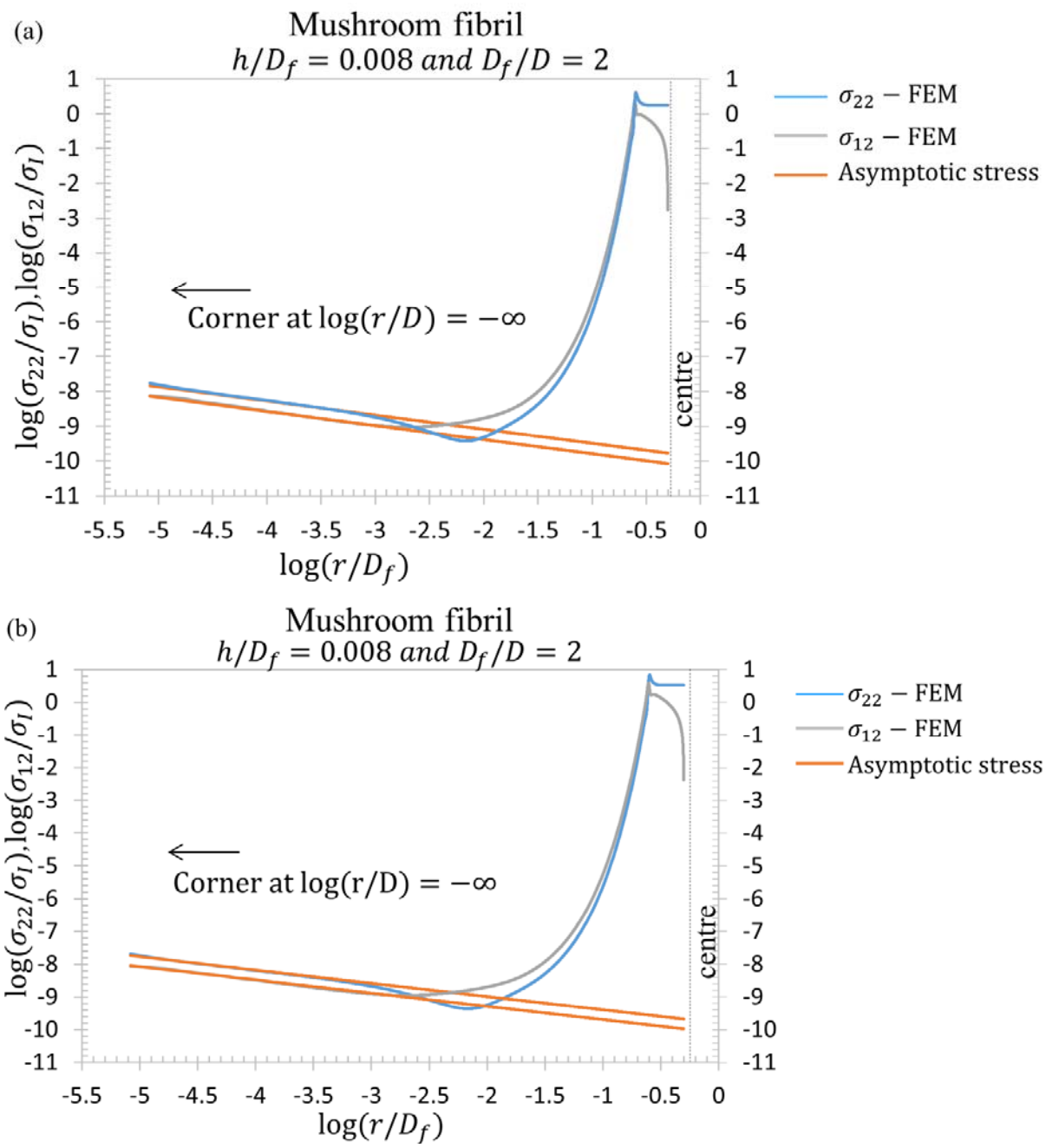

Figure 3.4: Comparison of the finite element results and the theoretical asymptotic results for the normal and shear tractions on the interface between the substrate and a specific mushroom capped fibril. The results are plotted from near the edge (left) to the fibril centre (right) for (a) plane strain and (b) axial symmetry.

3.3.1.1 Varying the mushroom stalk diameter *D*

Figure 3.5 shows the results for the influence of the mushroom cap diameter, D_f, relative to the stalk diameter, D, when $h/D_f = 0.008$ for plane strain (Figure 3.5 (a)) and axisymmetric fibrils (Figure 3.5 (b)). In the calculations, the mushroom diameter D_f (which defines the contact area) is kept constant and D is varied to obtain a range from $D_f/D = 1.09$ to 2. Even for the smallest mushroom cap a significant reduction of the corner stress singularity over the straight punch is found. As the mushroom cap diameter is increased, the magnitude of the corner stress diminishes. Further increases in the mushroom diameter beyond twice the stalk diameter result in further reductions of the corner stress over many orders of magnitude.

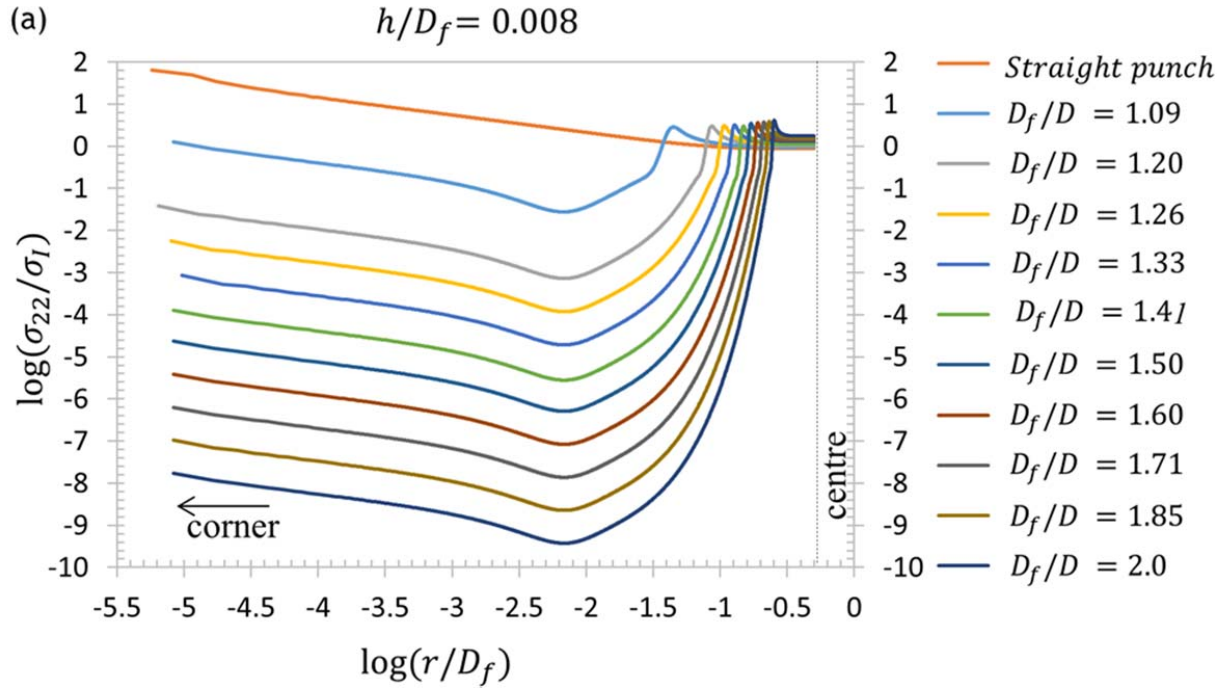

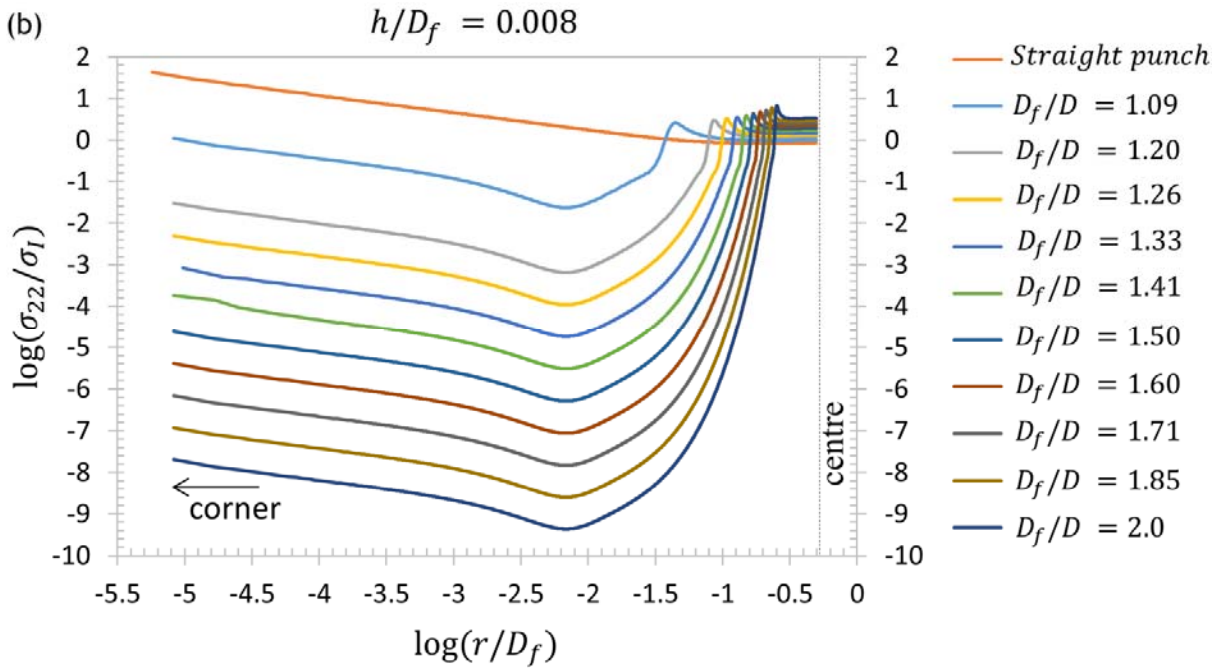

Figure 3.5: Tensile stress along the interface between the substrate and a fibril having a mushroom cap for (a) plane strain and (b) axial symmetry for various values of the mushroom cap diameter, D_f, divided by the diameter, D, of the fibril stalk. Results are shown for a mushroom cap that has a thickness, h, equal to 0.008 *times its diameter.*

3.3.1.2 Varying cap thickness h

The influence of the mushroom cap thickness h is reported for ten different values for plane strain fibrils Figure 3.6(a) and axisymmetric fibrils in Figure 3.6(b) when $D_f/D = 2$. Again, the mushroom diameter is kept constant and h is varied. It is observed that the amplitude of the corner stress singularity decreases when h/D_f decreases. The corner stress for thin caps, e.g. $h/D_f = 0.008$, is very low and the maximum stress visible in the plots lies close to the centre of the fibril. Any increase in h/D_f increases the corner stress, which approaches that of a straight punch as h increases.

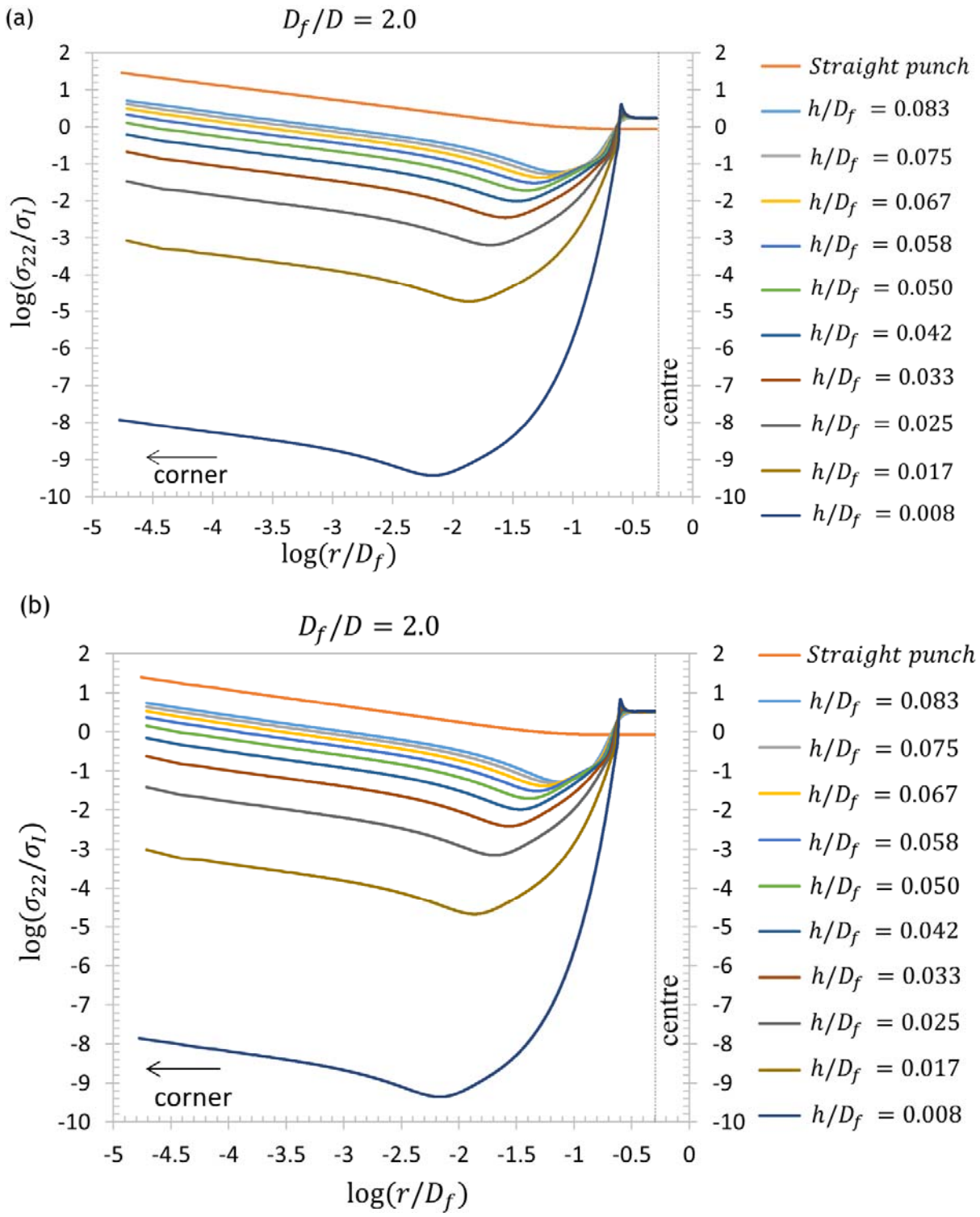

Figure 3.6: Tensile stress along the interface between the substrate and a fibril having a

mushroom cap for axial symmetry for various values of the ratio of the cap thickness to its diameter h/D_f. Results are shown for a fibril having a mushroom cap whose diameter is twice that of its stalk.

Figure 3.7 shows the calibration coefficient $\tilde{a}$ plotted versus h/D_f for various values of D_f/D for plane strain (Figure 3.7(a)) and axisymmetric (Figure 3.7(b)) mushroom fibrils. In addition, the results for straight punch fibrils are shown on the plots as horizontal dashed lines. On increase of the stalk diameter D and the mushroom cap thickness h the calibration coefficient $\tilde{a}$ increases and approaches the value for that of a straight punch, i.e. 0.331 for plane strain and 0.278 for the axisymmetric case.

(a)

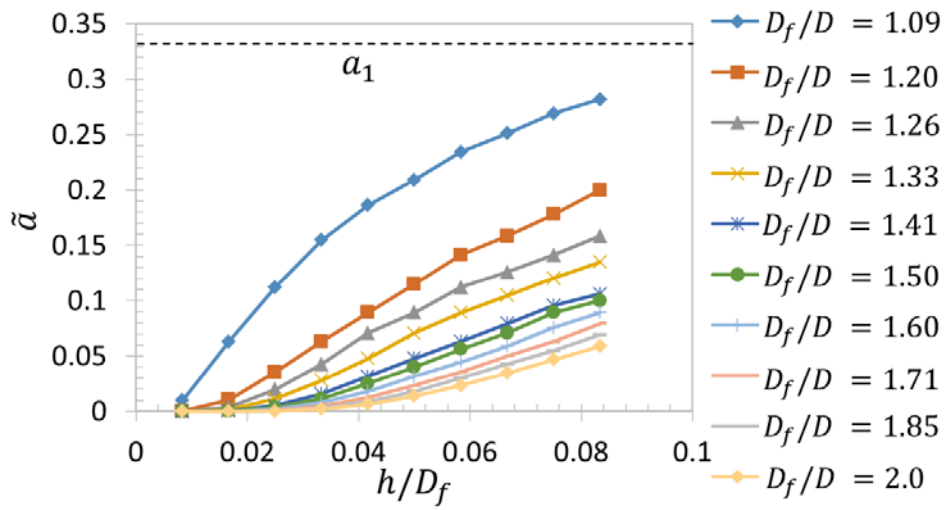

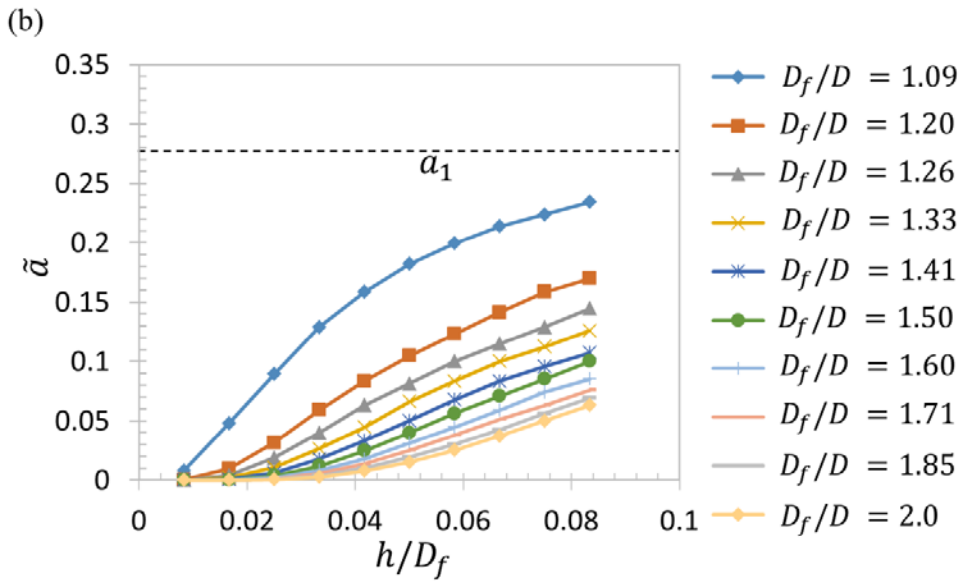

Figure 3.7: Calibration coefficient, $\tilde{a}$, plotted as a function of the ratio of mushroom cap thickness to diameter, h/D_f, for various ratios of fibril mushroom cap diameter to fibril stalk diameter D_f/D for (a) plane strain and (b) axial symmetry. The dashed horizontal lines indicate the value of the calibration coefficients a_1 for a straight punch.

Figure 3.8 similarly depicts the calibration coefficient $\tilde{a}$ as a function of the thickness, h, for fibrils having mushroom caps for axial symmetry, but now up to cap thicknesses that are comparable to the diameter of the mushroom cap. The result for a straight punch is also shown as the horizontal dashed line. This plot clearly shows that as the mushroom cap becomes very thick, and therefore the lower segment of the fibril becomes indistinguishable from a straight punch, the behaviour reverts to that of the straight punch.

We have compiled all values of the calibration coefficients from our results and presented them in Table 3.1 and Table 3.2.

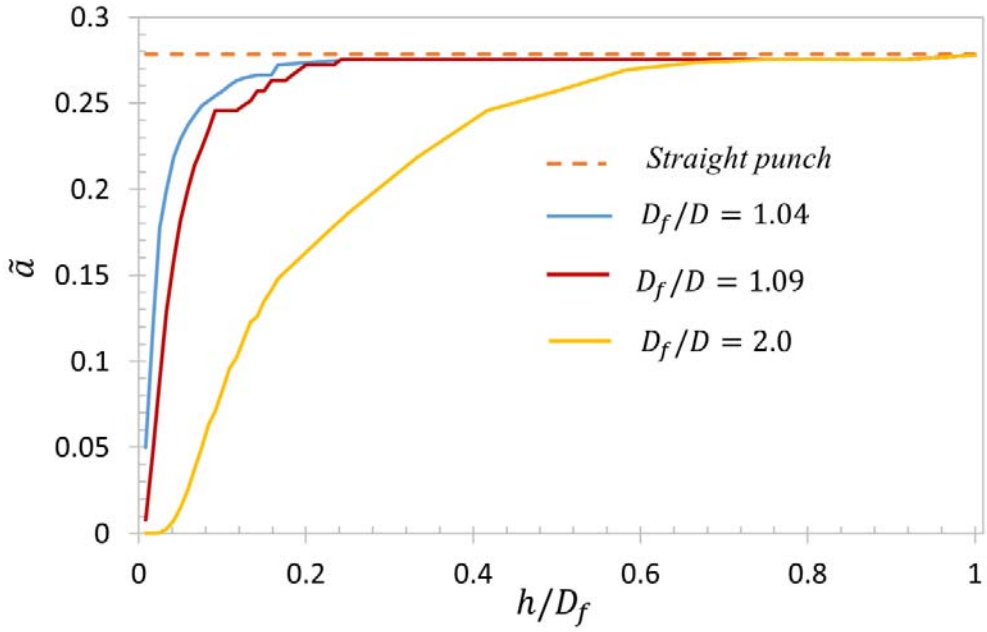

Figure 3.8: Calibration coefficient $\tilde{a}$ plotted as a function of the ratio of mushroom cap thickness to diameter, h/D_f, for 3 values of the ratio of fibril mushroom cap diameter to fibril stalk diameter D_f/D for axial symmetry. The dashed horizontal lines indicate the value of the calibration coefficient a_1 for a straight punch. The plot is extended to $h/D_f = 1$ to show how the results for the mushroom capped fibril converge to that of the straight punch as the mushroom cap is thickened.

	D_f/D									
h/D_f	1.09	1.2	1.26	1.33	1.41	1.50	1.6	1.71	1.85	2
0.008	0.010	2.5E-04	4.0E-05	6.3E-06	1E-06	1.8E-07	3.2E-08	4.5E-09	7.9E-10	1.3E-10
0.017	0.063	0.010	4.0E-03	1.78E-03	6.3E-04	2.82E-04	1.26E-04	5.0E-05	2E-05	8.9E-06
0.025	0.112	0.035	0.020	0.011	0.0054	0.004	0.002	0.0011	0.0006	0.0004
0.033	0.155	0.063	0.043	0.028	0.0158	0.011	0.0079	0.0050	0.003	0.002
0.042	0.186	0.089	0.071	0.048	0.0316	0.025	0.0178	0.0126	0.009	0.007
0.050	0.209	0.115	0.089	0.071	0.0479	0.040	0.0316	0.0234	0.018	0.014
0.058	0.234	0.141	0.112	0.089	0.0631	0.056	0.0447	0.0355	0.030	0.023
0.067	0.251	0.158	0.126	0.105	0.0794	0.071	0.0589	0.0501	0.043	0.035
0.075	0.269	0.178	0.141	0.120	0.0955	0.089	0.0759	0.0631	0.055	0.047
0.083	0.282	0.200	0.158	0.135	0.1059	0.1	0.0891	0.079	0.069	0.059

Table 3.1: Calibration coefficients $\tilde{a}$ for plane strain fibrils having a mushroom cap of width D_f and thickness h. The width of the fibril stalk is D.

	D_f/D									
h/D_f	1.09	1.20	1.26	1.33	1.41	1.50	1.60	1.71	1.85	2.0
0.008	0.008	2.2E-04	4.0E-05	6.3E-06	1.0E-06	2.0E-07	3.2E-08	5.0E-09	1.0E-09	1.6E-10
0.017	0.048	0.009	4.0E-03	1.7E-03	7.1E-04	3.0E-04	1.3E-04	5.6E-05	2.2E-05	1.0E-05
0.025	0.089	0.032	0.019	0.010	0.006	0.004	0.002	0.0011	0.0007	0.0004
0.033	0.129	0.059	0.040	0.0263	0.018	0.012	0.008	0.005	0.0035	0.003
0.042	0.158	0.083	0.063	0.045	0.033	0.025	0.018	0.013	0.010	0.008
0.050	0.182	0.105	0.081	0.066	0.050	0.040	0.031	0.025	0.019	0.015
0.058	0.200	0.123	0.100	0.083	0.068	0.056	0.045	0.038	0.030	0.025
0.067	0.214	0.141	0.115	0.100	0.083	0.071	0.059	0.051	0.043	0.037
0.075	0.224	0.158	0.129	0.112	0.095	0.085	0.074	0.063	0.056	0.050
0.083	0.234	0.170	0.145	0.126	0.107	0.1	0.085	0.076	0.069	0.063

Table 3.2: Calibration coefficients $\tilde{a}$ for axially symmetric fibrils having a mushroom cap of diameter D_f, and thickness h where D is the diameter of the fibril stalk.

3.4 Adhesion strength

The adhesion strength controlled by edge initiated detachment for fibrils having mushroom caps was next calculated by using equation 3.9 so that the strength is normalised by that of a straight punch where both the fibril with the mushroom cap and the straight punch have the same diameter where they contact the substrate, the same detachment length, l, at the corner, the same Young's modulus and the same adhesion energy, W. That is, the diameter of the mushroom fibril cap is the same as the diameter of the straight punch. We note that the detachment length l is small ($l \ll D_f$) so that its behaviour is controlled by the corner singularity. The results for adhesion strength are shown in Figure 3.9 for both plane strain (Figure 3.9(a)) and axisymmetric (Figure 3.9(b)) fibrils, and are shown as functions of h/D_f for various values of D_f/D. The results for straight punches are shown as horizontal dashed lines.

It is observed that the fibril cap geometry plays an important role in promoting adhesive strength. As the mushroom cap diameter is increased and as the cap thickness is decreased, the adhesive strength rises. Therefore, both a thin mushroom cap and one with a large diameter enhance the adhesive strength of the fibril when strength is controlled by detachment from a defect at the corner. In fact we observe that the adhesive strength can be enhanced by 10 orders of magnitude over the straight punch strength S^{punch} when the mushroom cap diameter is twice that of its fibril stalk and its thickness is less than 1% of its diameter.

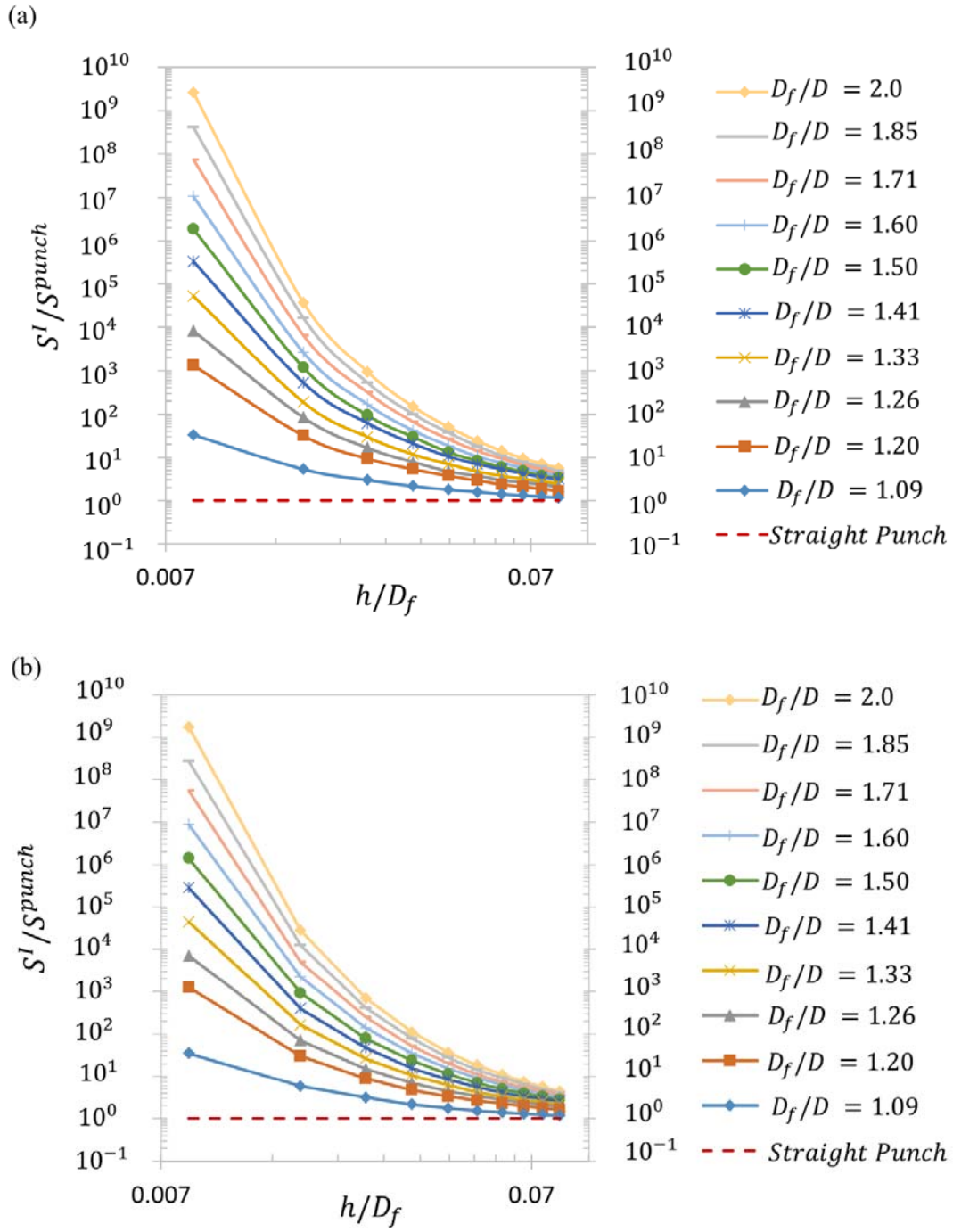

Figure 3.9: Adhesion strength for edge initiated detachment for a fibril having a mushroom cap of thickness h and diameter D_f is shown for (a) plane strain and (b) axial symmetry. The adhesion strength, S^I, of the fibril with the mushroom cap is given in terms of the average

stress on the interface and is normalised by the adhesion strength, S^{punch} of a straight punch fibril having the same diameter as the mushroom cap, with Young's modulus, adhesion energy and edge detachment length, l, the same for all fibrils.

We note, however, that the benefit from the mushroom cap is limited by 3 sources. One source of the limitation is the inherent strength of the bond between the fibril and the substrate, which can lead to detachment commencing near the centre of the fibril rather than at the edge. The second source is that weak areas of bonding or of no bonding at all may be present near the centre of the fibril, representing adhesion defects that may initiate detachment. The third source of limitation is the strength of the fibril material itself, which may lead to the stalk of the fibril rupturing, since the mushroom shape leads to a stress in the stalk that is higher than the average stress at the interface with the substrate. In the current work we have not addressed the material strength. Therefore, we cannot qualify our results with quantified limits from this source. However, the inherent strength of the bond between the fibril and the substrate can be addressed based on the following consideration. We observe from Figure 3.5, Figure 3.6 and others that the stress at the interface for the mushroom fibril is almost uniform under the stalk. When the stress at that location reaches a critical value, S^C, we assume that the cohesive strength of the bond has been reached and detachment of the fibril occurs, if it has not already occurred through an alternative mechanism, such as propagation of the defect at the edge of the contact. Furthermore, detachment motivated by an adhesion defect at or near the centre of interface between the fibril may be considered explicitly and this is addressed below; in this case we consider an adhesion defect located at the peak stress visible in Figure 3.4 and Figure 3.5 just below the edge of the stalk of the fibril.

We now assume that detachment can occur by one of the three failure modes just described, namely that triggered when stress at the interface under the stalk reaches the critical value S^C. In Figure 3.10 for comparison with this critical stress the adhesion strength, S^S, for fibrils having mushroom caps is shown in terms of the average stress on the mushroom fibril stalk instead of the average stress on the interface. The results are normalised by the adhesion strength of a straight punch fibril, S^{punch}, having the same diameter as the mushroom cap, and the same edge detachment length, Young's modulus and adhesion energy, and are shown for plane strain in

Figure 3.10(a) and for axial symmetry in Figure 3.10(b). Results for straight punches are shown as full horizontal lines. The detachment strength associated with the stress under the stalk reaching the critical level S^C is shown as a horizontal dashed line marked "Cohesive Strength S^C" in the figure legend. The location of this dashed line on the ordinate is arbitrary as we do not select a specific value of the cohesive strength for any given interface. Thus the line can be adjusted up or down to represent the cohesive strength in any given case; however, in plotting the dashed lines in Figure 3.10 we have assumed that the cohesive strength of the interface exceeds the strength of straight punches when detachment in that case initiates at the corner. The dashed line in Figure 3.10 is to be used in the following manner. The detachment strength for mushroom fibrils cannot exceed the value represented by the dashed line; therefore, for any given combination of mushroom cap diameter and thickness, the detachment strength is given by the lower of the dashed line and the line representing the fibril detachment strength when detachment initiates at the corner of the mushroom cap. We conclude, therefore, that given our assumption regarding the cohesive strength behaviour, fibrils with very thin, large diameter mushroom caps will experience detachment that initiates near the centre of the fibril, and will have a detachment strength predicted approximately by the horizontal dashed lines in Figure 3.10. In contrast, fibrils having thick, small diameter mushroom caps will experience detachment that initiates at the edge and their adhesive strength will be predicted by the full lines in Figure 3.10.

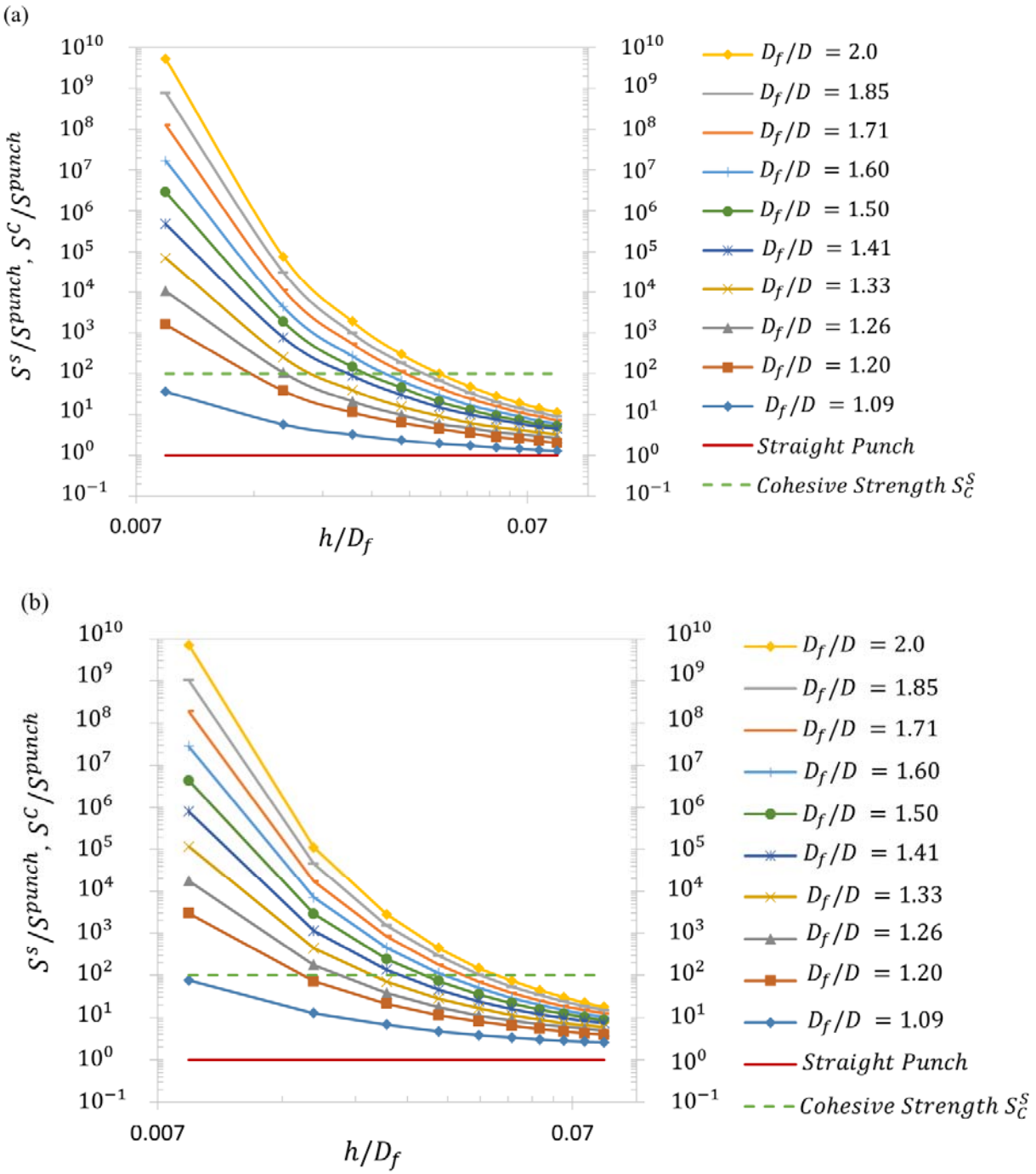

Figure 3.10: Adhesion strength, S^S (full lines), for edge initiated detachment fibrils having mushroom caps of thickness h and diameter D_f is plotted for (a) plane strain and (b) axial symmetry. In this case the adhesion strength is given in terms of the average stress applied to the

mushroom fibril stalk of diameter D and is normalised by the adhesion strength, S^{punch}, for a straight punch fibril having the same diameter as the mushroom cap, with Young's modulus, adhesion energy and edge detachment length, l, the same for all fibrils. The detachment strength associated with the stress under the stalk reaching a critical value S_C^S is represented by the horizontal dashed lines, marked "Cohesive Strength S_C^S." The dashed line for Cohesive strength S_C^S is exemplary with an arbitrary position.

When we inspect Figure 3.5 and Figure 3.6 we note that there is a peak in the normal traction at the interface that is located approximately under the edge of the fibril stalk. It is possible that the high stress under the edge of the fibril stalk will exceed the cohesive strength of the interface and therefore can initiate fibril detachment. Furthermore, if a detachment defect in the form of a region that is not adhered is located there it is possible that fibril detachment will initiate due to that defect. To further characterise this possibility, in Figure 3.11 we have plotted the ratio of the peak stress, σ_{Peak}, to the average interface stress σ_I, as a function of h/D_f, for various values of D_f/D for axially symmetric fibrils having mushroom caps. It is convenient at this point to introduce the notation of a stress concentration factor for the stress at the interface under the edge of the fibril stalk as $k = \sigma_{peak}/\sigma_I$.

We note that as the mushroom cap is made thinner or its diameter is made larger the peak in stress under the edge of the fibril stalk becomes more pronounced, and is more likely to promote fibril detachment. Therefore, the influence of this peak in stress on the likelihood of fibrillar detachment runs counter to that of the effect of the mushroom cap on edge detachment, whose likelihood is diminished by a thin, large diameter mushroom cap.

The influence of the peak in stress plotted in Figure 3.11 may be investigated as follows. As a rudimentary treatment of the relevant fracture mechanics, we may consider a small detachment of length or diameter $2a$ at the location of the peak stress. There will be a stress singularity around the edge of this detachment that will control the tendency for it to spread. As an approximation we may estimate this stress intensity factor as if the detachment were present in an infinite body subject to a stress equal in magnitude to the peak in stress plotted in Figure 3.11. The resulting value is

$$K_I = \sigma_{peak}\sqrt{\pi a} \qquad 3.10$$

Note that we have not attempted to estimate a shape factor that would multiply the right hand side of equation 3.10 but instead have simply assumed that this factor is unity. As our treatment is highly approximate, we consider this to be satisfactory. With K_{II} assumed to be zero, we compute the energy release rate according to the first and second results on the right hand side of equation 3.7 and set it equal to the adhesion energy to predict fibril detachment initiated as such a defect. The predicted strength, S^P, in terms of the average interface stress, for fibril detachment initiated at a defect at the location of the peak stress is then

$$S^P = \frac{1}{k}\sqrt{\frac{8EW}{3\pi a}} \qquad 3.11$$

where k is the stress concentration factor for the peak stress as introduced above in connection with Figure 3.11.

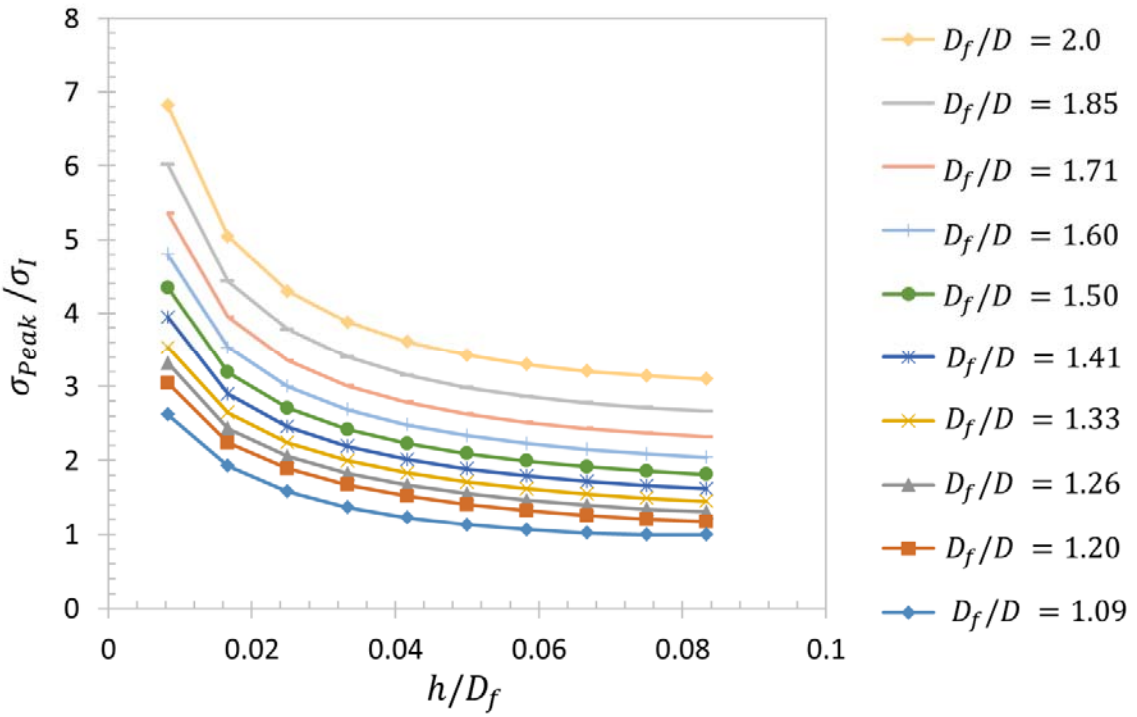

Figure 3.11: The magnitude of the local peak stress σ_{peak} near the centre of the fibril as depicted in the plots of interface stress in Figure 3.5 and Figure 3.6. The peak stress is normalised by the average interface stress σ_I and is therefore given as the stress concentration factor k. The result is shown as a function of h/D_f for various values of D_f/D. Note that a thin mushroom cap and a thin stalk will promote detachment at the centre by raising the local peak stress there.

The competition between detachment initiated at the edge of the mushroom cap and that initiated at a defect at the location of the peak stress under the edge of the fibril stalk is explored in Figure 3.12 as follows. The non-dimensional strength for edge detachment follows directly from equation 3.8 as

$$\bar{S}^I = \frac{S^I D_f^{0.406} l^{0.094}}{0.6\sqrt{EW}} = \frac{1}{\tilde{a}} \qquad 3.12$$

From equation 3.11 the strength for fibril detachment initiated at a defect located at the peak stress under the edge of the fibril stalk is now expressed in this non-dimensional form as

$$\bar{S}^P = \frac{S^P D_f^{0.406} l^{0.094}}{0.6\sqrt{EW}} = \frac{D_f^{0.406} l^{0.094}}{0.3k\sqrt{1.5\pi a}} \qquad 3.13$$

A comparison of $\bar{S}^I$ and $\bar{S}^P$ is plotted in Figure 3.12. The curves for $\bar{S}^P$ are marked "Detachment caused by a defect at the location of high stress under the edge of the fibril stalk." Note that for illustration we have chosen three different values for $3.3D_f^{0.406} l^{0.094}/\sqrt{1.5\pi a}$ namely $50, 100\ \&, 200$, representing the relative sizes of the two defects of length l and $2a$ respectively and the diameter, D_f, of the mushroom cap. These curves are marked in Figure 3.12 by their values $50, 100\ \&, 200$ respectively. These choices of $50, 100\ \&, 200$ are somewhat arbitrary and the reason for them will become clear below.

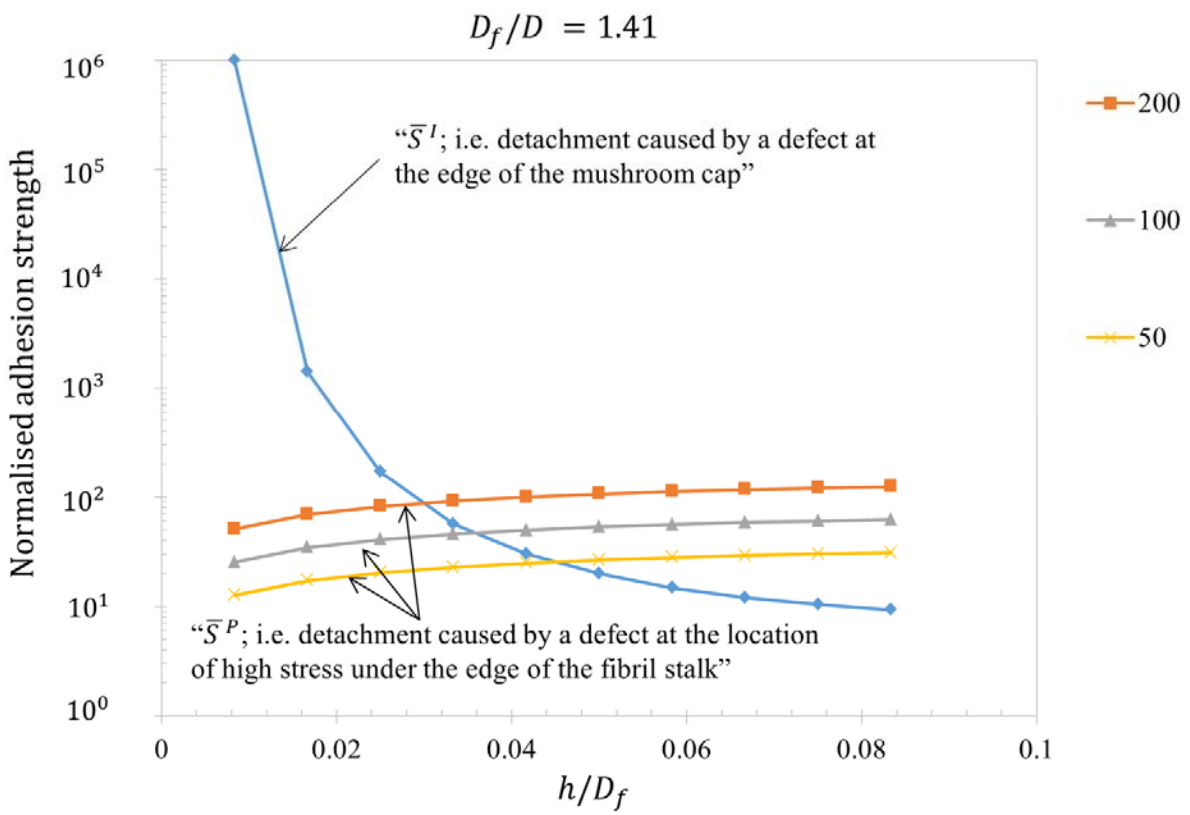

Figure 3.12: Adhesion strength for a fibril having a mushroom cap predicted for detachment due to a defect at the edge of the mushroom cap ($\bar{S}^I$) and for detachment due to a defect at the location of high stress under the edge of the fibril stalk ($\bar{S}^P$). The ratio of fibril mushroom cap

diameter to fibril stalk diameter $D_f/D = 1.41$ *and the fibril is axisymmetric. The defect sizes are plotted for three different values of* $(3.3D_f^{0.406}\ l^{0.094})/\sqrt{1.5\pi a} = 50, 100,$ *and* 200 *where* l *is the size of the defect at the mushroom cap edge and* $2a$ *is the size of the defect at the location of the high stress. These curves are marked accordingly as* $50, 100$ *and* 200.

In Figure 3.12 the curve for $\bar{S}^I$ is marked "Detachment caused by a defect at the edge of the mushroom cap." It can be seen that with the chosen relative sizes of the defects the plot for edge initiated detachment, within the domain of the figure, intersects with the plots for detachment commencing at the location of the peak stress. This is the reason for choosing the values $3.3D_f^{0.406}l^{0.094}/\sqrt{1.5\pi a} = 50, 100$ & 200 as the resulting intersections enable us to illustrate the relevant situation, which is as follows. For this explanation we focus on the case where either edge initiated detachment takes place or detachment occurs commencing at the location of peak stress with flaw sizes such that $3.3D_f^{0.406}l^{0.094}/\sqrt{1.5\pi a} = 200$. In this case, the adhesive strength of the fibril is predicted by the lower of the curve for the latter and the curve for edge initiated detachment in Figure 3.12. This implies that for small values of h/D_f detachment will be initiated at the defect under the peak in stress at the edge of the fibril stalk, whereas for large values of h/D_f detachment will be initiated at the edge of the mushroom cap. The reason for choosing the three different values $3.3D_f^{0.406}l^{0.094}/\sqrt{1.5\pi a} = 50, 100$ & 200 in Figure 3.12 is to illustrate how the domains of edge initiated detachment and detachment initiated at the peak stress location vary as the relative sizes of a, l and D_f change. It can be seen that as $3.3D_f^{0.406}l^{0.094}/\sqrt{1.5\pi a}$ becomes larger, the domain in which edge initiated detachment occurs becomes more extensive; this outcome is a consequence of the fact that $3.3D_f^{0.406}l^{0.094}/\sqrt{1.5\pi a}$ becomes larger as a consequence of a diminishing, so that detachment caused by a defect at the location of the peak stress at the edge of the fibril stalk is less likely.

3.5 Discussion

Spuskanyuk et al. (Spuskanyuk et al., 2008) provided the initial study on how the corner stress singularity varies from a straight punch to a mushroom fibril for frictionless and sticking friction conditions. In the course of the work just described we have repeated their simulations and our results are in good agreement with theirs. They also reported how the stress varies along the substrate interface for the straight punch and the mushroom fibril, and a similar behaviour can be observed in our results in Figure 3.2 and Figure 3.4 respectively. The straight punch exhibits lower adhesive strength when compared to mushroom fibrils because the corner stress singularity acts as the driving force to initiate detachment. In the case of the mushroom fibril, the extra material present on either side of the stalk evidently reduces the corner singularity, which in turn improves the adhesive strength of the fibril. The results in Figure 3.5 and Figure 3.6 show that there is a zone of higher stress at the centre of the fibril under the edge of the stalk, from where detachment could now initiate. Experimentally, such a behaviour was found by Hossfeld et al. (Hossfeld et al., 2013) and by Micciché et al. (Micciché et al., 2014), who observed that detachment of mushroom fibrils started from close to the centre. We have only investigated this issue in a preliminary manner as we have not quantified the strength of the adhesive bond between the fibril and the substrate for any specific combination of materials. However, we have provided illustrative results that indicate the trade-off between detachment initiated near the centre of the fibril and that commencing at the edge of the mushroom cap.

The most systematic experimental study on how the contact shape of a compliant PDMS (polydimethylsiloxane) fibril adhered to a glass probe affects adhesion was published by del Campo et al. (del Campo et al., 2007). They examined different geometries such as the straight punch, the spherical cap, the spatula cap, the straight cap with rounded edges, the mushroom cap and the concave cap. Mushroom fibrils showed superior adhesion when compared to other shapes. The adhesive strength of the straight punch and the mushroom fibril varied from approximately 30 to 60 kPa depending on the fibril radius and preload. For a mushroom fibril with $D_f/D = 1.29$, the adhesive strength varied from 30 to 185 kPa.

Carbone and Pierro (Carbone and Pierro, 2012) have calculated the dependence of adhesive performance on the mushroom cap geometry and suggested an optimal shape for adhesion. They

erroneously assumed that the corner stress singularity involves inverse square root behaviour, a result that cannot be justified as it disagrees with the analysis of Khaderi et al. (Khaderi et al., 2015) and our results. Therefore, their interpretation of their results cannot be deemed to be reliable, as they used the wrong order of singularity throughout their analysis. However, Carbone and Pierro (Carbone and Pierro, 2012) show results for stress at the interface between the fibril and the substrate that can be used in principle to deduce the adhesive strength of mushroom shaped fibrils, albeit of a different design from the ones we have considered. On the other hand, the mushroom caps that Carbone and Pierro (Carbone and Pierro, 2012) consider in their analysis are very large in diameter, with the smallest one having a diameter twice as large as that of the fibril stalk. As we have shown that mushroom fibrils having cap to stalk diameter ratios much less than 2 are very effective at raising fibril adhesive strengths, the designs contemplated by Carbone and Pierro (Carbone and Pierro, 2012) are somewhat unrealistic and unnecessary.

Aksak et al. (Aksak et al., 2014) have presented a computational study on how the geometry of a wedge or conical shaped mushroom cap influences fibrillar adhesion by varying the angle (from $25°$ to $80°$) at which the wedge shaped mushroom cap meets the substrate. Using a Dugdale cohesive zone to model the detachment process, they found that the strongest adhesion was associated with a mushroom cap that meets the substrate at $45°$ and (in our notation) $D_f/D = 1.1$ or 1.2. In addition, they assumed a thin disc of material appended to the tip with the same diameter as the fibril tip; this was found to compromise the adhesive strength of the fibril.

To make a direct comparison with the work of Aksak et al. (Aksak et al., 2014) we have chosen a mushroom fibril with wedge angle $45°$ and a thin disc of thickness $0.01\,D$ appended to it. Two cases were examined with different ratios of mushroom cap diameter to stalk diameter: $D_f/D = 1.09$ and 1.2. The comparison of the stress distributions for wedge shape (as in (Aksak et al., 2014)) and mushroom shape (as in the present study) can be seen in Figure 3.13. The calibration coefficients and adhesion strength values are listed in Table 3.3. The range of values 1.2 to 35 and 1.63 to 1242 corresponds to the respective h/D_f. It can be observed from Figure 3.13 and Table 3.3 that the mushroom fibrils (from the current study) have the capability to perform better, provided detachment does not occur earlier with a different mechanism. The stress peak close to the centre of mushroom fibrils seen in Figure 3.13 can act as a crack initiation point, but

the peak can be removed by improving the design which will be discussed in section 3.5.1. Therefore, it is relatively straightforward to design mushroom shaped fibrils to outperform wedge shaped ones.

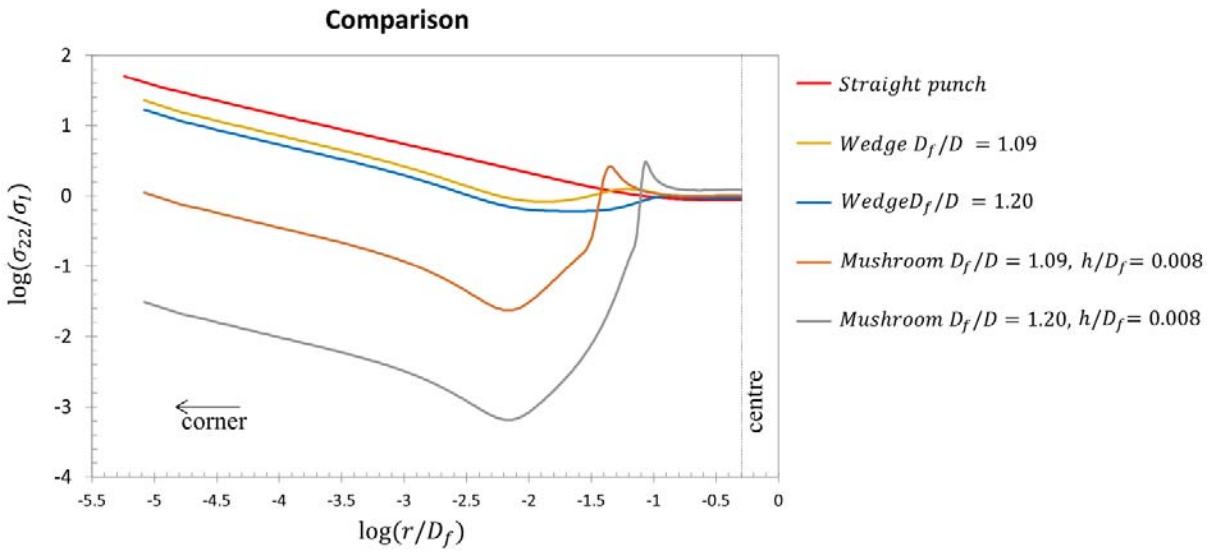

Figure 3.13: Comparison of published fibril shapes and present study: Tensile stress along the interface for a straight punch, a mushroom fibril (as in the current paper) and a wedge shaped mushroom cap (as in (Aksak et al., 2014)), all for the axisymmetric case. Adhesion controlled by edge detachment is superior for the mushroom shaped fibrils compared to that of the wedge shaped ones.

D_f/D	$\tilde{a}$ *Wedge*	S^I/S^{punch} Wedge	S^I/S^{punch}
1.09	0.151	1.84	1.2 to 35
1.2	0.125	2.21	1.63 to 1242

Table 3.3: Calibration coefficients $\tilde{a}$ and normalised adhesion strength for axisymmetric fibrils with wedge shaped mushrooms as assumed by Aksak et al. (2014) (S^I/S^{punch} $Wedge$). For comparison, we list the adhesion strength of mushroom cap fibrils (S^I/S^{punch}) used in the current paper. The range of S^I/S^{punch} values refers to the mushroom fibrils with different h/D_f.

3.5.1 Improved shape for a fibril having a mushroom cap

As noted above, the results in Figure 3.5 and Figure 3.6 show that there is a peak in the normal traction at the interface between the fibril and the substrate that is located immediately under the edge of the fibril stalk. We have explored designs that will eliminate this elevation in the stress, and have found that it disappears when there is a fillet radius, as in Figure 3.14, smoothing the transition from the fibril stalk to the mushroom cap. As an example of this improvement in the design, we carry out simulations for the stress at the interface between the substrate and fibrils having $D_f/D = 1.41$ and a fillet radius, R, such that $R/D_f = 0.083$. The results for the normal traction at the interface are shown in Figure 3.15 for various values of h/D_f for axial symmetry. It can be seen that the stress elevation visible in Figure 3.5 and Figure 3.6 is absent in the results in Figure 3.15. In this case the maximum normal traction under the fibril, other than at the edge of the cap, is simply twice the average stress on the interface.

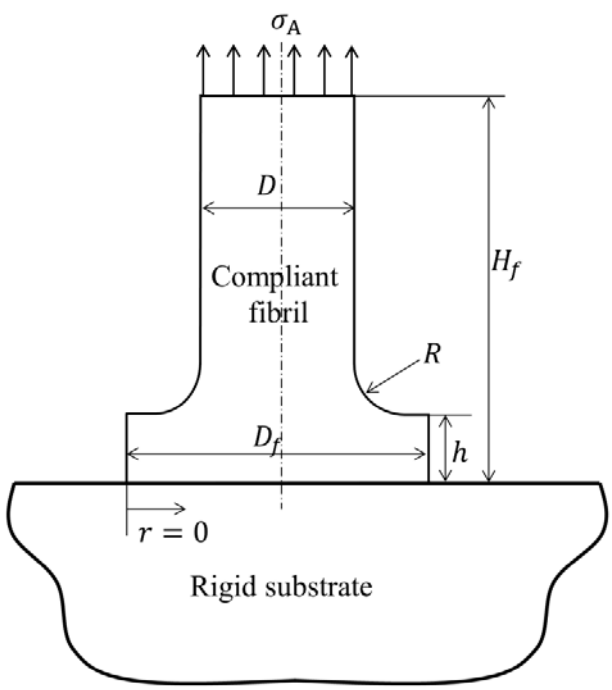

Figure 3.14: Schematic of a mushroom fibril with a fillet of radius R where $R/D_f = 0.083$.

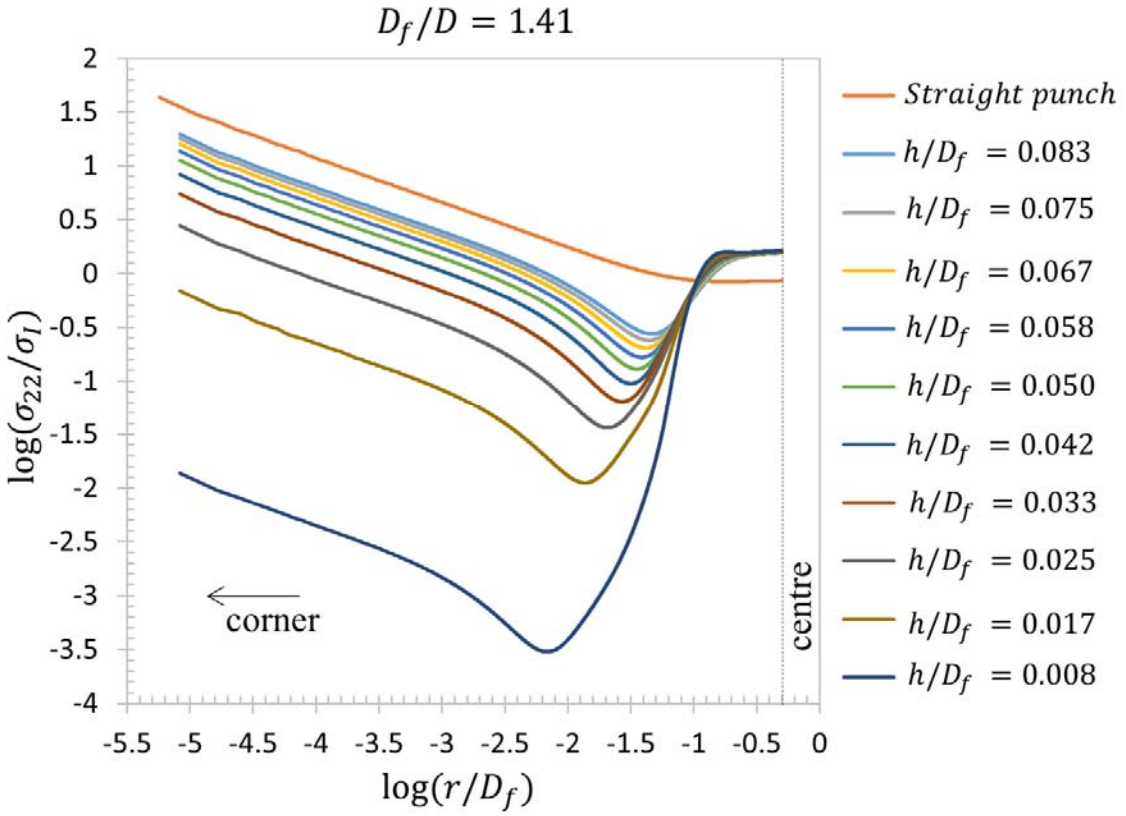

Figure 3.15: Tensile stress along the interface between the substrate and an axisymmetric mushroom cap fibril having a value of the radius of the fillet, R, that is effective at eliminating the high stress under the edge of the fibril stalk. Results are shown for a fibril having a mushroom cap whose diameter is 1.41 *times that of its stalk and for various values of the ratio of the cap thickness to its diameter h/D_f. The fillet radius is such that $R/D_f =$* 0.083.

The calibration coefficient for the edge singularity is extracted from the results in Figure 3.15 by fitting the plots to the asymptotic solution as before. The results, designated $\tilde{a}_{fillet}$, are shown in Figure 3.16 and are listed in Table 3.4, as are the calibration coefficients, $\tilde{a}$, for fibrils having mushroom caps without the fillet radius. It can be seen that the introduction of the fillet radius has increased the amplitude of the edge singularity compared to that prevailing in the absence of the fillet radius. It follows that the mushroom fibrils with the fillet radius will be more prone to edge detachment than the equivalent design lacking a fillet radius. However, the fillet radius, by

eliminating the peak in stress that would otherwise occur under the edge of the stalk, diminishes the likelihood of detachment commencing near the centre of the fibril.

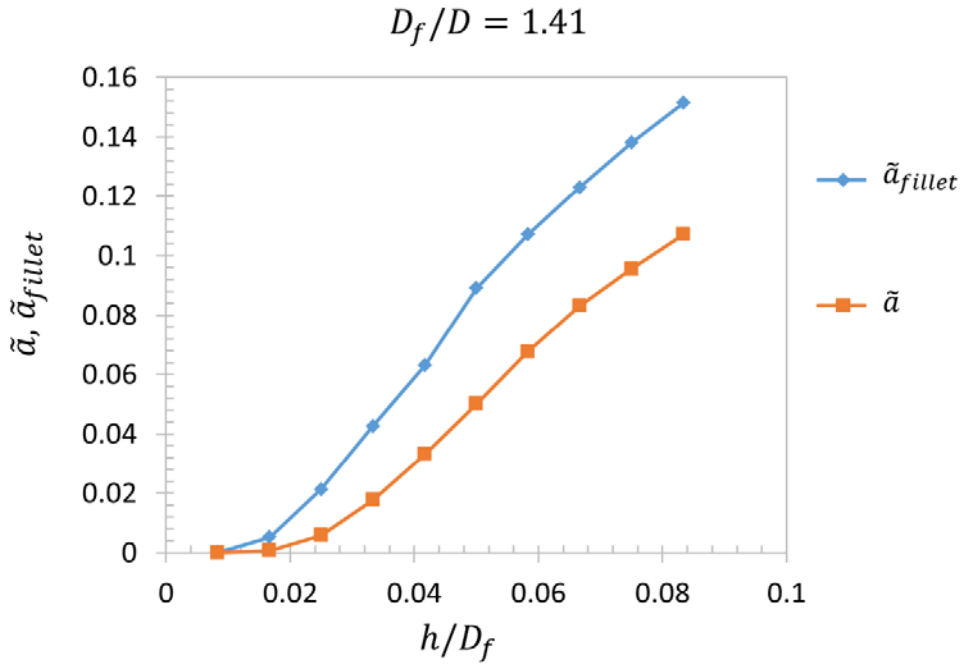

Figure 3.16: Calibration coefficients, $\tilde{a}$, for mushroom fibrils without fillet radii and, $\tilde{a}_{fillet}$, for mushroom fibrils with fillet radii, both plotted as a function of the ratio of mushroom cap thickness to diameter, h/D_f, for a ratio of fibril mushroom cap diameter to fibril stalk diameter $D_f/D = 1.41$ for axisymmetric fibrils. The fillet radius is such that $R/D_f = 0.083$.

h/D_f	$\tilde{a}_{fillet}$	S^I_{fillet}/S^{punch}
0.008	1.05E-04	3.16E+03
0.017	5.25E-03	6.31E+01
0.025	2.14E-02	1.55E+01
0.033	4.27E-02	7.76E+00
0.042	6.31E-02	5.25E+00
0.050	8.91E-02	3.71E+00
0.058	1.07E-01	3.09E+00
0.067	1.23E-01	2.69E+00
0.075	1.38E-01	2.40E+00
0.083	1.51E-01	2.19E+00

Table 3.4: Calibration coefficients $\tilde{a}$ for axisymmetric fibrils having a fillet radius that is effective at eliminating the high stress under the fibril stalk for mushroom caps with $D_f/D = 1.41$ where D_f and D are the diameter of mushroom cap and the stalk respectively and h is the thickness of the mushroom cap. The fillet radius $R/D_f = 0.083$.

In Figure 3.17 we have replotted the results in Figure 3.16 to represent S^I/S^{punch}, the ratio of the adhesive strength of a fibril having a mushroom cap to that of a punch shaped fibril. One curve, marked "With fillet radius" gives the results for fibrils with the fillet radius connecting the mushroom cap and the stalk, while the results marked "Without fillet radius" are for the fibrils lacking the smooth transition from stalk to mushroom cap. It can be seen that the adhesive strength of the fibrils having a fillet radius is somewhat poorer than that for fibrils in which the fillet radius is absent. However, that conclusion is associated with detachment that commences at the edge of the mushroom. Due to the lack of a peak in the stress under the fibril stalk when there is a fillet radius present, the situation will be reversed when detachment commences near the centre of the fibril. In the case of the fibrils used for the calculations with results presented in Figure 3.17, the adhesive strength for detachment commencing at the centre of the fibril, measured in terms of S^I, i.e. the average stress on the interface, will be $\sigma_o/2$, where σ_o is

representative of the cohesive interaction strength between the fibril and the substrate. If we assume that this interaction is of the Dugdale type, σ_o will be equal to the cohesive stress attracting one surface to the other.

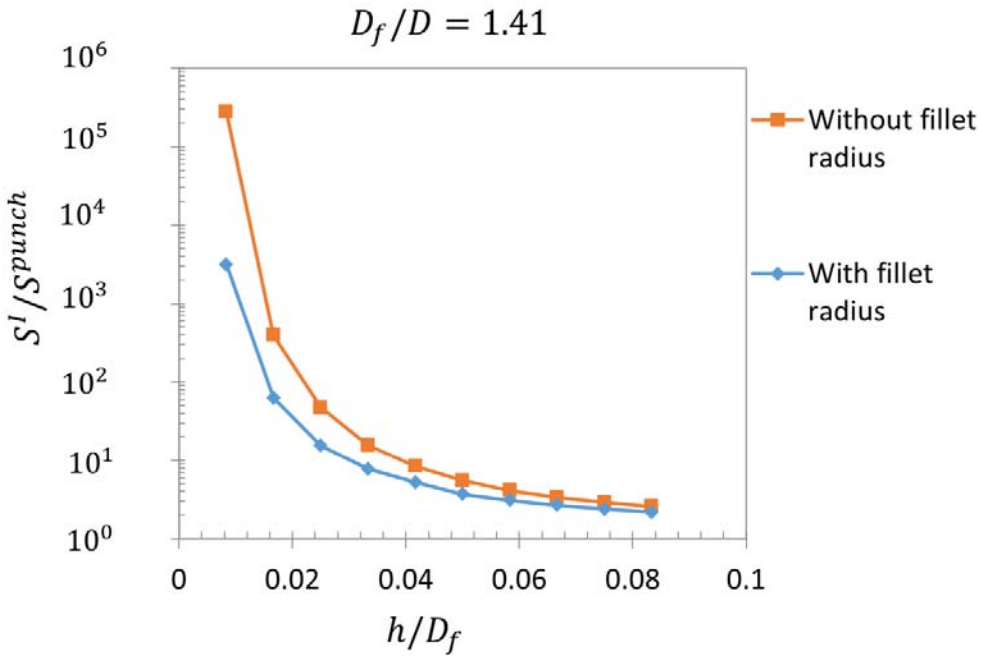

Figure 3.17: Adhesion strength for fibrils with and without fillet radii plotted versus h/D_f for a ratio of fibril mushroom cap diameter to fibril stalk diameter $D_f/D = 1.41$ for axisymmetric mushroom fibrils. Detachment in these cases is initiated at the edge of the mushroom cap. The adhesion strength is normalised by that for a punch shaped fibril. The fillet radius is such that $R/D_f = 0.083$.

In fact, we can assume that a fillet radius can be introduced in all cases to smooth the transition from the fibril stalk to the mushroom cap no matter the values of the ratios D_f/D and h/D_f. Designs can then always be found with a sufficiently effective fillet radius such that detachment will commence near the centre of the fibril, and this will occur at a strength, measured in terms of the average stress at the interface, given by

$$S^I = \left(\frac{D}{D_f}\right)^2 \sigma_o \qquad 3.14$$

Thus the best strength is achieved with the smallest possible mushroom cap diameter that eliminates edge detachment and therefore leads to a strength quite close to the cohesive stress.

3.6 Conclusion

In the current work we focus on the corner singularity for a mushroom fibril that is assumed to be perfectly bonded to a rigid substrate so that no sliding can occur at the interface between the fibril and the substrate to which it is attached. The mushroom cap and stalk dimensions are varied and the calibration coefficient and the adhesive strength are calculated for the resulting combinations of mushroom cap geometry. In total, more than a hundred different combinations of fibril geometry are analysed in this study. The following conclusions can be drawn:

- In agreement with earlier work, straight punch fibrils exhibit a corner stress singularity. This explains the tendency of straight fibrils to detach from a corner location.
- In mushroom fibrils, the corner stress is reduced to a level that may preclude detachment initiating at that location. Instead, the stress near the centre of the fibril may initiate detachment there.
- The mushroom geometry strongly influences the stress distribution. The corner stress singularity amplitude is minimized for small cap thicknesses and small fibril stalk diameters.
- Optimisation of fibrillar adhesives will require mushrooms caps with minimum thickness and minimum stalk diameter, but limited by the tendency for detachment to occur near the centre of the fibril and by the material strength.
- Introduction of a fillet radius to smooth the transition from the fibril stalk to the mushroom cap was successful in removing the stress peak that otherwise occurs in mushroom fibrils on

the interface immediately below the edge of the fibril stalk. However, the adhesive strength controlled by the edge singularity is reduced, which is a drawback. However, the adhesive strength associated with detachment commencing near the centre of the fibril is improved. The results suggest that an adhesive strength close to the cohesive stress at the interface can be achieved with careful design of the mushroom cap and the fillet radius. A detailed analysis is necessary to establish the best design.

4 Adhesion and stress singularities for composite fibrils with soft tip layers

4.1 Introduction

Nature provides many concepts for temporary and reversible adhesion to various substrates, e.g. on plants and animals (Gorb, 2007; Gorb, 2008). Geckos and insects use hairy structures whose adhesion is due to intermolecular forces (Arzt et al., 2003; Autumn et al., 2000; Autumn et al., 2002; Gao et al., 2005; Huber et al., 2005a). Transferring nature's solution into artificial structures that may eventually find technological applications is the current objective of research and development efforts (Boesel et al., 2010; Kamperman et al., 2010; Menon et al., 2004; Purtov et al., 2015; Sathya et al., 2013). Many reversible attachment systems (Paretkar et al., 2011) based on micropatterns (del Campo and Arzt, 2011) have been investigated in the literature (Arzt et al., 2002; del Campo and Arzt, 2007; Greiner et al., 2009; Mengüç et al., 2012; Spolenak et al., 2005).

Recent modelling studies have pointed to the importance of optimizing the distribution of interfacial stresses in order to realize high adhesion. Following biological examples, fibrils with spatula and mushroom-shaped tips have repeatedly been demonstrated to exhibit superior adhesion performance (del Campo et al., 2007; Gorb et al., 2007a; Greiner et al., 2007; Kim and Sitti, 2006). Numerical simulations have suggested that the main reasons for improved adhesion is the reduction of the stress magnitudes associated with the corner singularity, which is likely to act as a crack initiation point in straight punch fibrils (Khaderi et al., 2015). Spuskanyuk et al. (Spuskanyuk et al., 2008) showed numerically that in mushroom fibrils the edge stresses were significantly reduced when compared to those of straight punches and other shapes. Based on earlier work by Akisanya et al. (Akisanya and Fleck, 1997) and Khaderi et al. (Khaderi et al., 2015) on the corner stress singularity, we have recently addressed the stress distributions of mushroom fibrils by Balijepalli et. al. (Balijepalli et al., 2016). In an extensive parametric study, we showed that such structures benignly distribute tractions along the interface and reduce the magnitude of the stresses associated with the singularity at the corner. This is suggested to be the main cause of the higher adhesion of mushroom structures while the onset of detachment is shifted away from the corner to the centre of the interface (Aksak et al., 2014; Balijepalli et al., 2016; Carbone and Pierro, 2012).

Mushroom tips are often manufactured by manual inking of previously made microstructures in a prepolymer and subsequent curing in contact with a smooth counter surface (Fischer et al., 2016b; Greiner et al., 2007; Murphy et al., 2009; Varenberg and Gorb, 2007). Tip and stalk material can be identical, but choosing a softer tip layer can further increase adhesion, especially to rough and deformable surfaces such as skin (Bae et al., 2013b; Kroner et al., 2012b; Kwak et al., 2011). Depending on the packing density and the amount of prepolymer used for the inking, not only isolated tips can be achieved but also connection among several or all fibrils (Liu et al., 2009; Vajpayee et al., 2009). Despite these benefits, mushroom structures suffer from the drawbacks that their fabrication is complicated, does not always lead to reproducible results and can hardly be scaled up to larger areas.

An alternative way to manipulate the interfacial stresses is to create fibres with gradients in mechanical properties (Bae et al., 2013a; Minsky and Turner, 2015; Scholz et al., 2008; Yoon et al., 2011). The ladybug has recently been shown to exhibit attachment hairs with at least two property levels, i.e. a soft tip layer with a modulus of about 1.2 MPa attached to a stiff stalk with a modulus of about 6.8 GPa (Peisker et al., 2013). According to Gorb and Filippov (Gorb and Filippov, 2014) such structures tend to enhance adhesion properties, especially against substrates with unpredictable roughness.

In this chapter, we propose, as an alternative, a novel two-material composite fibril with a sharp transition in modulus. For modelling the stress singularities, the fibril was assumed to have a straight punch shape, but to consist of a comparatively stiff stalk and a soft layer at its tip. A detailed numerical study is presented of the stress distributions along and near differently shaped interfaces between the two materials, as shown in Figure 4.1. The system parameters are the Young's moduli (E_1, E_2) and the thicknesses $(L_1,\ L_2)$ of, respectively, the stalk and the soft tip layer. For comparison, adhesion experiments to glass were performed with single macroscopic composite fibrils.

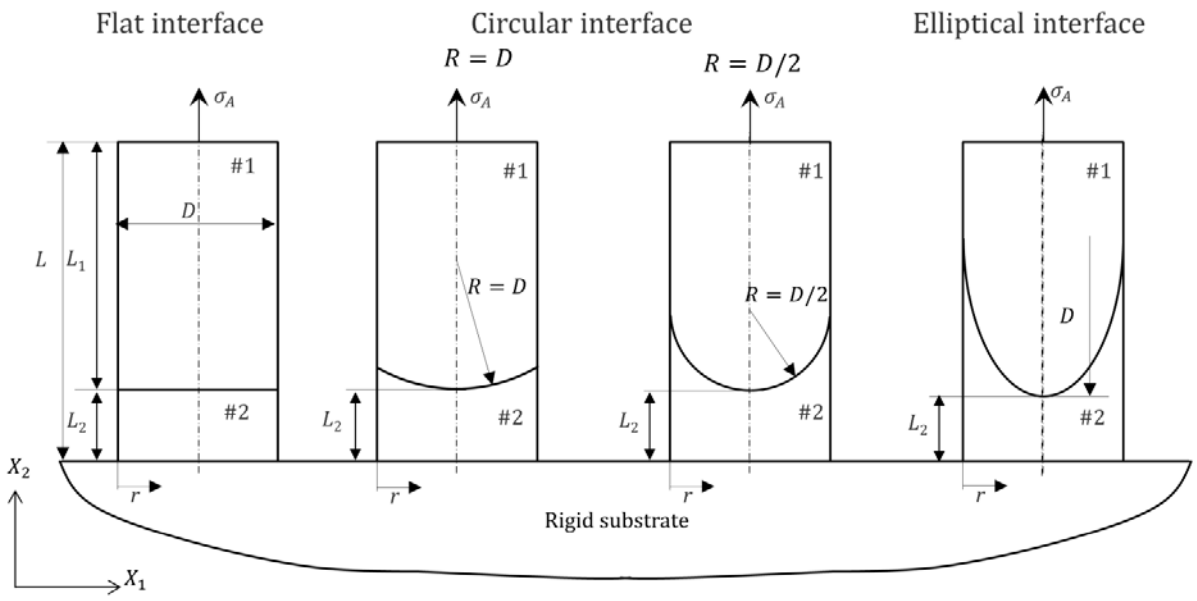

Figure 4.1: Schematic of different composite fibril interfaces, namely a flat interface, two circular interfaces ($R = D$ and $R = D/2$) and an elliptical interface (where major axis is double the diameter) considered in the current work. The parameter R is the radius of curvature of the interface, D is the fibril diameter, L is the total height of the composite fibril, L_1 and L_2 are the thicknesses of the stiff stalk (#1, with modulus E_1) and the soft layer (#2, with modulus E_2) respectively. The composite fibrils adhere to a rigid substrate. For a remote tensile stress σ_A applied on the free end, the normal stress distribution is calculated along the fibril/substrate interface.

4.2 Numerical and experimental methods

4.2.1 Numerical simulations

A compliant composite fibril, with diameter D and length L, was assumed to adhere to a rigid substrate with no defects (interfacial cracks) along the interface. The ratio of L to D was 2 for all the simulations and the experiments. The fibril was considered to be an isotropically elastic and incompressible solid. The boundary condition was assigned to be sticking friction which totally suppressed sliding of the fibril against the substrate. A remote stress σ_A was applied on the free

end of the fibril (Figure 4.1), which results in a stress singularity at the fibril-substrate interface (Akisanya and Fleck, 1997). The corner singularity method was adopted from Akisanya and Fleck (Akisanya and Fleck, 1997) and Khaderi et al. (Khaderi et al., 2015). The treatment follows that of our earlier work on mushroom-shaped fibrils (Balijepalli et al., 2016). The singular terms in the asymptotic normal stress (σ_{22}) and shear stress (σ_{12}) components are given by equations 3.1 and 3.2:

The calibration coefficients of a straight homogeneous punch are $a_1 = 0.331$ for the plane strain and $a_1 = 0.278$ for the axisymmetric case according to Khaderi et al.(Khaderi et al., 2015). The asymptotic stress solutions for the plane strain case in logarithmic form were listed in Chapter 3.2.

The resulting normal and shear stress along the interface of a straight punch and a rigid substrate for plane strain and axisymmetric fibrils are shown in *Figure 3.2* (a) and (b) respectively. In order to predict the adhesive strength of the fibril, we assume a small detachment length l at its edge where the corner singularity controls the detachment behaviour. A detailed analysis was provided in Chapter 3.2. The stress distribution near the crack tip can be described by equation 3.4 and the Mode I and Mode II stress intensity factors, K_I and K_{II}, are given by equations 3.5 and 3.6. The energy release rate during detachment of a composite fibril seen in *Figure 4.1* is given by

$$G = \frac{1 - v^2}{2E_2}\,(K_I^2 + K_{II}^2) = \frac{3}{8E_2}(K_I^2 + K_{II}^2) = \frac{2.8\sigma_A^2 D^{0.81} l^{0.19} \tilde{a}^2}{E_2} \qquad 4.1$$

where E_2 is Young's modulus of the soft layer in contact with the rigid substrate and v is the associated Poisson's ratio, equal to 0.5 consistent with incompressibility. For detachment to occur, the energy release rate must be equal to the adhesion energy, W. The adhesion energy of the composite fibril S^I can be expressed as

$$S^I = \frac{0.6\sqrt{E_2 W}}{D^{0.406} l^{0.094} \tilde{a}} \qquad 4.2$$

We define a normalised adhesion strength by dividing by the value for the straight punch S^{punch}, which is assumed to have the same initial crack length:

$$\frac{S^I}{S^{punch}} = \frac{a_1}{\tilde{a}} \qquad 4.3$$

The resulting adhesion strength was calculated using equation 4.3.

Following the expectation that the interfacial stress distribution would be modulated by the geometry of the interface, four different interface shapes were considered, i.e. flat, two circular and elliptical as shown in Figure 4.1. Calculations were performed for plane strain ($2D$) and axisymmetric ($3D$) conditions. Only $3D$ results will be discussed in the main thesis while the $2D$ results are presented in Appendix B. For each interface shape, we have examined six different thickness ratios ($L_2/L = 0.25, 0.20, 0.15, 0.10, 0.05$ and 0.005) and five different Young's modulus ratios ($E_1/E_2 = 2, 10, 10^2, 10^3$ and 10^6) for all axisymmetric ($3D$) fibrils. For plane strain ($2D$) fibrils only five different thickness ratios ($L_2/L = 0.25, 0.20, 0.15, 0.10$ and 0.05) and four different Young's modulus ratios ($E_1/E_2 = 2, 10, 10^2$ and 10^3) were considered.

A mesh validation study was performed to identify the optimum mesh density and the element size along the interface was chosen such that further mesh refinement did no longer influence the results (within 0.5 % in the stress values). We used linear quadrilateral hybrid elements for plane strain (Abaqus terminology element CPE4RH) and axial symmetry (CAX4RH) (Abaqus6.11, 2011). The total number of elements varied accordingly from $100{,}000$ to $600{,}000$ for different investigated geometries. The mesh along the interface was much finer than elsewhere to extract more precise information from this region.

4.2.2 Fibril fabrication[2]

In addition to the numerical simulations, adhesion was tested in selected experiments on composite fibrils with macroscopic dimensions (diameter 2 mm, height ca. 4 mm and varying soft layer thickness). The fibrils consisted of a stiff stalk; for this, poly(ethyleneglycol) dimethacrylate (PEGdma, Sigma-Aldrich, St. Louis, MO, USA; elastic modulus of about 350 MPa) or polydimethylsiloxane (PDMS, Sylgard 184, Dow Corning, Midland, MI, USA; elastic modulus of about 2 MPa) were used. The softer tip layer consisted of polyurethane Polyguss $74-41$ (PU, PolyConForm GmbH, Duesseldorf, Germany) with an elastic modulus of about

[2] Experimental work was performed by S. C. L. Fischer.

900 kPa. The fibrils were fabricated using a two-step moulding process as illustrated in Figure 4.2. Thus, composites fibril structures with an elastic modulus ratio of stiff to soft of about 350 and 2, and three interface geometries, flat, circular ($R = D/2$) and elliptical, were generated. As straight-punch control samples, fibrils consisting entirely of PU were manufactured.

The fibrils were fabricated in a two-step moulding process as shown in Figure 4.2. In a first step, the stalk of the composite fibril was generated using a custom-made aluminum mould as shown in the optical micrograph in Figure 4.2a. The soft layer was added to the fibril in the second molding step (Figure 4.2b): The second pre-polymer, PU, was applied on top of the fibril and the superfluous polymer was removed. To realize different thicknesses of the soft material, spacers with different thickness were used. The fibril top face was further covered with a smooth Teflon film covered glass slide. Upon curing, the composite fibril was gently demoulded. Cross-sections of the final fibrils are shown in the optical micrograph in Figure 4.2b.

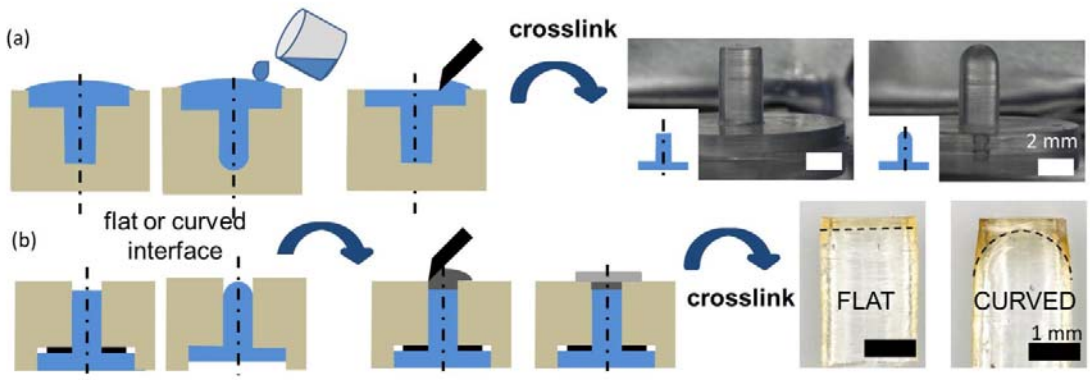

Figure 4.2: Two-step manufacturing process of macroscopic composite fibrils. (a) The fibril stalk is manufactured by filling a prepolymer into a mould with a flat or curved bottom; after the backing layer is flattened using a razor blade, the material is crosslinked. Optical micrographs show exemplary stalk structures. (b) A softer layer is added in a second mould (flat interface). The layer thickness is determined by spacers (in black). The prepolymer of the soft material is covered with a Teflon coated glass slide (in grey) to obtain a flat surface after crosslinking. Optical micrographs show cross sections of final structures. For a more detailed description see (Fischer et al., 2016a).

4.2.3 Adhesion experiments[3]

Normal adhesion experiments were performed using a custom-built, slightly modified setup following Kroner et al. (Kroner et al., 2012a). A nominally flat glass substrate was used as a probe and the specimen was aligned by optical inspection. During the adhesion measurements, a constant velocity of $5\ \mu m/s$ was maintained. Sample and substrate were brought towards each other until a maximum force, i.e. the preload force, was reached and then moved apart until the sample detached from the substrate. Two different characteristic forces were determined: The pull-off force indicates the maximal force that has to be applied to cause full detachment. However, a crack can propagate in a stable manner along the interface or further cracks can be initiated before delamination takes place. Therefore, the force necessary to initiate the first crack was also determined.

For each sample, five different preloads between 40 to 150 mN were applied and all pull-off forces obtained were averaged. The adhesion measurements were repeated at two different positions on the substrate.

4.3 Results

4.3.1 Numerical results

4.3.1.1 Flat interface

The results for axisymmetric ($3D$) composite fibrils with a flat interface, where the total height of the fibril is twice that of the diameter ($L/D = 2$), will be presented in this section. The effects of variations in Young's modulus at constant soft layer thickness ($L_2/L = 0.05$) are reported in Figure 4.3a. The normal stress along the fibril-substrate interface, normalised by the remote stress, is plotted against the normalised distance from the corner, r/D. It is seen that an increase in E_1/E_2 from 1 to 10^6 leads to a progressive decrease in the magnitude of the corner singularity; at the same time, the stress values at the centre of the fibril increase and reach a maximum value of about 0.3. Further increase beyond the ratio of 1000 no longer affects the

[3] Experimental work was performed by S. C. L. Fischer.

stress behaviour significantly, at least for fibrils with $L_2/L = 0.25$ to 0.05. By comparison with the solution for the straight punch fibril (shown as a dashed line), all composite fibrils exhibit lower corner stresses, at the expense of higher centre stresses. The results for plane strain fibrils are reported in Figure B1 in Appendix B.

Figure 4.3b depicts the influence of the thickness L_2 of the softer material at a constant Young's modulus ratio $E_1/E_2 = 10^6$. It can be seen that L_2 exerts a strong influence on the calculated stress distribution: smaller thicknesses reduce the corner stress more significantly and, again, the centre stresses increase until a maximum value of about 0.3 is reached. The plane strain case is again reported in Figure B1 in Appendix B. In order to explain the increase of the centre stress, an asymptotic stress analysis was performed (Appendix A). We consider an axisymmetric cylindrical fibril of diameter D adhering to a rigid flat substrate. The fibril is also rigid other than an infinitesimally thin layer of compliant material at the tip where the fibril adheres to the substrate (i.e., $E_1/E_2 \rightarrow \infty$ and $L_2/L \rightarrow 0$). The solution shows that the tensile stress along the fibril-substrate interface varies with r^2 (equation A 31 in Appendix A) and is therefore greatest at the centre of the fibril. Furthermore, the analysis predicts that the tensile stress at the centre is twice as high as the applied stress (equation A 34 in Appendix A), which is in good agreement with the numerical solution ($\log \sigma_{22}/\sigma_A \approx 0.3$) obtained for high Young's modulus ratios and very thin soft layers.

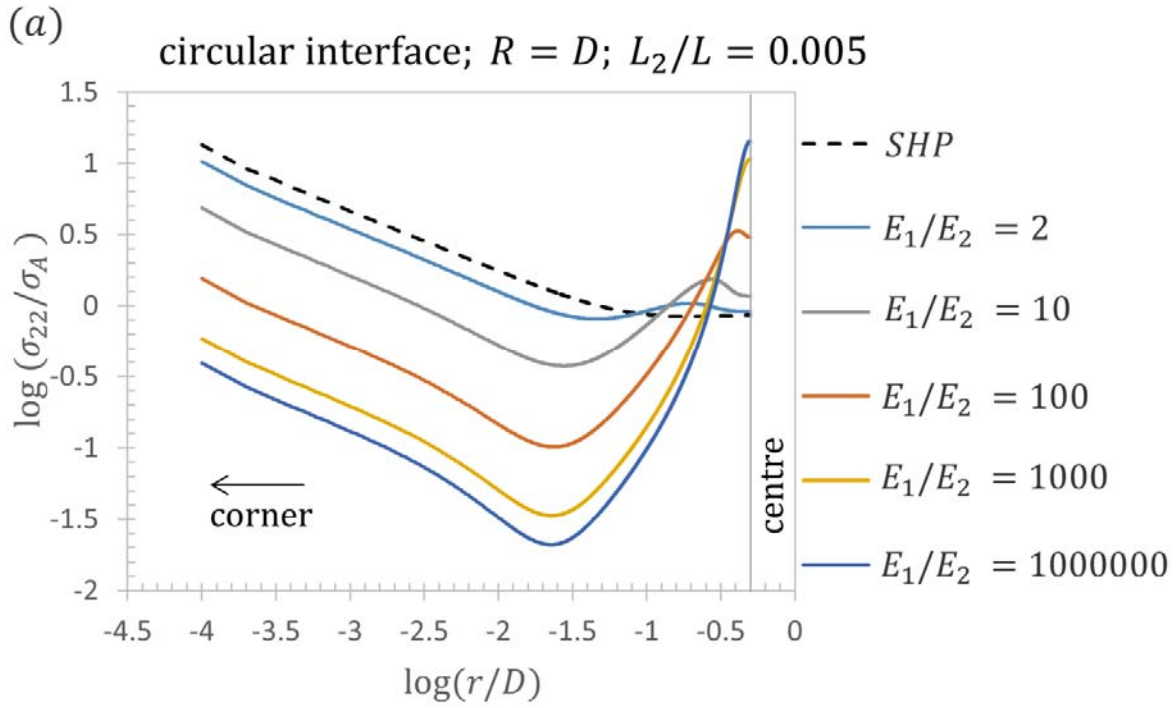
(a)
circular interface; $R = D$; $L_2/L = 0.005$
1.5
1
0.5
0
-0.5
-1
-1.5
-2
$\log(\sigma_{22}/\sigma_A)$
-4.5
-4
-3.5
-3
-2.5
-2
-1.5
-1
-0.5
0
$\log(r/D)$
corner
centre
SHP
$E_1/E_2 = 2$
$E_1/E_2 = 10$
$E_1/E_2 = 100$
$E_1/E_2 = 1000$
$E_1/E_2 = 1000000$

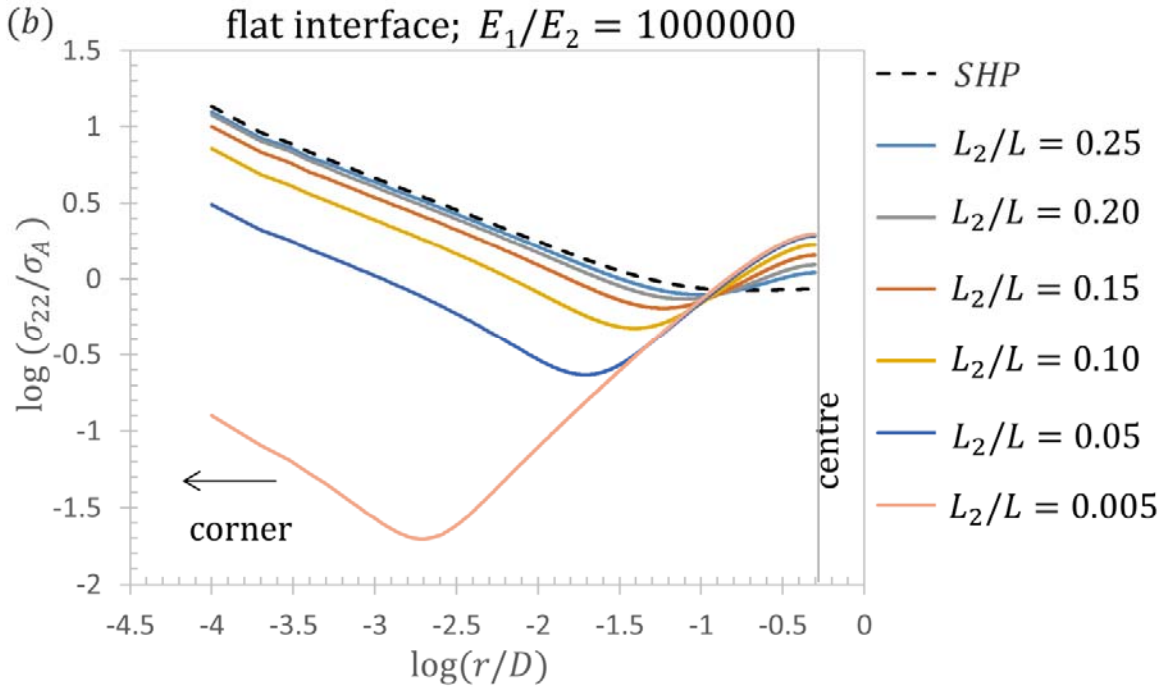
(b)
flat interface; $E_1/E_2 = 1000000$
1.5
1
0.5
0
-0.5
-1
-1.5
-2
$\log(\sigma_{22}/\sigma_A)$
-4.5
-4
-3.5
-3
-2.5
-2
-1.5
-1
-0.5
0
$\log(r/D)$
corner
centre
SHP
$L_2/L = 0.25$
$L_2/L = 0.20$
$L_2/L = 0.15$
$L_2/L = 0.10$
$L_2/L = 0.05$
$L_2/L = 0.005$

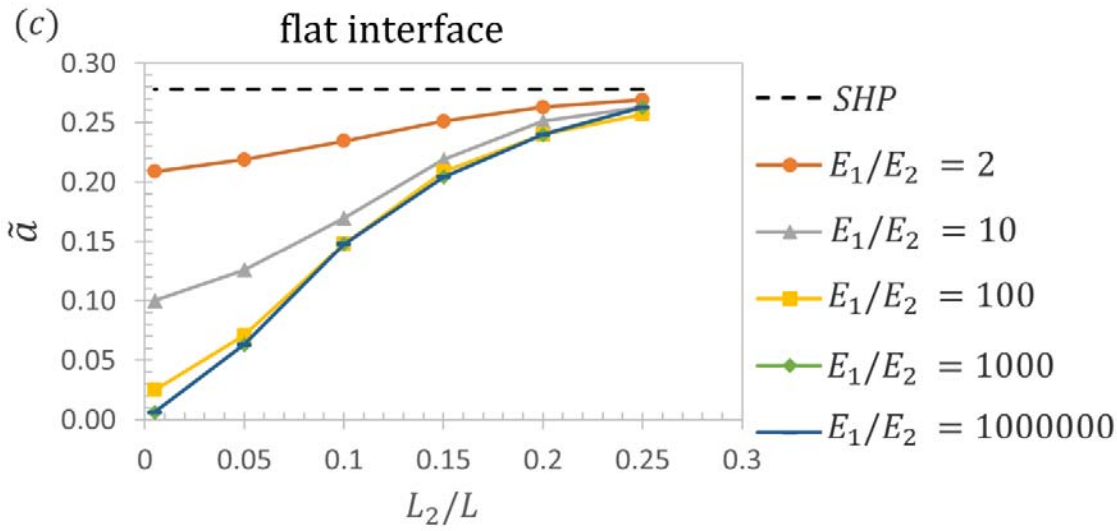

Figure 4.3: Analysis of a composite fibril with flat interface (axisymmetric case). (a) Normalized tensile stress σ_{22}/σ_A along the fibril-substrate interface for different Young's modulus ratios E_1/E_2 at constant $L_2/L = 0.05$. (b) Plots for different combinations of L_2/L at constant $E_1/E_2 = 1000000$. (c) Calibration coefficient for different combinations of L_2/L and E_1/E_2 . The dashed black lines represent the straight homogeneous punch (SHP) results.

The results shown in Figure 4.3a and 3b were fitted with the asymptotic stress solution from equation 3.3 to find the calibration coefficients $\tilde{a}$ for different combinations of E_1/E_2 and L_2/L (Figure 4.3c and Table 4.1). Plane strain results are reported in Figure B1 and Table B1 in Appendix B.

L_2/L	$\tilde{a}$				
	$E_1/E_2 = 2$	$E_1/E_2 = 10$	$E_1/E_2 = 100$	$E_1/E_2 = 1000$	$E_1/E_2 = 1000000$
0.25	0.2692	0.2630	0.2570	0.2570	0.2570
0.2	0.2630	0.2512	0.2399	0.2399	0.2399
0.15	0.2512	0.2188	0.2089	0.2042	0.2042
0.1	0.2344	0.1698	0.1479	0.1479	0.1479
0.05	0.2188	0.1259	0.0708	0.0631	0.0631
0.005	0.2089	0.1000	0.0251	0.0063	0.0063

Table 4.1: Calibration coefficients $\tilde{a}$ for flat interface for the axisymmetric case.

4.3.1.2 Circular interfaces

The normal stress distributions and the calibration coefficients for the two circular interfaces for $R = D$ and $D/2$ can be seen in Figure 4.4 and Figure 4.5 respectively for the axisymmetric case. The corresponding plain strain results are presented in Figure B2 and Figure B3 in Appendix B. The calibration coefficients are provided in Table B2 in Appendix B for the plane strain (Table B2(a)) and axisymmetric case (Table B2(b)).

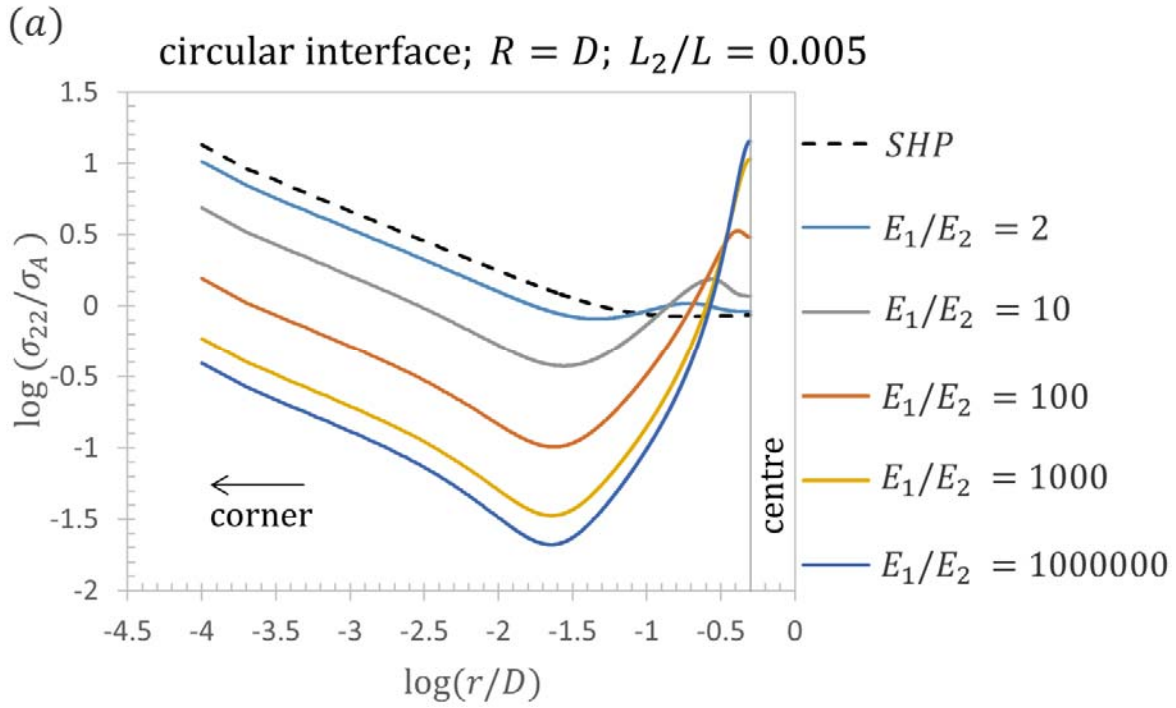
(a)
circular interface; $R = D$; $L_2/L = 0.005$
1.5
1
0.5
0
-0.5
-1
-1.5
-2
$\log(\sigma_{22}/\sigma_A)$
-4.5
-4
-3.5
-3
-2.5
-2
-1.5
-1
-0.5
0
$\log(r/D)$
corner
centre
SHP
$E_1/E_2 = 2$
$E_1/E_2 = 10$
$E_1/E_2 = 100$
$E_1/E_2 = 1000$
$E_1/E_2 = 1000000$

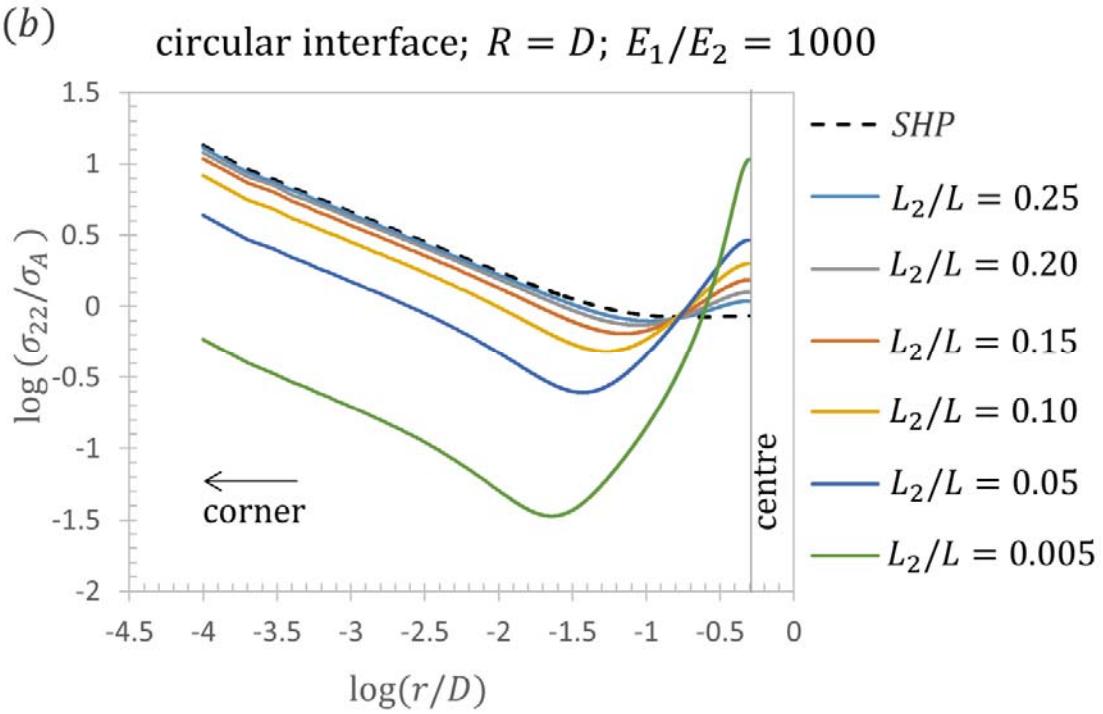
(b)
circular interface; $R = D$; $E_1/E_2 = 1000$
1.5
1
0.5
0
-0.5
-1
-1.5
-2
$\log(\sigma_{22}/\sigma_A)$
-4.5
-4
-3.5
-3
-2.5
-2
-1.5
-1
-0.5
0
$\log(r/D)$
corner
centre
SHP
$L_2/L = 0.25$
$L_2/L = 0.20$
$L_2/L = 0.15$
$L_2/L = 0.10$
$L_2/L = 0.05$
$L_2/L = 0.005$

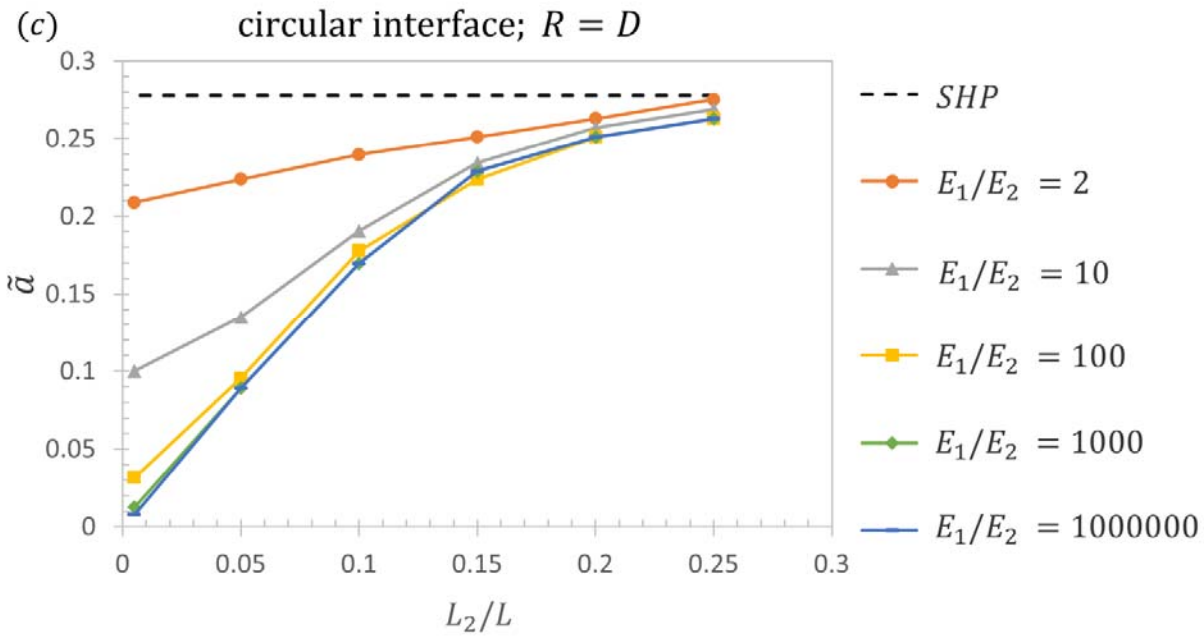

Figure 4.4: Tensile stress σ_{22} along the fibril and substrate interface for a composite fibril with a circular interface ($R = D$) for different combinations of Young's modulus ratio E_1/E_2 and layer thickness ratio L_2/L. The results are reported for the axisymmetric case. The dashed black lines represent the straight homogeneous punch (SHP) results. The colours and symbol shapes reflect the varying parameters E_1/E_2 and L_2/L.

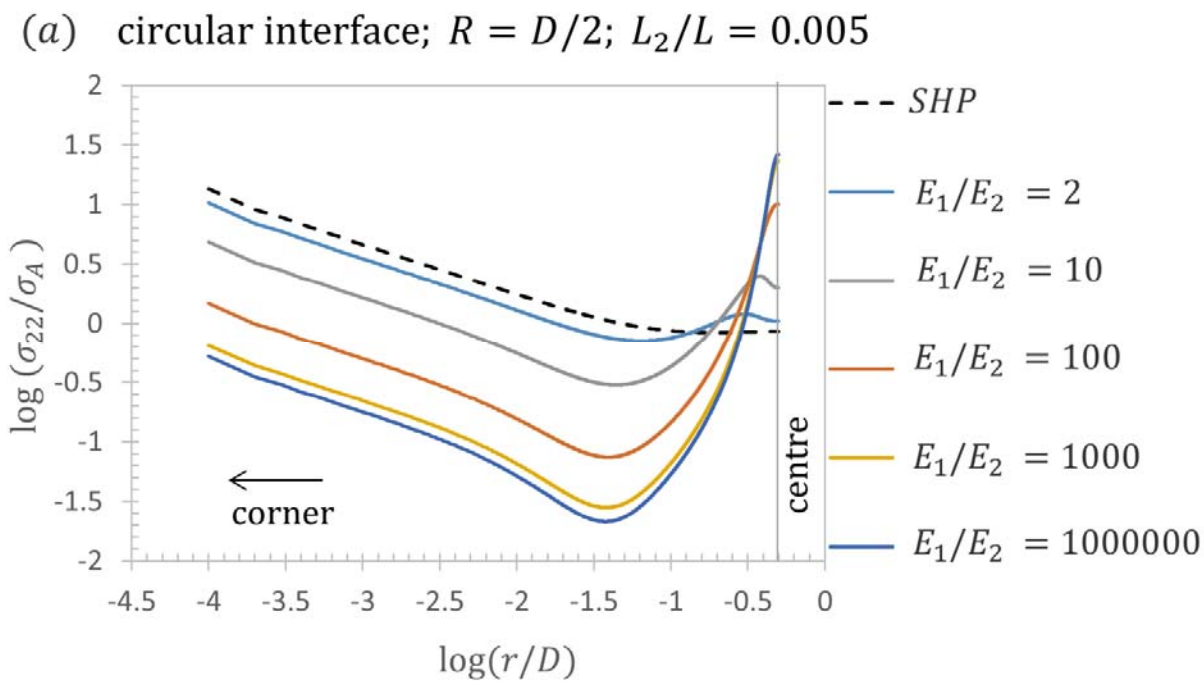
(a) circular interface; $R = D/2$; $L_2/L = 0.005$
SHP
$E_1/E_2 = 2$
$E_1/E_2 = 10$
$E_1/E_2 = 100$
$E_1/E_2 = 1000$
$E_1/E_2 = 1000000$
corner
centre
$\log(\sigma_{22}/\sigma_A)$
$\log(r/D)$

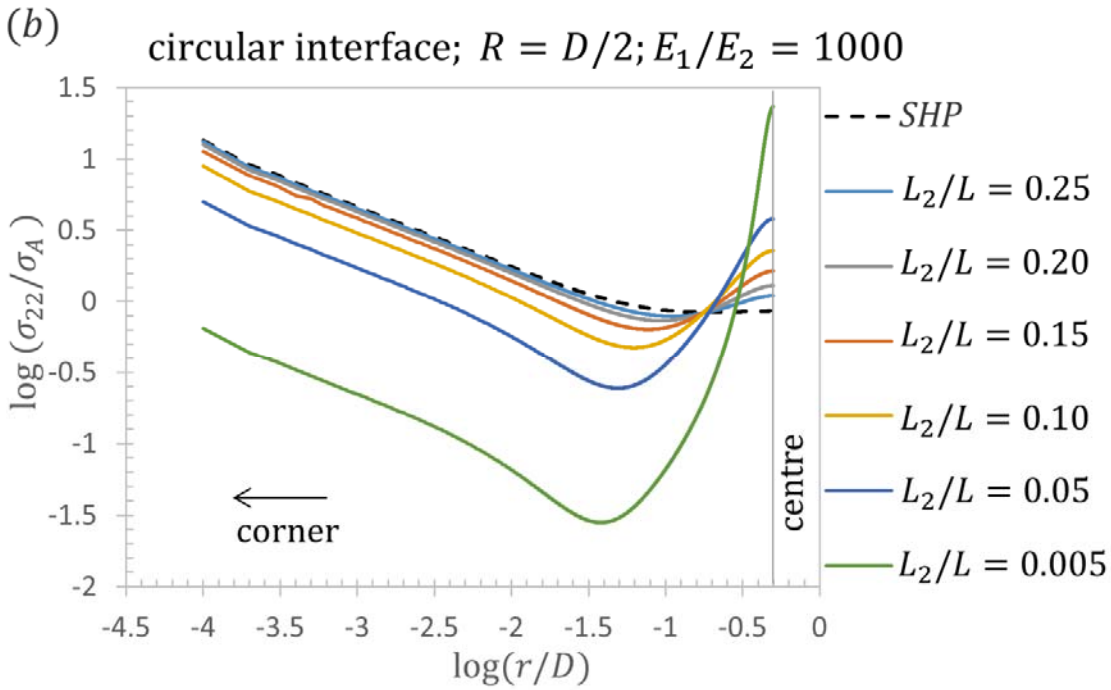
(b) circular interface; $R = D/2$; $E_1/E_2 = 1000$
SHP
$L_2/L = 0.25$
$L_2/L = 0.20$
$L_2/L = 0.15$
$L_2/L = 0.10$
$L_2/L = 0.05$
$L_2/L = 0.005$
corner
centre
$\log(\sigma_{22}/\sigma_A)$
$\log(r/D)$

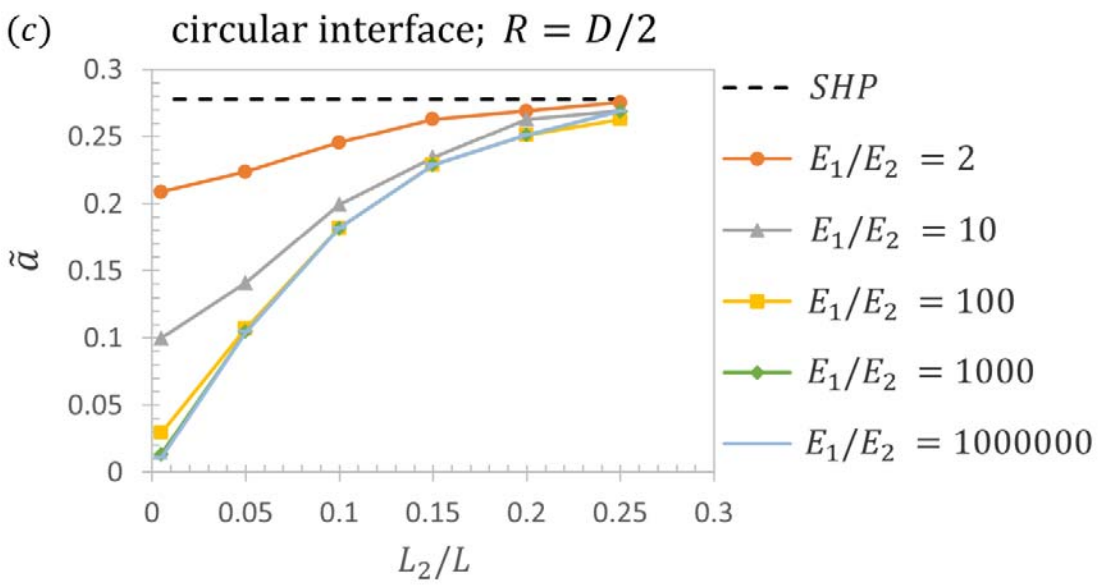

Figure 4.5: Tensile stress σ_{22} along the fibril and substrate interface for a composite fibril with a circular interface ($R = D/2$) for different combinations of Young's modulus ratio E_1/E_2, layer thickness ratio L_2/L and the corresponding calibration coefficients. The results are reported for the axisymmetric case. The dashed black lines represent the straight homogeneous punch (SHP) results. The colours and symbol shapes reflect the varying parameters E_1/E_2 and L_2/L.

4.3.1.3 Elliptical interface

In this section the results of an elliptical interface will be presented where the major axis is equal to twice the diameter D. The influence of the normalised height L_2/L and Young's modulus ratio E_1/E_2 affects the stress pattern along the interface as can be seen in Figure 4.6. When E_1/E_2 is increased and L_2/L is decreased, the magnitude of the singularity decreased for all studied combinations of elliptical interface; a similar behaviour was found for the flat and the circular interface. The plane strain ($2D$) results for different E_1/E_2 and L_2/L are reported in Figure B4 in Appendix B. The calibration coefficients and adhesion strengths are provided in Table B3 in Appendix B for the plane strain (Table B3(a)) and the axisymmetric case (Table B3(b)).

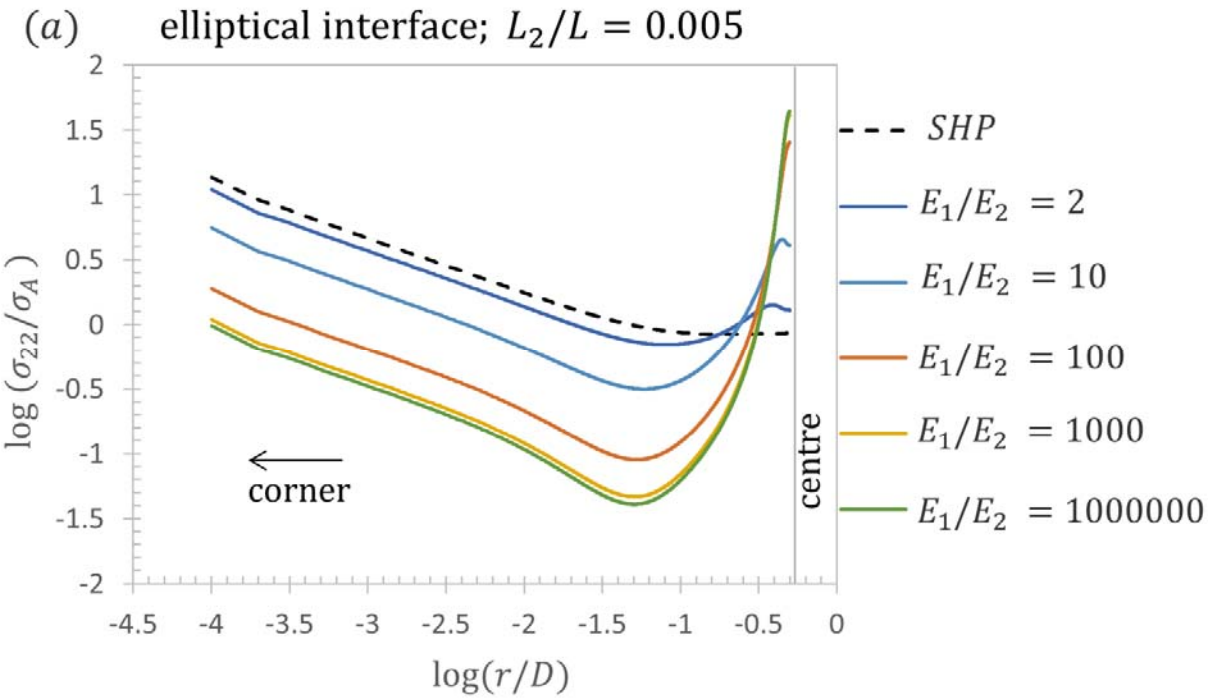
(a)
elliptical interface; $L_2/L = 0.005$
$\log(\sigma_{22}/\sigma_A)$
$\log(r/D)$
corner
centre
SHP
$E_1/E_2 = 2$
$E_1/E_2 = 10$
$E_1/E_2 = 100$
$E_1/E_2 = 1000$
$E_1/E_2 = 1000000$

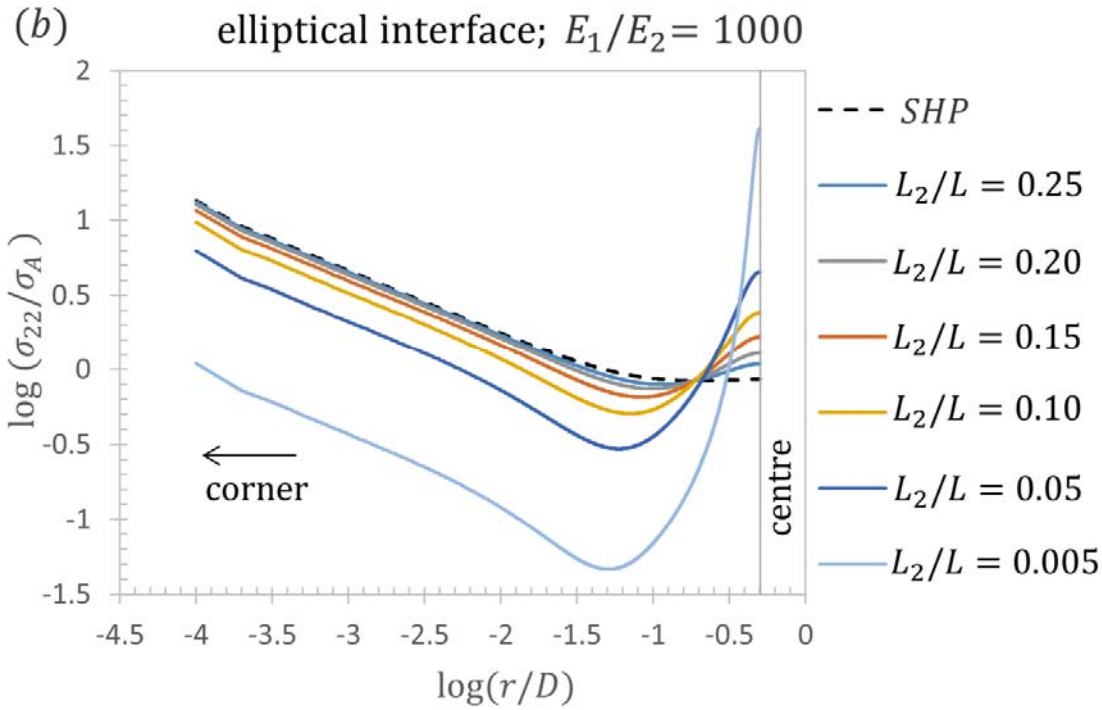
(b)
elliptical interface; $E_1/E_2 = 1000$
$\log(\sigma_{22}/\sigma_A)$
$\log(r/D)$
corner
centre
SHP
$L_2/L = 0.25$
$L_2/L = 0.20$
$L_2/L = 0.15$
$L_2/L = 0.10$
$L_2/L = 0.05$
$L_2/L = 0.005$

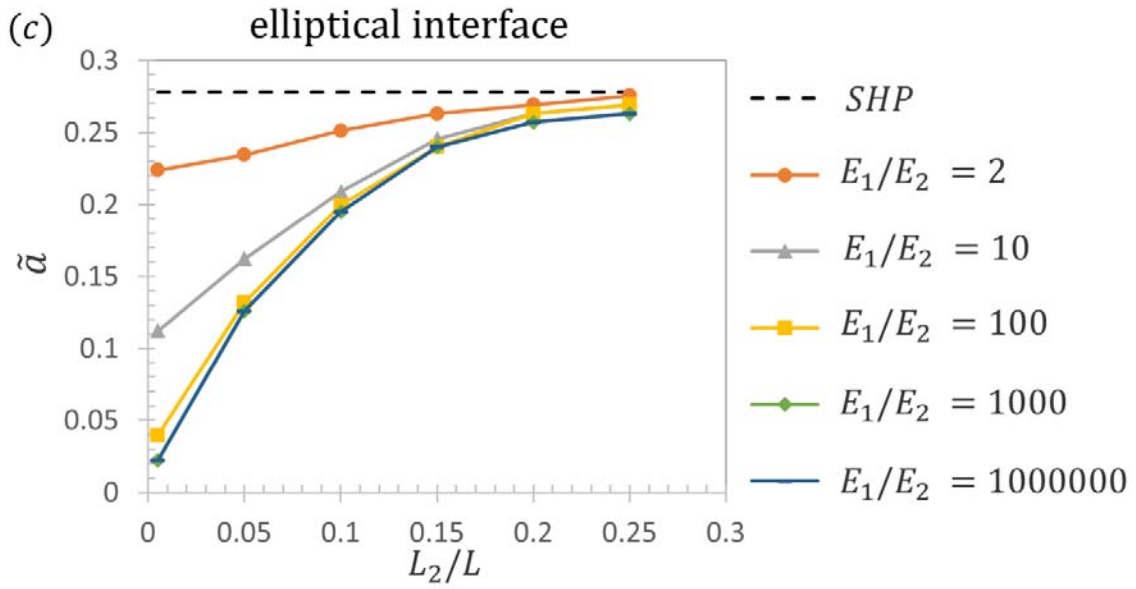

Figure 4.6: Tensile stress σ_{22} along the fibril and substrate interface for a composite fibril with an elliptical interface where the major axis length is twice the diameter D for different combinations of Young's modulus ratio E_1/E_2, layer thickness ratio L_2/L and the corresponding calibration coefficients. The results are reported for the axisymmetric case. The dashed black lines represent the straight homogeneous punch (SHP) results. The colours and symbol shapes reflect the varying parameters E_1/E_2 and L_2/L.

A comparison for the different interface shapes at a constant E_1/E_2 ratio of 1000, but for two different L_2/L ratios of 0.25 and 0.05, is given in Figure 4.7; the corresponding plane strain comparison can be seen in Figure B5 in Appendix B. It can be observed that for $L_2/L = 0.25$ the influence of interface shape is insignificant as all curves collapse and approach the straight homogeneous punch (SHP) case. For thinner soft layers (e.g., $L_2/L = 0.05$), interface shape strongly influences the distribution of stress along the interface: In the case of $R = D$ and $L_2/L = 0.05$, the centre stress is 2.9 times the applied stress (Figure 4.7) which is similar to the value of 3.3 calculated analytically (equation A 37 in Appendix A). For even thinner soft layers ($L_2/L = 0.005$), the centre stress rises up to 14.1 and 15.2 times the applied stress in the numerical solution (Figure 4.4) and the analytical solution (equation A 37 in Appendix A), respectively. Hence, thinner soft layers create higher centre stresses. By increasing the radius of

the interface curvature, the corner and the centre stress are slightly reduced. The flat interface is most efficient in reducing both the corner stress and the centre stress.

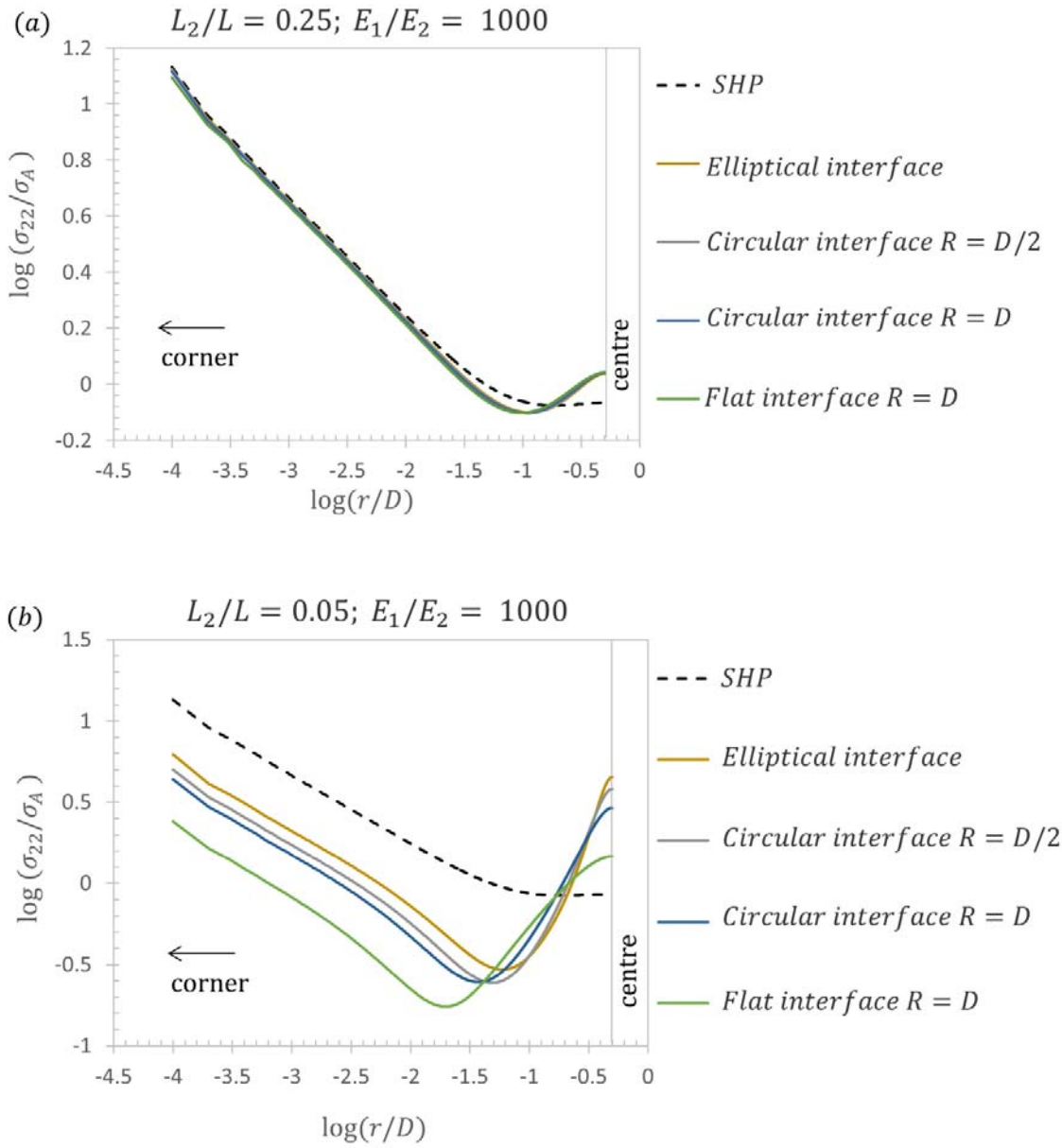

Figure 4.7: Normalized stress σ_{22}/σ_A along the fibril-substrate interface for fibrils with different interface shapes, E_1 / E_2 = 1000 and L_2/L = 0.25 (a) and 0.05 (b) (axisymmetric case). The dashed black lines represent the straight homogeneous punch (SHP) results.

4.3.2 Adhesion strength

The normalized adhesion strength S^I/S^{punch} was calculated by using equations 4.2 and 4.3. The results for flat and circular interfaces and various L_2/L and E_1/E_2 ratios are shown in Figure 4.8 and Table 4.2. The corresponding plane strain results are given in Figure B6 and Table B4. It is seen that both parameters, which are design parameters for composite fibrils, affect adhesion: smaller layer thicknesses and higher Young's modulus ratios result in higher adhesion strength. Close inspection shows that the interface curvature becomes important only for very thin soft layers ($L_2/L < 0.05$), where the flat interface showed highest adhesion.

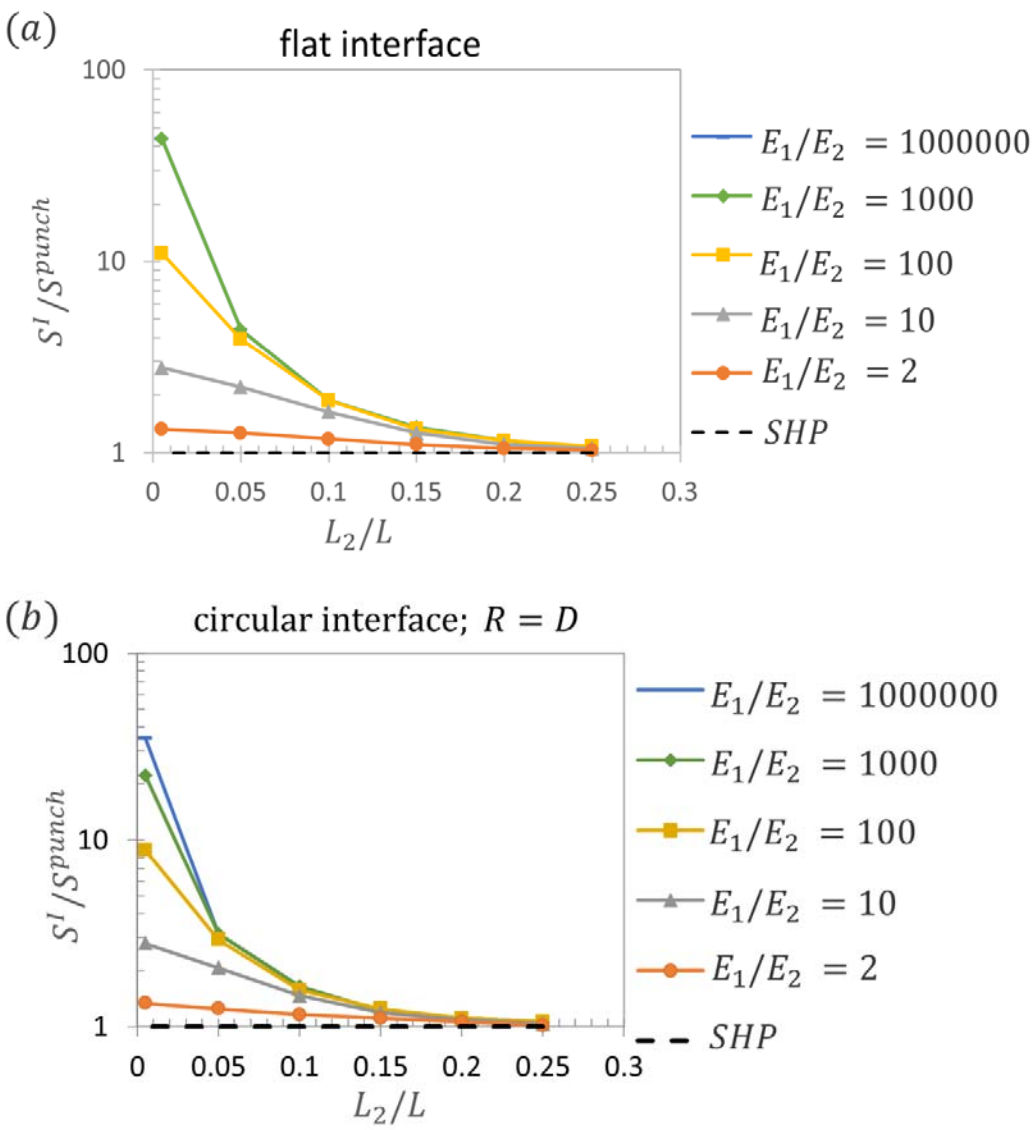

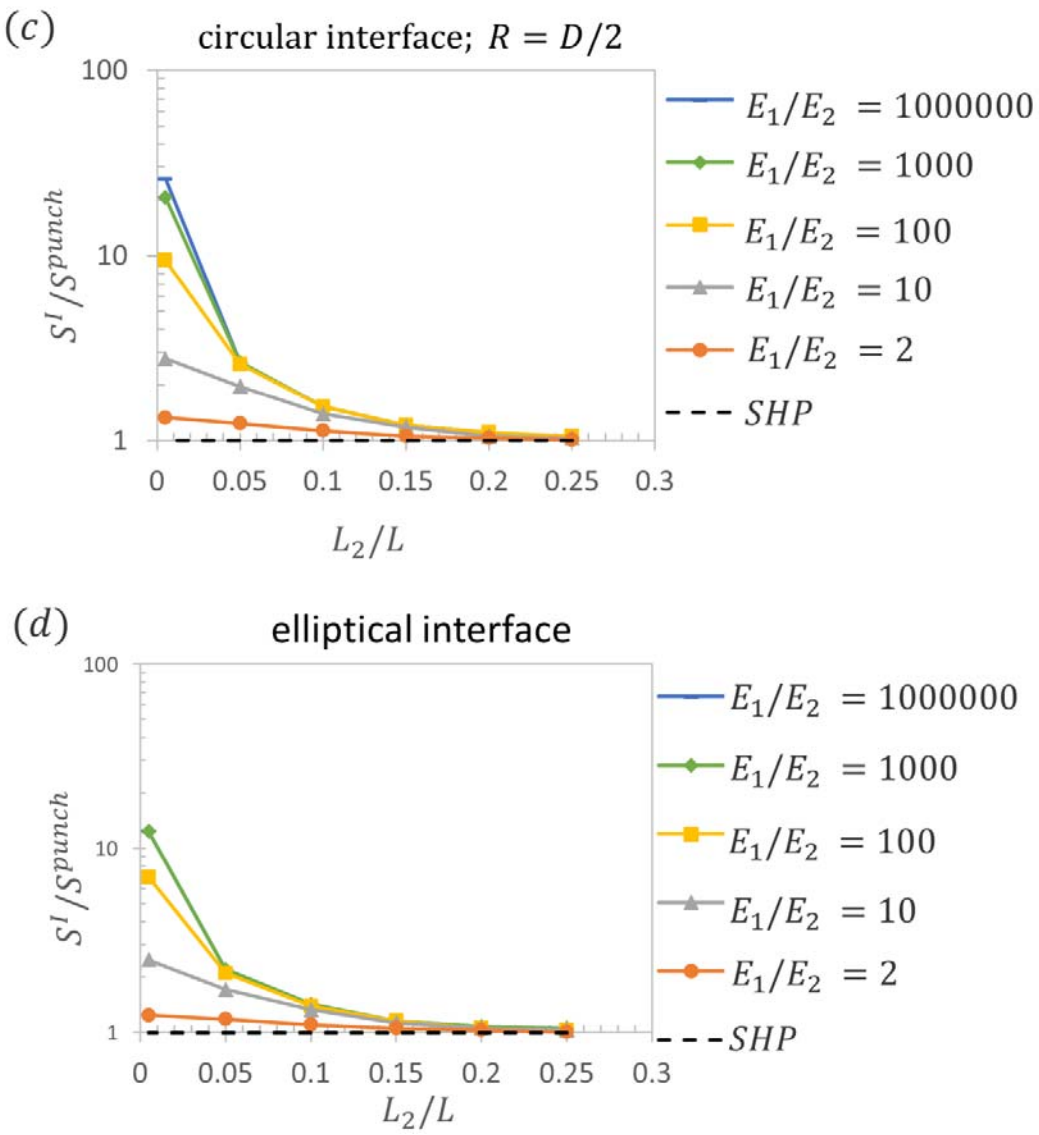

Figure 4.8: Calculated influence of Young's modulus ratio on adhesive strength, normalized to that of a flat punch, with the following interface shapes: (a) flat, (b) circular with radius $R = D$ *, (c)* $R = D/2$ *and (d) elliptical. The dashed black lines represent the straight homogeneous punch (SHP) results. The different Young's modulus ratios are* $E_1/E_2 = 2$ *(orange, circles),* 10 *(grey, triangles),* 100 *(gold, squares),* 1000 *(green, diamonds) and* 1000000 *(blue, dashes).*

S_I/S_A	$E_1/E_2 = 2$				$E_1/E_2 = 10$				$E_1/E_2 = 100$				$E_1/E_2 = 1000$				$E_1/E_2 = 1000000$			
	FI	*CI*		*EI*	*FI*	*CI*		*EI*	*FI*	*CI*		*EI*	*FI*	*CI*		*EI*	*FI*	*CI*		*EI*
L_2/L	*R=∞*	*R=D*	*R=D/2*		*R=∞*	*R=D*	*R=D/2*		*R=∞*	*R=D*	*R=D/2*		*R=∞*	*R=D*	*R=D/2*		*R=∞*	*R=D*	*R=D/2*	
0.25	1.03	1.01	1.01	1.01	1.06	1.03	1.03	1.03	1.08	1.06	1.06	1.03	1.06	1.06	1.03	1.06	1.06	1.06	1.03	1.06
0.2	1.06	1.06	1.03	1.03	1.11	1.08	1.06	1.06	1.16	1.11	1.11	1.06	1.16	1.11	1.11	1.08	1.16	1.11	1.11	1.08
0.15	1.11	1.11	1.06	1.06	1.27	1.19	1.19	1.13	1.33	1.24	1.21	1.16	1.36	1.21	1.21	1.16	1.36	1.21	1.21	1.16
0.1	1.19	1.16	1.13	1.11	1.64	1.46	1.39	1.33	1.88	1.56	1.53	1.39	1.88	1.64	1.53	1.43	1.88	1.64	1.53	1.43
0.05	1.27	1.24	1.24	1.19	2.21	2.06	1.97	1.71	3.93	2.91	2.59	2.11	4.41	3.12	2.65	2.21	4.41	3.12	2.65	2.21
0.005	1.33	1.33	1.33	1.24	2.78	2.78	2.78	2.48	11.07	8.79	9.42	6.98	44.06	22.08	20.61	12.42	44.06	35.00	25.94	12.42

Table 4.2: Adhesion strength values for different interfaces which include flat (FI), circular

(CI) for two different radius $R = D$ and $D/2$ and elliptical (EI) represented as adhesion of composite fibrils normalised by that of a straight homogeneous punch.

4.3.3 Experimental results[4]

While the stress distribution along the substrate-fibril interface is not directly accessible in experiments, the adhesion strength was defined as the normal pull-off force divided by the total apparent contact area of $A = 3.14\ \mathrm{mm}^2$. The adhesion performance of a straight punch fibril and one with a flat interface and a circular interface $(R = D/2)$ for two elastic modulus ratios $E_1/E_2 = 2$ and 350 were studied. By dividing the adhesion strengths of the composites by those of the straight punch fibril, a normalization was achieved for direct comparison with the numerical results.

The normalized adhesion strengths for flat and circular interface structures are shown in Figure 4.9 along with the predictions from the numerical simulations for very similar Young's modulus ratios. Each point in the graph represents the average value of all measurements performed with one sample, the errors being smaller than the symbol size. The absolute pull-off forces measured for the composite fibrils were always higher than for the reference fibril made entirely from the soft material (i.e., the straight punch case). Two regimes of the experimental data can be distinguished:

i) Regime of large soft layer thickness: Provided $L_2/L > 0.06$ for $E_1/E_2 = 350$ and $L_2/L > 0.03$ for $E_1/E_2 = 2$, the measured adhesion strength increased with decreasing L_2/L ratio for both interface shapes. In this regime, the increase in adhesion was found to be higher for the flat interface than for the curved interface. This trend is reflected in the simulations. Optical microscopy of the interfaces showed that cracks were always initiated at the contact edges and propagated to cause fast delamination. Therefore, no differences between pull-off and crack initiation forces were observed.

[4] Experimental work was performed by S. C. L. Fischer.

ii) Regime of small soft layer thickness: For soft layers with L_2/L ratios smaller than 0.06 ($E_1/E_2 = 350$) or than 0.03 ($E_1/E_2 = 2$), detachment occurred by a different mechanism and seemed to depend on interface shape. For flat interfaces (Figure 4.9a), a drop in adhesion strength was observed. The detachment mechanism changed from single edge crack to several finger-like cracks which propagated radially towards the centre of the fibril; this detachment mechanism is reminiscent of earlier studies on thin soft films (Nase et al., 2008). By contrast, the fibrils with the circular interface (Figure 4.9b), showed a steady increase of the adhesion strength with decreasing L_2/L ratio. Here, a transition from edge to centre cracks could be observed. Interestingly, the primary crack did not cause fast detachment, but grew in a stable manner up to a critical diameter of more than half of the total diameter. Therefore, the pull-off forces were much larger than the crack initiation forces as is indicated by the arrows in Figure 4.9b.

4.4 Discussion

A novel concept for designing bioinspired dry adhesives was introduced in this chapter: comparatively stiff fibrils with a thin soft material layer on the terminal face. Numerical results demonstrated that such composite fibrils have reduced stress singularities at the contact edges, which typically control the detachment of flat punch fibrils from substrates (Akisanya and Fleck, 1997; Khaderi et al., 2015). Stronger adhesion is achieved by reducing the corner stresses; this is similar to the findings previously reported for mushroom fibrils, where the gradually widening terminal face results in a more uniform stress distribution and strongly enhanced adhesion (Balijepalli et al., 2016; del Campo et al., 2007; Gorb et al., 2007b). Our composite fibril design, by contrast, exhibits a uniform axial cross-sectional area with several possible advantages: fibrils without re-entrant corners are easier to fabricate and will be less prone to elastic collapse, which is known to counteract adhesion.

Our parametric study reveals a counter-intuitive trend: thinner soft layers (with smaller L_2/L) create substantially better adhesion. The reason is that, for all Young's modulus ratios, a smaller layer thickness results in a decreased corner stress while the stress at the centre is increased. Recently, a similar trend was found by Minsky and Turner (Minsky and Turner, 2015), who studied a different, but related fibril geometry. A stiff fibril stalk, when fully coated with a thin soft polymer layer, exhibited improved adhesion, based on a cohesive zone model. However

their results were limited to only one elastic modulus ratio. In our work, the variation of that ratio also affects the tensile stress distribution along the fibril-substrate interface, with higher ratios leading to significantly better adhesion. However, when $L_2/L > 0.05$, the effect decreases for higher ratios and disappears for a Young's modulus ratio exceeding three orders of magnitude. Interestingly, the composite fibrils of ladybugs (Peisker et al., 2013) exhibit a modulus ratio of such a magnitude, and not more.

Out of the different interface shapes examined, the adhesion of a composite fibril with a flat interface shows the lowest maximum stress at the corner and the centre along the fibril-substrate interface. The simulations indicate that higher curvatures of circular interfaces lead to higher stresses at the centre and the edge compared to the flat interface.

It is instructive to examine more closely the correlation between our numerical results and the experimental measurements on single macroscopic composite fibrils. While the agreement is not perfect, the trend to higher normalized adhesion strength with decreasing layer thickness is also found in the experiments (Figure 4.9). What is not found in the calculations is the drop in adhesion strength seen in the flat interface fibril for small L_2/L ratios. It is very likely that this is caused by an alternative detachment mechanism not considered in the model, i.e. finger-like crack growth starting from the edge as observed in Figure 4.9a. Such a behaviour is well known in interface mechanics as the Saffman–Taylor instability (Derks et al., 2003; Nase et al., 2011; Shull and Creton, 2004). Interestingly, the transition from single-edge crack propagation to delamination by instabilities depends on the stiffness of the stalk.

In the case of the circular interfaces, a drop of adhesion strength was not found in the experiments although a change in detachment mechanism initiated by centre cracks occurred (Figure 4.9b). The mechanism change is in agreement with the numerical calculations, which predict a strong increase of the centre stress when the soft layer becomes thinner. Why the presence of centre cracks still leads to increasing adhesion strengths is a matter of conjecture. A possible explanation lies in the steep decrease of the stress from the centre to the edges (see Figure 4.7), which may induce stable crack propagation. Incorporation of this additional mechanism into the numerical calculations would be possible (see, for instance, (Balijepalli et al., 2016)), but is beyond the scope of the present study.

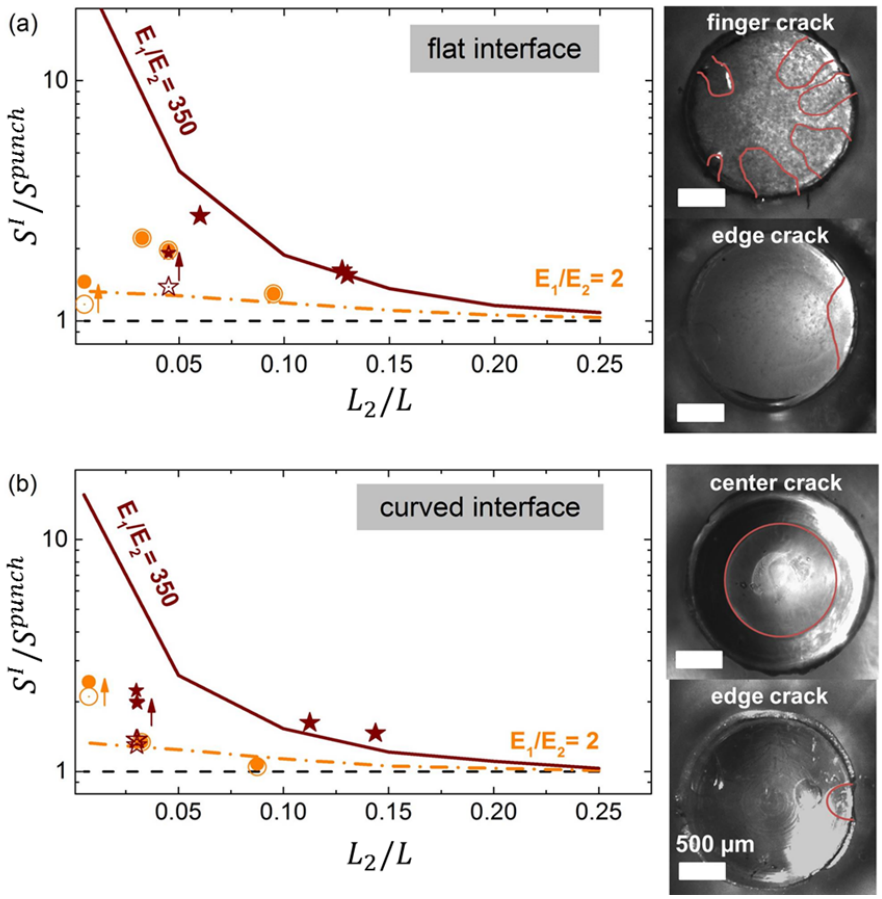

Figure 4.9: Comparison of normalized adhesion strengths from experiments (symbols) and numerical calculations (lines) for composite fibrils with (a) flat interface and (b) circular interface $(R = D/2)$ *for* $E_1/E_2 = 2$ *and* 350*. The lines refer to calculations for a straight homogeneous punch (black, dashed), and a composite fibril with* $E_1/E_2 = 2$ *(orange, dashes and dots) and* 350 *(red, solid). Light green circles represent experiments with* $E_1/E_2 = 2$ *and dark green stars with* $E_1/E_2 = 350$*. Filled symbols represent pull-off forces, empty symbols crack initiation forces. Arrows indicate the samples for which the two forces differ significantly. Optical micrographs represent the characteristic detachment mechanisms that were observed for (a) flat and (b) circular interfaces depending on the soft layer thickness. The crack fronts are highlighted by red lines.*

Overall, we believe that our research provides an promising alternative for straight homogeneous punch or mushroom-type fibrils. The more benign stress distribution of the composite fibrils is

reminiscent of the effect found in previous studies for mushroom fibrils while reducing the manufacturing complexity. Additionally, our geometry allows for the use of softer materials, as the stiffer stalk will stabilize the fibrils against collapse or clustering. The combination of numerical calculations with model experiment has hence provided us with new insight which will be valuable for the optimization of micropatterned dry adhesive surfaces. A more detailed experimental study of these composite fibrils is currently underway (Fischer et al., 2016a).

4.5 Conclusion

In this investigation, we demonstrated the potential of composite fibril structures that combine relatively stiff stalks with very soft tip layers. With this design, high aspect ratio structures with straight sidewalls can be manufactured without the risk of thin flaps collapsing. The soft material forming the tip of the microstructures provides a benign stress distribution and high adaptability to the substrate while the stiffer underlying material ensures mechanical stability. The following conclusions can be drawn:

- The adhesion of composite fibrillar structures can be tuned by varying the Young's modulus of the two material components, by manipulating the curvature of their interface, and by changing the soft layer thickness.
- Thinner soft layers (smaller L_2/L) are found to result in higher adhesive strength.
- Higher Young's modulus ratios (E_1/E_2) increase the adhesive strength provided that detachment is controlled by the corner singularity.
- Flat interfaces lead to better adhesion than curved interfaces for the case of edge crack detachment. For very thin soft layers, the experimentally observed detachment is different and depends on the interface curvature. Thus, detachment from the centre provoked by a curved interface may result in better adhesion.
- The experimental results can be explained reasonably well by the numerical simulations as long as detachment occurs by edge cracks. Below a certain limit of L_2/L ratios a transition from edge crack to centre crack or finger cracks occurred in the experiments; these mechanisms are not yet part of the calculations.

Appendix A: Asymptotic analysis of the stress in a stiff adherent axisymmetric cylindrical fibril with a thin compliant layer at its tip

We consider a circular cylindrical fibril of diameter D adhering to a rigid flat substrate. The fibril is also rigid other than a thin layer of compliant material at the tip where the fibril adheres to the substrate. The geometry is axisymmetric. The compliant material is incompressible and linear elastic with shear modulus μ. The relevant equilibrium equations are

$$\begin{aligned} &\frac{\partial \tilde{\sigma}_{rr}}{\partial \tilde{r}} + \frac{\tilde{\sigma}_{rr} - \tilde{\sigma}_{\theta\theta}}{\tilde{r}} + \frac{\partial \tilde{\sigma}_{rz}}{\partial \tilde{z}} = 0 \\ &\frac{\partial \tilde{\sigma}_{rz}}{\partial \tilde{r}} + \frac{\tilde{\sigma}_{rz}}{\tilde{r}} + \frac{\partial \tilde{\sigma}_{zz}}{\partial \tilde{z}} = 0 \end{aligned} \qquad \text{A 1}$$

where the stress components are given in cylindrical polar coordinates and $\tilde{r}, \theta, \tilde{z}$ are those cylindrical polar coordinates. The elasticity relationships are

$$\begin{aligned} &\frac{\partial \tilde{u}_r}{\partial \tilde{r}} = \frac{1}{2\mu}\left(\tilde{\sigma}_{rr} + \tilde{p}\right) \\ &\frac{\tilde{u}_r}{\tilde{r}} = \frac{1}{2\mu}\left(\tilde{\sigma}_{\theta\theta} + \tilde{p}\right) \\ &\frac{\partial \tilde{u}_z}{\partial \tilde{z}} = \frac{1}{2\mu}\left(\tilde{\sigma}_{zz} + \tilde{p}\right) \\ &\frac{\partial \tilde{u}_z}{\partial \tilde{r}} + \frac{\partial \tilde{u}_r}{\partial \tilde{z}} = \frac{\tilde{\sigma}_{rz}}{\mu} \end{aligned} \qquad \text{A 2}$$

where $\tilde{u}_r$ and $\tilde{u}_z$ are the axial displacements and $\tilde{p} = -\left(\tilde{\sigma}_{rr} + \tilde{\sigma}_{\theta\theta} + \tilde{\sigma}_{zz}\right)/3$ is the pressure, *i.e.* the negative of the hydrostatic stress. Incompressibility is embedded in equation A 2 but can also be stated as

$$\frac{\partial \tilde{u}_r}{\partial \tilde{r}} + \frac{\tilde{u}_r}{\tilde{r}} + \frac{\partial \tilde{u}_z}{\partial \tilde{z}} = 0 \qquad \text{A 3}$$

The boundary conditions are

$$\tilde{u}_r = \tilde{u}_z = 0 \text{ on } \tilde{z} = 0 \qquad \text{A 4}$$

and

$$\begin{aligned} \tilde{u}_r &= 0 \\ \tilde{u}_z &= \Delta \end{aligned} \qquad \text{on } \tilde{z} = \tilde{h}(\tilde{r}) \qquad \text{A 5}$$

where Δ is the upward displacement of the rigid segment of the fibril and $\tilde{z} = \tilde{h}(\tilde{r})$ is the interface between the complaint layer and the rigid segment of the fibril. We assume that $\tilde{h}(\tilde{r}) << D$ so that the complaint layer is thin compared to the diameter of the fibril. The traction boundary conditions are

$$\tilde{\sigma}_{rr}\left(\frac{D}{2}, \tilde{z}\right) = 0 \text{ and } \tilde{\sigma}_{rz}\left(\frac{D}{2}, \tilde{z}\right) = 0 \qquad \text{A 6}$$

Now define the parameter η such that $\eta = \tilde{h}(D/2)$. It follows that $\eta << D$ and thus $\delta = 2\eta / D << 1$ is a small parameter. Now normalize lengths such that $\tilde{r} = Dr/2$, $\tilde{z} = \eta z$, and the displacements are such that $\tilde{u}_r = \Delta u_r$ and $\tilde{u}_z = \Delta u_z$. It follows that u_z, r and z are $O(1)$. We normalize the stresses by Σ, to be determined, such that $\tilde{\sigma}_{ij} = \Sigma \sigma_{ij}$. However, we specify that σ_{zz} is $O(1)$, so that Σ is the order of the stress applied to the fibril. As a result of the normalizations, the equations become as follows. For equilibrium we have

$$\begin{aligned} &\delta \frac{\partial \sigma_{rr}}{\partial r} + \delta \frac{\sigma_{rr} - \sigma_{\theta\theta}}{r} + \frac{\partial \sigma_{rz}}{\partial z} = 0 \\ &\delta \frac{\partial \sigma_{rz}}{\partial r} + \delta \frac{\sigma_{rz}}{r} + \frac{\partial \sigma_{zz}}{\partial z} = 0 \end{aligned} \qquad \text{A 7}$$

For elasticity we deduce that

$$\frac{2\Delta\partial u_r}{D\partial r} = \frac{\Sigma}{2\mu}\left(\sigma_{rr} + p\right)$$
$$\frac{2\Delta u_r}{Dr} = \frac{\Sigma}{2\mu}\left(\sigma_{\theta\theta} + p\right)$$
$$\frac{\Delta\partial u_z}{\eta\partial z} = \frac{\Sigma}{2\mu}\left(\sigma_{zz} + p\right) \qquad \text{A 8}$$
$$\frac{2\Delta\partial u_z}{D\partial r} + \frac{\Delta\partial u_r}{\eta\partial z} = \frac{\Sigma\sigma_{rz}}{\mu}$$

where $\tilde{p} = \Sigma p$, incompressibility becomes

$$\delta\frac{\partial u_r}{\partial r} + \delta\frac{u_r}{r} + \frac{\partial u_z}{\partial z} = 0 \qquad \text{A 9}$$

and the boundary conditions are

$$u_r = u_z = 0 \text{ on } z = 0 \qquad \text{A 10}$$

$$u_r = 0 \text{ on } z = \tilde{h}\left(r\right)/\eta \qquad \text{A 11}$$

$$u_z = 1 \text{ on } z = \tilde{h}\left(r\right)/\eta \qquad \text{A 12}$$

and

$$\sigma_{rr}\left(1,z\right) = 0 \text{ and } \sigma_{rz}\left(1,z\right) = 0 \qquad \text{A 13}$$

From the set of equations above we deduce that to satisfy incompressibility u_r must be $O\left(1/\delta\right)$, *i.e.* much bigger than u_z. The first of equation A 7 shows that σ_{rz}/σ_{rr} is $O\left(\delta\right)$ and we assume that σ_{zz} and σ_{rr} are the same order of magnitude. Therefore σ_{rz} is $O\left(\delta\right)$. Inspection of the last of equation A 8 then allows us to deduce that $\Delta/\eta\delta$ and $\Sigma\delta/\mu$ are of the same order. Therefore, we write $\Sigma = \Delta\mu/\eta\delta^2$. As a consequence, equation A 8 becomes

$$
\begin{aligned}
&\delta^3 \frac{\partial u_r}{\partial r} = \frac{1}{2}\left(\sigma_{rr} + p\right) \\
&\delta^3 \frac{u_r}{r} = \frac{1}{2}\left(\sigma_{\theta\theta} + p\right) \\
&\delta^2 \frac{\partial u_z}{\partial z} = \frac{1}{2}\left(\sigma_{zz} + p\right) \\
&\delta^3 \frac{\partial u_z}{\partial r} + \delta^2 \frac{\partial u_r}{\partial z} = \sigma_{rz}
\end{aligned}
\qquad \text{A 14}
$$

This immediately tells us that the deviatoric stresses are no greater than $O(\delta)$. Therefore, we deduce that we can expand the stresses asymptotically as

$$
\begin{aligned}
&p = p^{(0)} + \delta p^{(1)} + O\left(\delta^2\right) \\
&\sigma_{rr} = -p^{(0)} - \delta p^{(1)} + \delta^2 \sigma_{rr}^{(2)} + O\left(\delta^3\right) \\
&\sigma_{\theta\theta} = -p^{(0)} - \delta p^{(1)} + \delta^2 \sigma_{\theta\theta}^{(2)} + O\left(\delta^3\right) \\
&\sigma_{zz} = -p^{(0)} - \delta p^{(1)} + \delta^2 \sigma_{zz}^{(2)} + O\left(\delta^3\right) \\
&\sigma_{rz} = \delta \sigma_{rz}^{(1)} + O\left(\delta^2\right)
\end{aligned}
\qquad \text{A 15}
$$

where the terms with the parenthetical superscripts are $O(1)$. We have therefore assumed that the stresses are hydrostatic to leading order and that deviatoric stress terms are $O(\delta)$. This means that the applied load in the thin layer is supported to leading order by the hydrostatic stress, arising because of the incompressibility of the material. Similarly, we expand the displacements as

$$
\begin{aligned}
&u_r = \frac{1}{\delta} u_r^{(-1)} + u_r^{(o)} + O(\delta) \\
&u_z = u_r^{(o)} + \delta u_r^{(1)} + O\left(\delta^2\right)
\end{aligned}
\qquad \text{A 16}
$$

which is consistent with our deductions above.

We substitute equation A 15 into equation A 7 and obtain to leading order for equilibrium

$$-\frac{\partial p^{(0)}}{\partial r}+\frac{\partial \sigma_{rz}^{(1)}}{\partial z}=0$$
$$-\frac{\partial p^{(0)}}{\partial z}=0 \qquad \text{A 17}$$

The stress strain relationships to leading order become

$$\frac{\partial u_r^{(-1)}}{\partial r}=\frac{1}{2}\left(\sigma_{rr}^{(2)}+p^{(2)}\right)$$
$$\frac{u_r^{(-1)}}{r}=\frac{1}{2}\left(\sigma_{\theta\theta}^{(2)}+p^{(2)}\right)$$
$$\frac{\partial u_z^{(0)}}{\partial z}=\frac{1}{2}\left(\sigma_{rr}^{(2)}+p^{(2)}\right) \qquad \text{A 18}$$
$$\frac{\partial u_r^{(-1)}}{\partial z}=\sigma_{rz}^{(1)}$$

Incompressibility to leading order is then

$$\frac{\partial u_r^{(-1)}}{\partial r}+\frac{u_r^{(-1)}}{r}+\frac{\partial u_z^{(0)}}{\partial z}=0 \qquad \text{A 19}$$

Since there is no equation in which $p^{(1)}$ appears, we conclude it must be zero.

We now proceed to solve the equations, A 17, A 18 and A 19. The 2nd of equation A 17 tells us that $p^{(0)}$ is independent of z and thus

$$p^{(0)}=p^{(0)}(r) \qquad \text{A 20}$$

The 1st of equation A 17 thus gives us

$$\frac{\partial \sigma_{rz}^{(1)}}{\partial z}=\frac{dp^{(0)}(r)}{dr} \qquad \text{A 21}$$

which can be integrated to give

$$\sigma_{rz}^{(1)} = \tau(r) + z\frac{dp^{(0)}(r)}{dr} \qquad \text{A 22}$$

where $\tau(r)$ is the as yet unknown value of the normalized shear stress at the interface with the substrate. The result from equation A 22 may be inserted into the 4th of equation A 18 to give

$$\frac{\partial u_r^{(-1)}}{\partial z} = \tau(r) + z\frac{dp^{(0)}(r)}{dr} \qquad \text{A 23}$$

This integrates to give

$$u_r^{(-1)} = z\tau(r) + \frac{1}{2}z^2\frac{dp^{(0)}(r)}{dr} \qquad \text{A 24}$$

where the boundary condition equation A 10 has been used. The boundary condition equation A 11 gives us from equation A 24

$$h(r)\tau(r) + \frac{1}{2}h^2(r)\frac{dp^{(0)}(r)}{dr} = 0 \qquad \text{A 25}$$

where $h(r) = \tilde{h}/\eta$. We use equation A 25 to eliminate $\tau(r)$ in favour of $dp^{(0)}(r)/dr$ and then incompressibility in the form of equation A 19, with results from equation A 25 inserted, to give

$$-z\frac{1}{2}\frac{d}{dr}\left[h(r)\frac{dp^{(0)}(r)}{dr}\right] - \frac{1}{2}zh(r)\frac{dp^{(0)}(r)}{rdr} + \frac{1}{2}z^2\frac{d^2p^{(0)}(r)}{dr^2} + \frac{1}{2}z^2\frac{dp^{(0)}(r)}{rdr} + \frac{\partial u_z^{(0)}}{\partial z} = 0 \qquad \text{A 26}$$

We then integrate this to obtain

$$u_z^{(0)} = \frac{1}{4}z^2\frac{d}{dr}\left[h(r)\frac{dp^{(0)}(r)}{dr}\right] + \frac{1}{4}z^2h(r)\frac{dp^{(0)}(r)}{rdr} - \frac{1}{6}z^3\frac{d^2p^{(0)}(r)}{dr^2} - \frac{1}{6}z^3\frac{dp^{(0)}(r)}{rdr} \qquad \text{A 27}$$

where we have used the boundary condition equation A 10 at $z = 0$. Now use equation A 12 and we deduce that this leads to

$$\frac{d}{dr}\left[rh^3(r)\frac{dp^{(0)}(r)}{dr}\right]=12r \qquad \text{A 28}$$

We integrate this once and obtain

$$\frac{dp^{(0)}(r)}{dr}=\frac{6r^2+c_1}{rh^3(r)} \qquad \text{A 29}$$

where c_1 is a constant. We confine ourselves to cases where $h(0)$ is finite, and conclude that this leads to $c_1=0$, since otherwise the gradient of $p^{(0)}$ diverges. As a consequence, integration of A 29gives us

$$p^{(0)}=6\int_1^r\frac{\xi d\xi}{h^3(\xi)} \qquad \text{A 30}$$

where we have used the 1st of the boundary conditions in equation A 13as it gives $p^{(0)}(1)=0$.

Examples:

(1) Layer of uniform thickness.

In this case $h(r)=1$ and equation A 30 becomes

$$p^{(0)}(r)=3\left(r^2-1\right) \qquad \text{A 31}$$

which, through equation A 21 leads to

$$\sigma_{rz}^{(1)}=3r(2z-1) \qquad \text{A 32}$$

Therefore, we have all the leading order stresses since

$$\sigma_{rr}^{(0)}=\sigma_{\theta\theta}^{(0)}=\sigma_{zz}^{(0)}=-p^{(0)}=3\left(1-r^2\right) \qquad \text{A 33}$$

The tensile stresses are therefore greatest at the centre of the fibril. Note that the shear stress in equation A 32 is not zero at $r = 1$, violating the 2nd boundary in equation A 13. However, the boundary condition is satisfied in an average sense since the integral of equation A 32 with respect to z from zero to 1 is zero. Since the shear stresses are lower order, this discrepancy is not significant. It would have to be fixed by a boundary layer, which the St. Venant principle shows would only affect the solution over a radial distance comparable to the thickness of the layer.

The results in equations A 32 and A 33 are normalized. We obtain the physical results by restoring the factors by which normalization took place. This gives

$$\begin{aligned} \tilde{\sigma}_{rr} &= \tilde{\sigma}_{\theta\theta} = \tilde{\sigma}_{zz} = 3\Sigma\left(1-r^2\right) = \frac{3\Delta\mu D^2}{4h^3}\left(1-\frac{4\tilde{r}^2}{D^2}\right) \\ \tilde{\sigma}_{rz} &= 3\Sigma\delta r\left(2z-1\right) = \frac{3\Delta\mu\tilde{r}}{h^2}\left(\frac{2\tilde{z}}{h}-1\right) \end{aligned} \qquad \text{A 34}$$

where h is the thickness of the compliant layer. It can be seen that the shear stress is much smaller than the direct stresses. The error in all stresses is small compared to the magnitude of the shear stress.

As a result of equation A 34 the highest tensile stress on the interface is $3\Delta\mu D^2/\left(4\eta^3\right) = E\Delta D^2/\left(4\eta^3\right)$, where E is Young's modulus. This is the stress at the centre of the fibril that will cause detachment if failure at the corner singularity is suppressed. Note that the solution in equation A 34 gives no information about the corner singularity as it represents a boundary layer at the edge of the fibril. We note that the maximum tensile stress at the interface is twice as high as the average stress on the interface.

(2) Layer with quadratic shape

This case can represent the rigid segment of the fibril having a circular shape where, following Hertz, we approximate these shapes by recognizing that the layer thickness is smaller than the

diameters of the circle. However, the slope of the curved interface must remain small throughout its extent for the asymptotic analysis to be valid. This rules out the caser of $R = D/2$, though the case of $R = D$ may be admissible (see Figure 4.1).

The shape of the thin layer is

$$h(r) = h_o + (1 - h_o) r^2 \qquad \text{A 35}$$

where $h_o = \eta_o / \eta$ with $\tilde{h}(0) = \eta_o$ and therefore is the narrowest segment of the thin layer.

Integration of equation A 30 then gives us

$$p^{(0)} = \frac{1}{4(1-h_o)} \left\{ 1 - \frac{1}{\left[h_o + (1-h_o) r^2 \right]^2} \right\} \qquad \text{A 36}$$

and then

$$\sigma_{rz}^{(1)} = \frac{3r(2z-1)}{\left[h_o + (1-h_o) r^2 \right]^3} \qquad \text{A 37}$$

These normalized values can be converted to physical values by multiplication by the appropriate factors as was carried out to obtain equation A 34, in this case, the maximum stress, which is at $\tilde{r} = 0$, is $(1 + h_o)/h_o = 1 + \tilde{h}(D/2)/\tilde{h}(0)$ times the average stress on the interface. We note that this result is valid for the flat interface, and predicts that the maximum stress rises above twice the average stress when the interface is curved, consistent with the results in Figure 4.7.

Appendix B: Plane strain and axisymmetric results

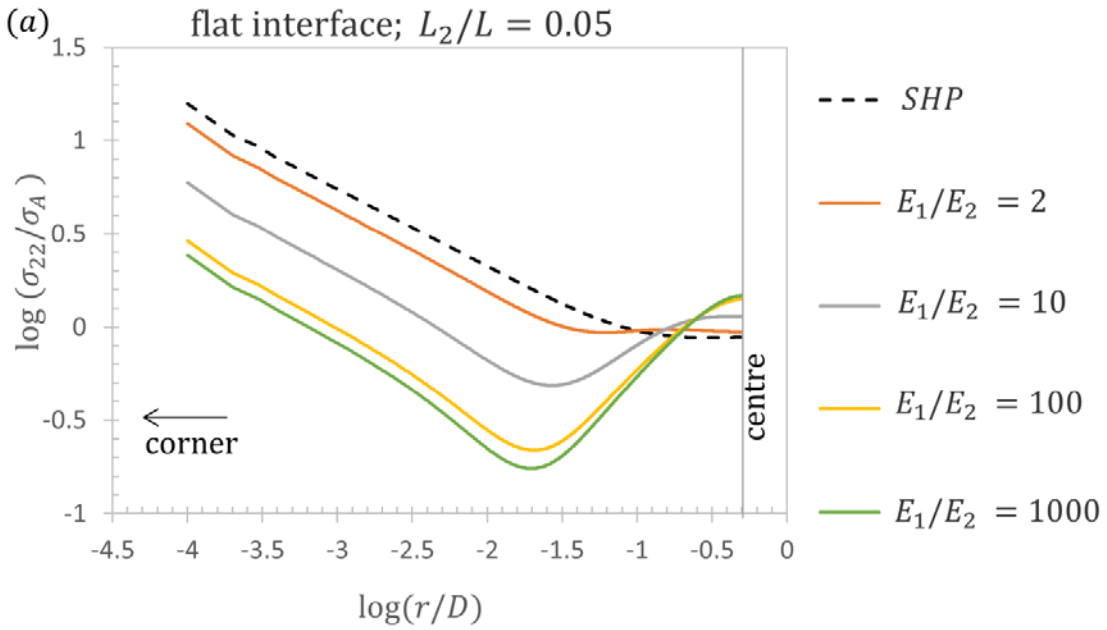

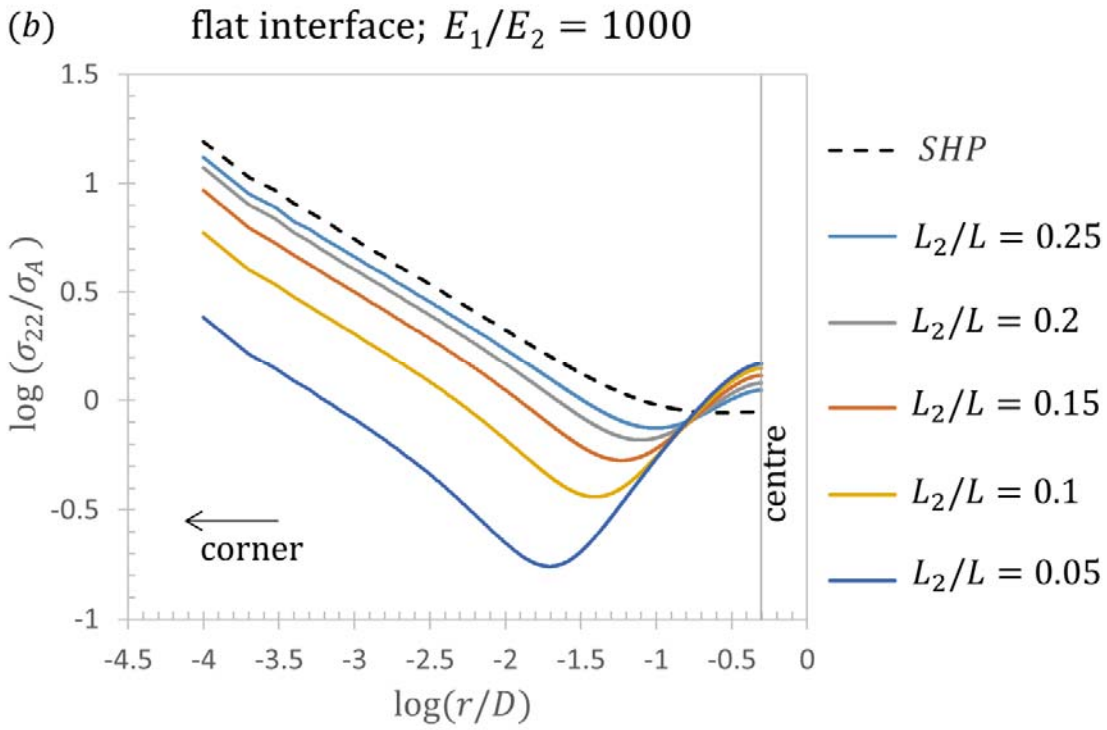

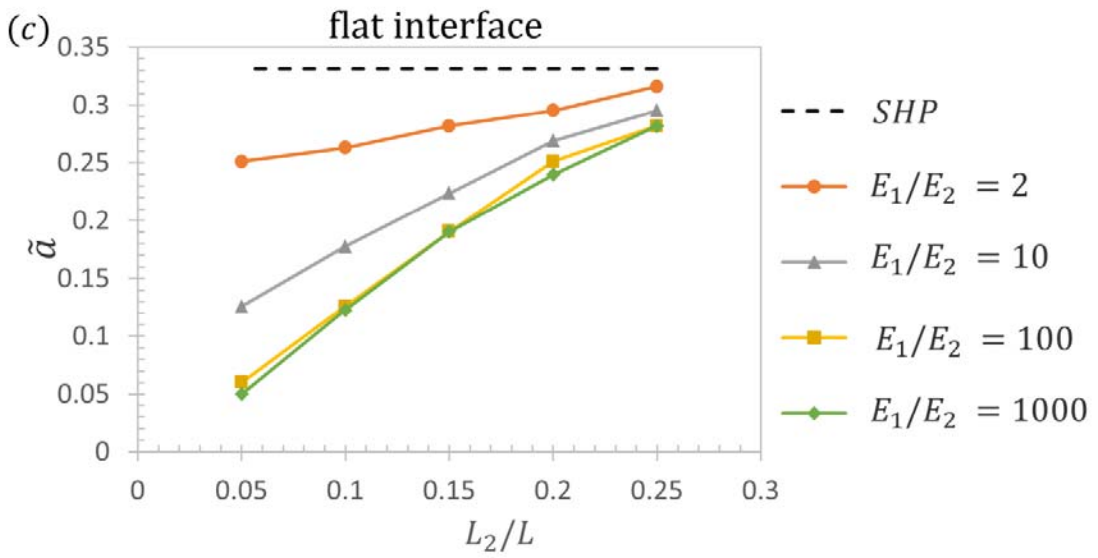

Figure B1: Analysis of a composite fibril with a flat interface for plane strain. Tensile stress σ_{22} along the fibril and substrate interface for different combinations of (a) Young's modulus ratio E_1/E_2 of the top and bottom part of the fibril respectively for a constant $L_2/L = 0.05$, and (b) height of the soft portion L_2 normalised by total height L and constant $E_1/E_2 = 1000$. (c) Calibration coefficient for composite fibrils for different combinations of the ratio of height L_2/L and Young's modulus E_1/E_2. The dashed black lines represent the straight homogeneous punch (SHP) results. The colours and symbol shapes reflect the varying parameters E_1/E_2 and L_2/L.

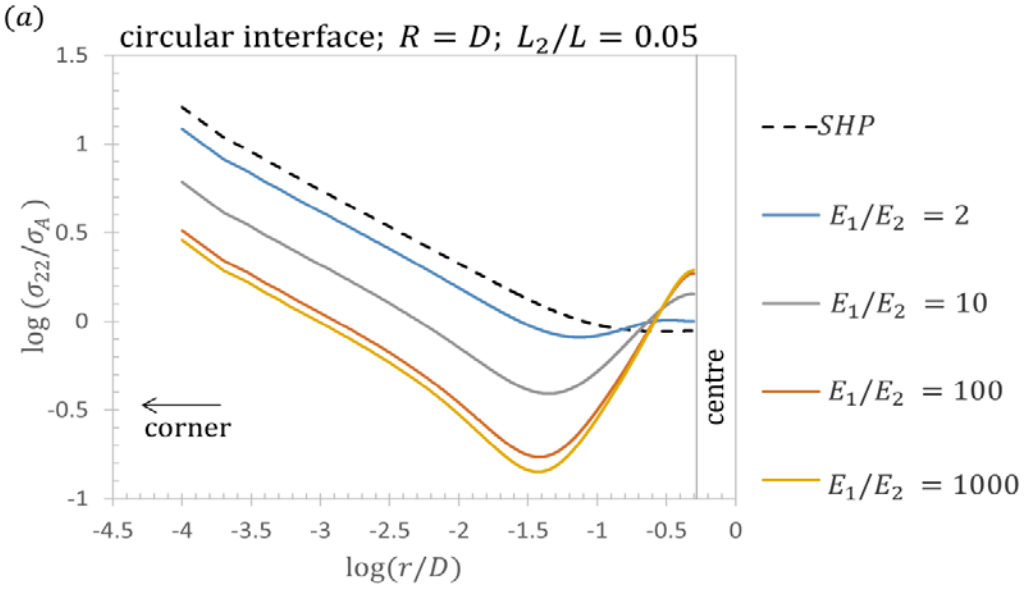
(a)
circular interface; $R = D$; $L_2/L = 0.05$
1.5
1
0.5
0
-0.5
-1
$\log(\sigma_{22}/\sigma_A)$
-4.5
-4
-3.5
-3
-2.5
-2
-1.5
-1
-0.5
0
$\log(r/D)$
corner
centre
SHP
$E_1/E_2 = 2$
$E_1/E_2 = 10$
$E_1/E_2 = 100$
$E_1/E_2 = 1000$

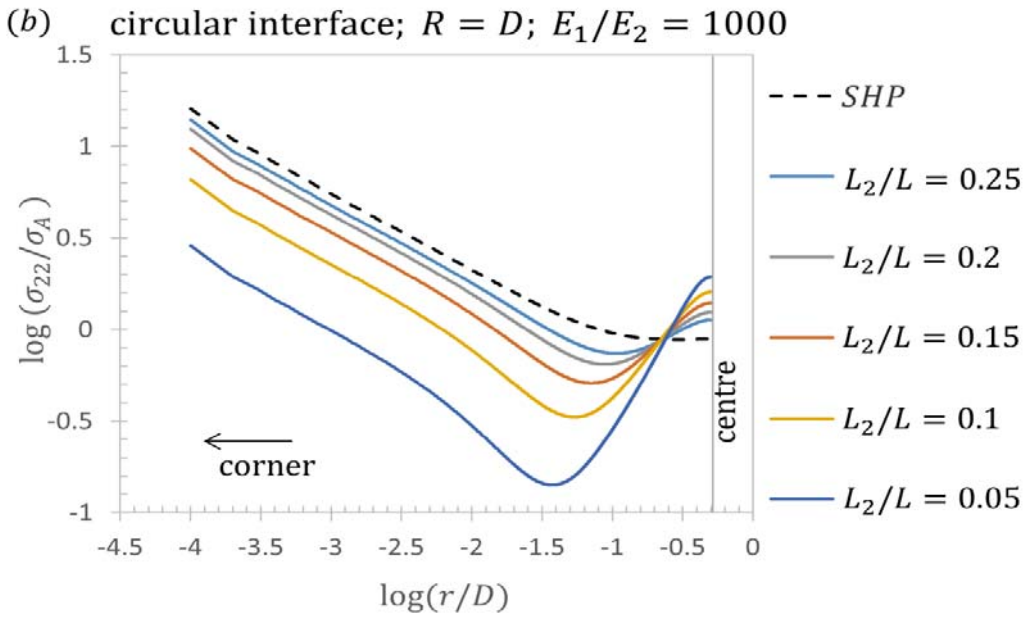
(b)
circular interface; $R = D$; $E_1/E_2 = 1000$
1.5
1
0.5
0
-0.5
-1
$\log(\sigma_{22}/\sigma_A)$
-4.5
-4
-3.5
-3
-2.5
-2
-1.5
-1
-0.5
0
$\log(r/D)$
corner
centre
SHP
$L_2/L = 0.25$
$L_2/L = 0.2$
$L_2/L = 0.15$
$L_2/L = 0.1$
$L_2/L = 0.05$

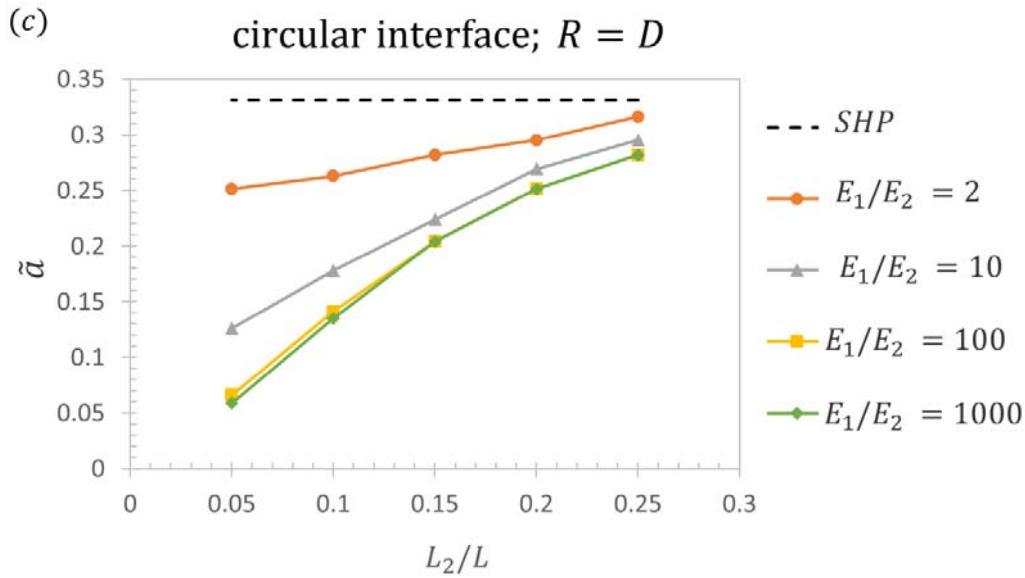

Figure B2: Tensile stress σ_{22} along the fibril and substrate interface for a composite fibril with a circular interface ($R = D$) for different combinations of Young's modulus ratio E_1/E_2 and layer thickness ratio L_2/L and their respective calibration coefficients. The results are reported for the plane strain case. The dashed black lines represent the straight homogeneous punch (SHP) results. The colours and symbol shapes reflect the varying parameters E_1/E_2 and L_2/L.

(a) circular interface; $R = D/2$; $L_2/L = 0.05$

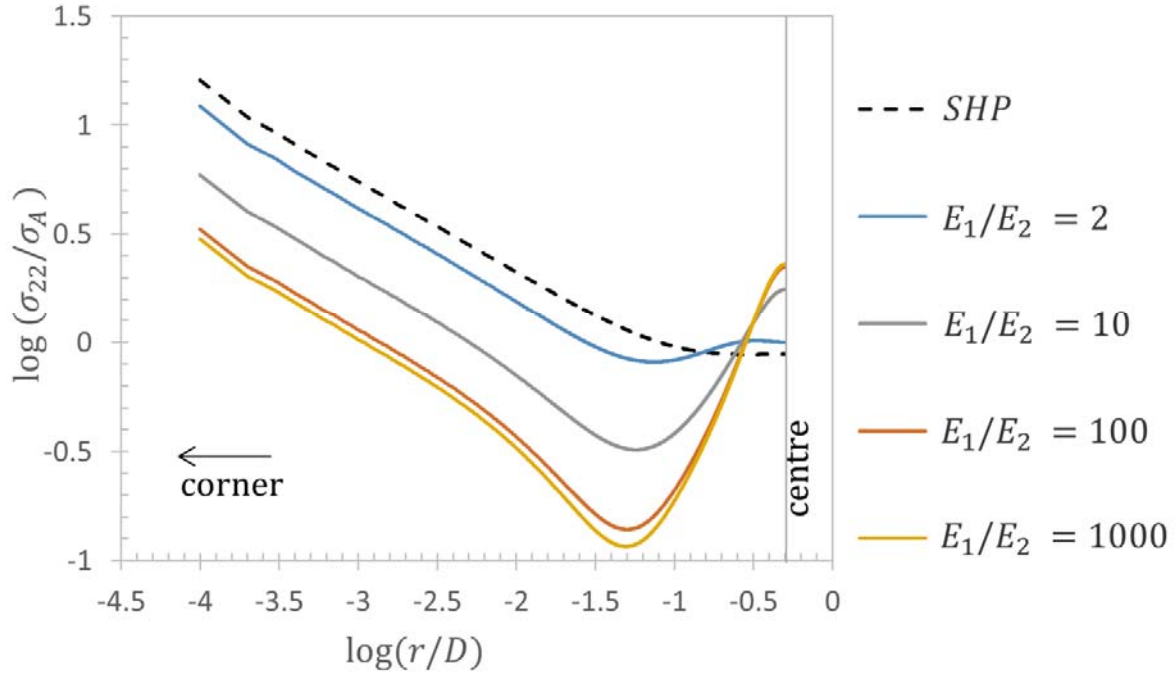

(b) circular interface; $R = D/2$; $E_1/E_2 = 1000$

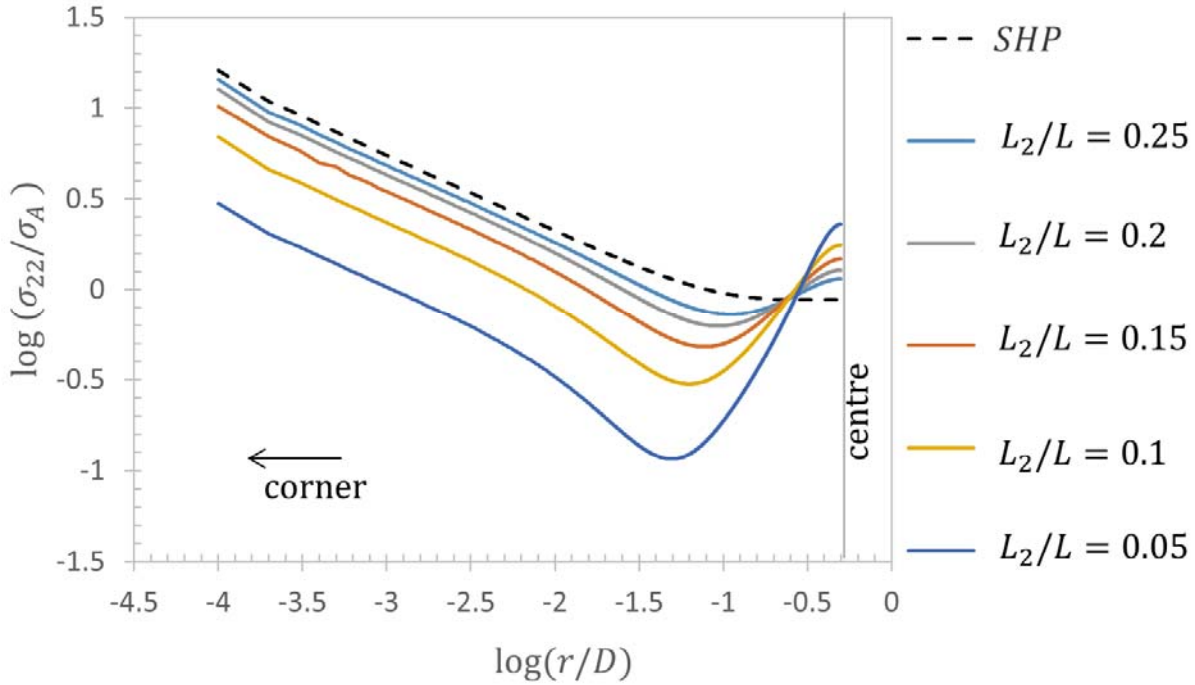

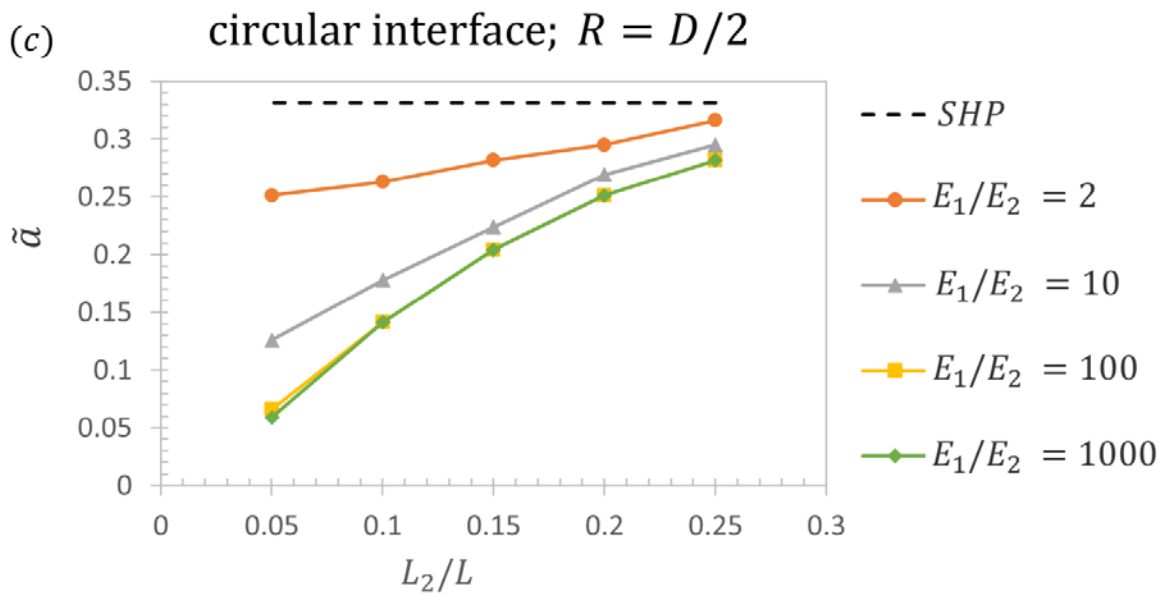

Figure B3: Tensile stress σ_{22} along the fibril and substrate interface for a composite fibril with a circular interface ($R = D/2$) for different combinations of Young's modulus ratio E_1/E_2, layer thickness ratio L_2/L and their corresponding calibration coefficients. The results are reported for the plane strain case. The dashed black lines represent the straight homogeneous punch (SHP) results. The colours and symbol shapes reflect the varying parameters E_1/E_2 and L_2/L.

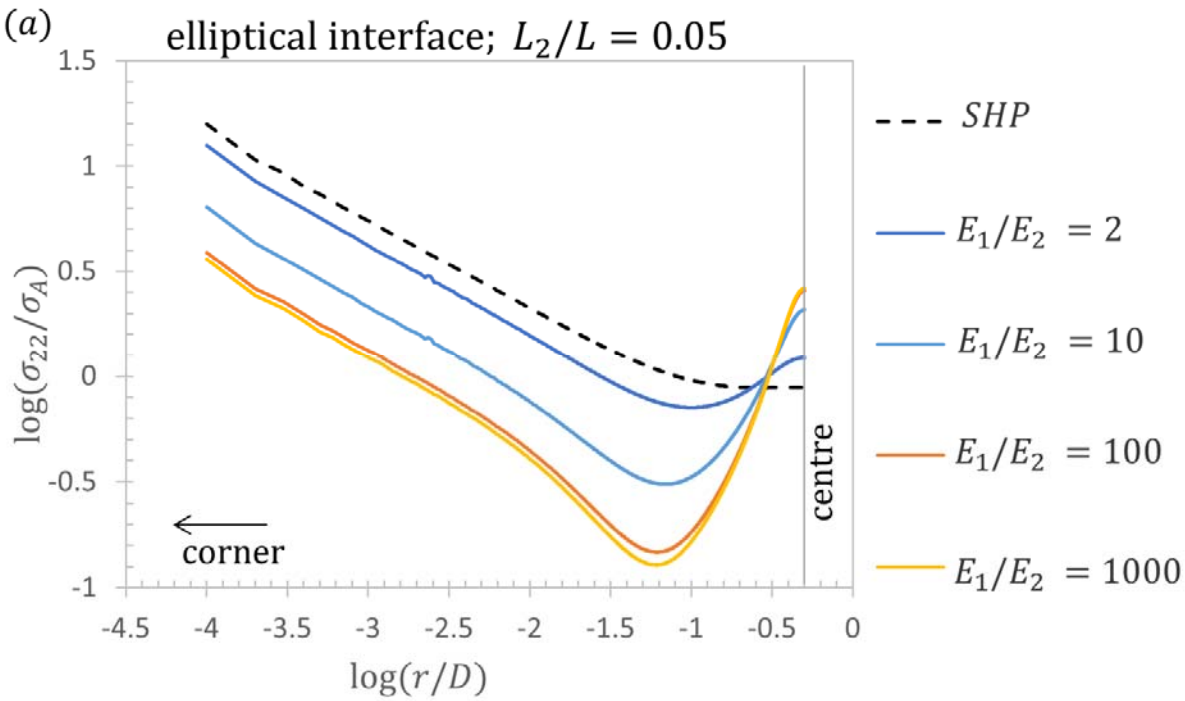
(a)
elliptical interface; $L_2/L = 0.05$
1.5
1
0.5
0
-0.5
-1
$\log(\sigma_{22}/\sigma_A)$
-4.5
-4
-3.5
-3
-2.5
-2
-1.5
-1
-0.5
0
$\log(r/D)$
corner
centre
SHP
$E_1/E_2 = 2$
$E_1/E_2 = 10$
$E_1/E_2 = 100$
$E_1/E_2 = 1000$

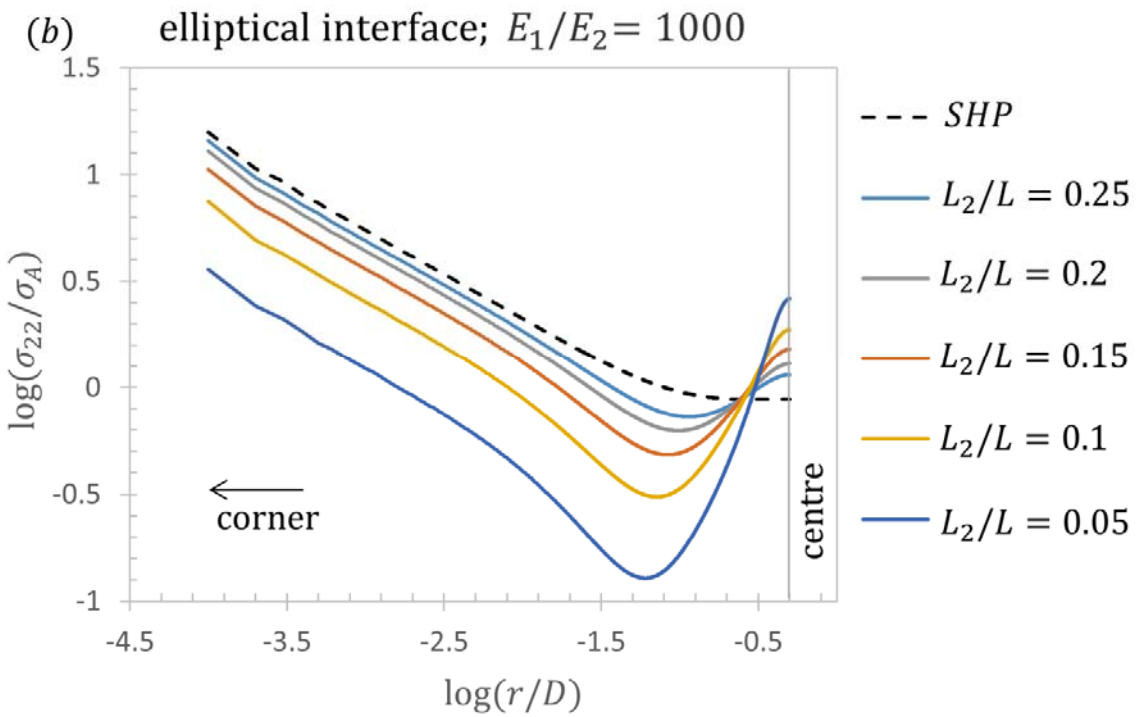
(b)
elliptical interface; $E_1/E_2 = 1000$
1.5
1
0.5
0
-0.5
-1
$\log(\sigma_{22}/\sigma_A)$
-4.5
-3.5
-2.5
-1.5
-0.5
$\log(r/D)$
corner
centre
SHP
$L_2/L = 0.25$
$L_2/L = 0.2$
$L_2/L = 0.15$
$L_2/L = 0.1$
$L_2/L = 0.05$

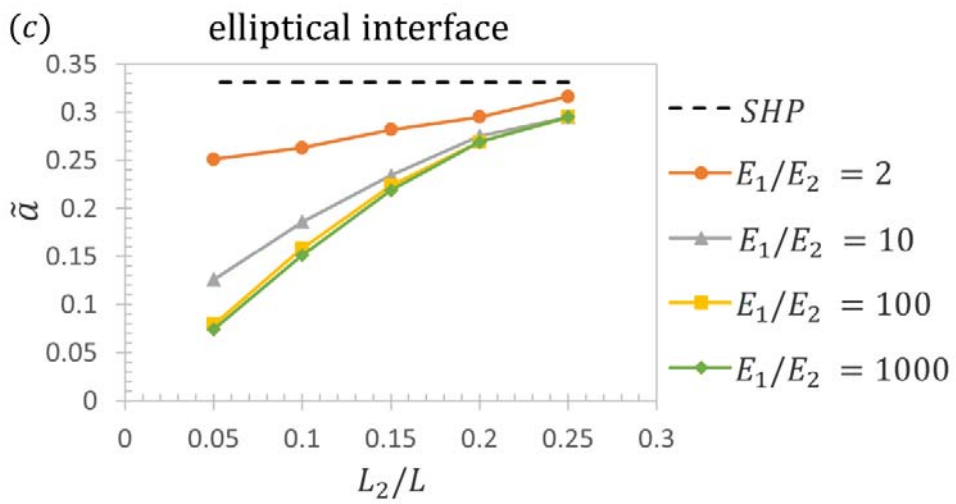

Figure B4: Tensile stress σ_{22} along the fibril and substrate interface for a composite fibril with an elliptical interface where the major axis length is double the diameter D by varying E_1/E_2 (a) and L_2/L. (b) and the corresponding calibration coefficients (c). The dashed black lines represent the straight homogeneous punch (SHP) results. The colours and symbol shapes reflect the varying parameters E_1/E_2 and L_2/L. The results are for plane strain $(2D)$.

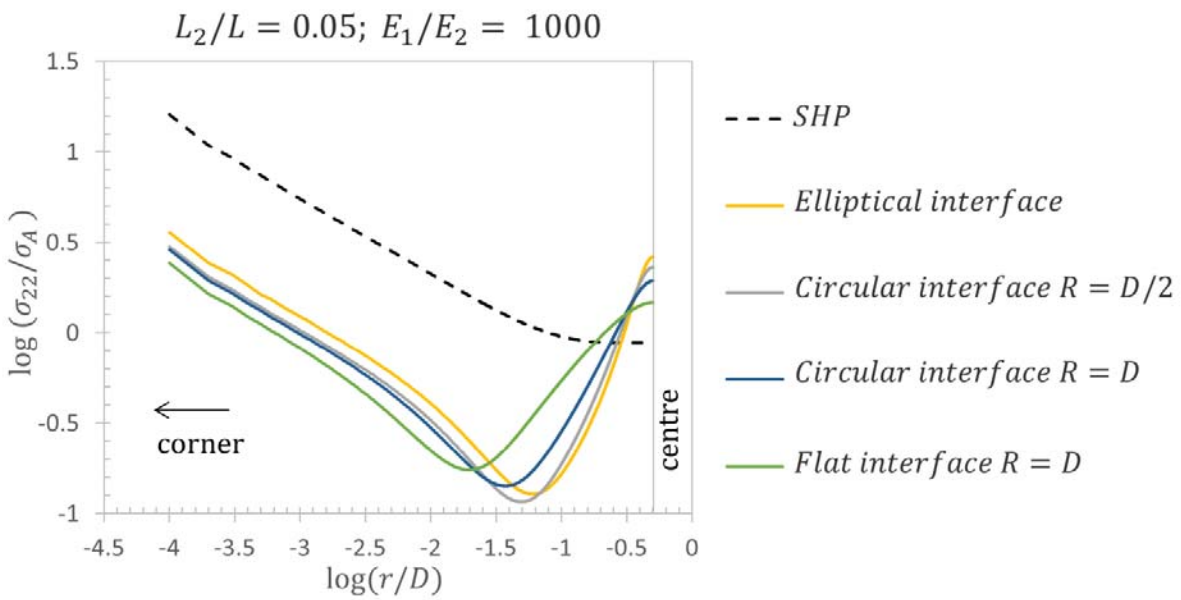

Figure B5: Normal stress σ_{22} along the fibril and substrate interface for fibrils with different interface shapes and with L_2/L ratio 0.05 for the plane strain case. The dashed black lines represent the straight homogeneous punch (SHP) results.

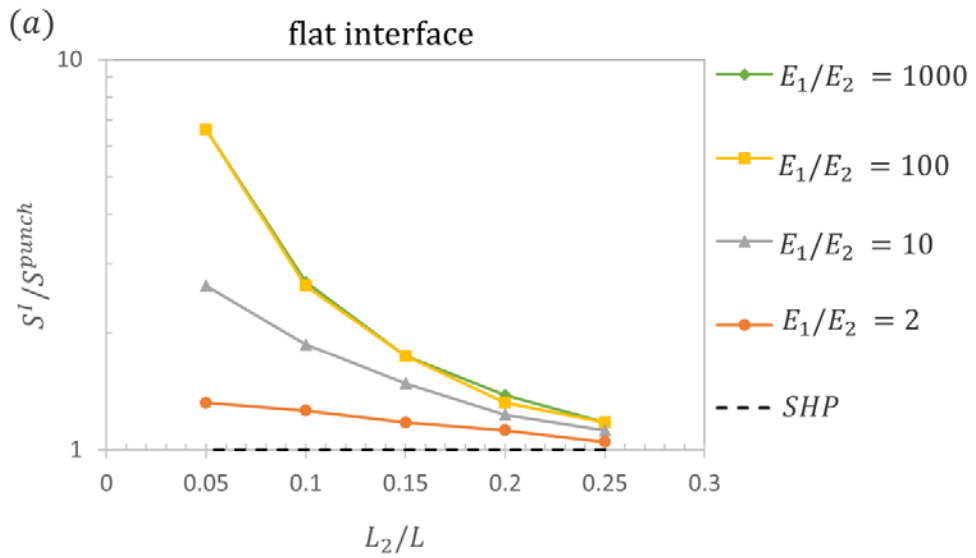
(a)
flat interface
10
1
S^I/S^{punch}
0
0.05
0.1
0.15
0.2
0.25
0.3
L_2/L
$E_1/E_2 = 1000$
$E_1/E_2 = 100$
$E_1/E_2 = 10$
$E_1/E_2 = 2$
SHP

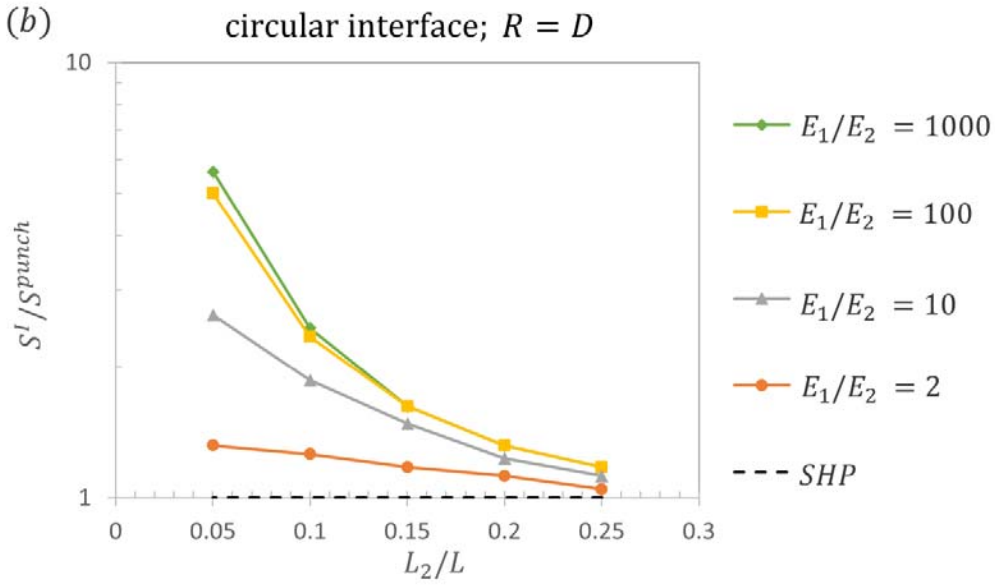
(b)
circular interface; $R = D$
10
1
S^I/S^{punch}
0
0.05
0.1
0.15
0.2
0.25
0.3
L_2/L
$E_1/E_2 = 1000$
$E_1/E_2 = 100$
$E_1/E_2 = 10$
$E_1/E_2 = 2$
SHP

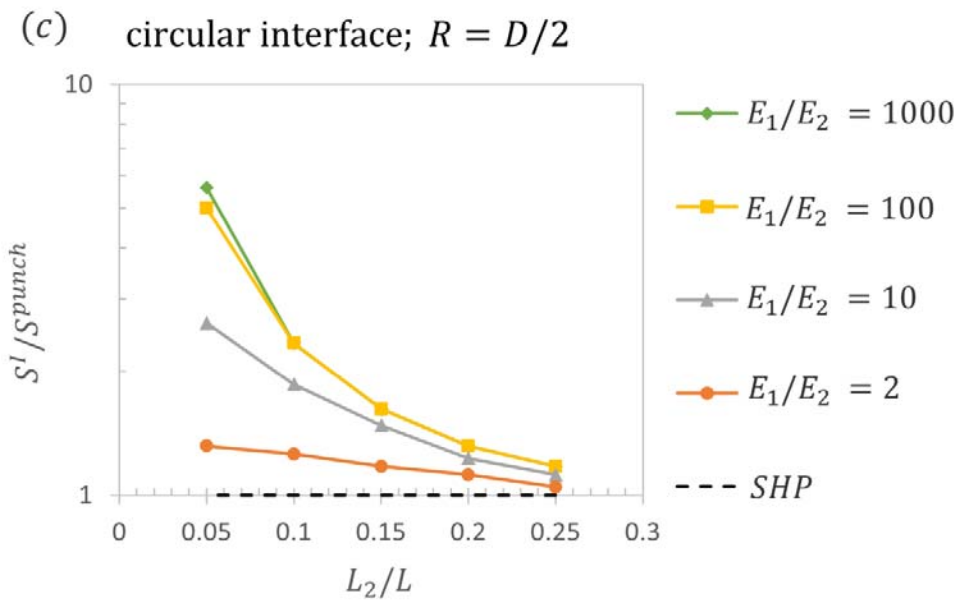

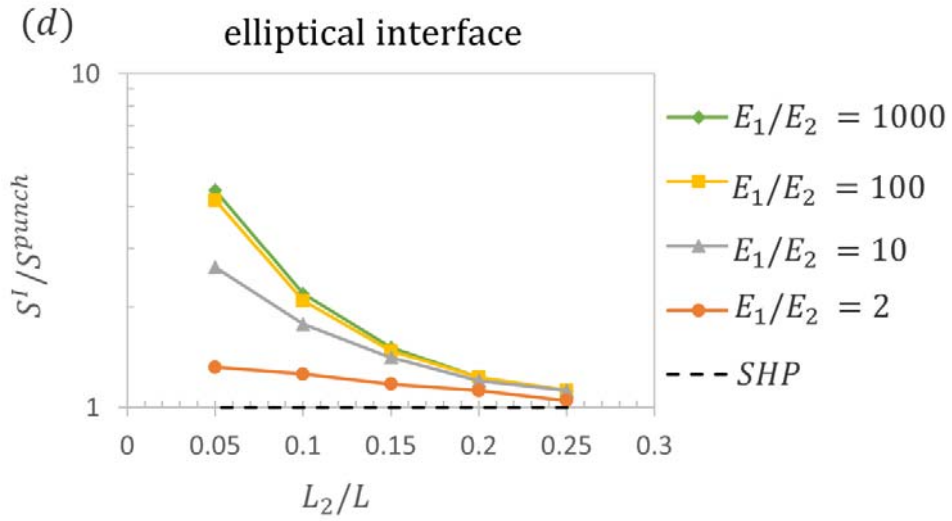

Figure B6: Adhesion strength values for composite fibrils for different interfaces, and different combinations of height ratio L_2/L and Young's modulus E_1/E_2. The results are shown for a composite fibril with (a) flat interface, (b) circular interface where the radius R is equal to the diameter D of the fibril, (c) circular interface where the radius R is equal to half of the diameter and (d) elliptical interface with major axis is double the diameter D. The dashed black lines represent the straight homogeneous punch (SHP) results.

L_2/L	$\tilde{a}$			
	$E_1/E_2 = 2$	$E_1/E_2 = 10$	$E_1/E_2 = 100$	$E_1/E_2 = 1000$
0.25	0.316	0.295	0.282	0.282
0.2	0.295	0.269	0.251	0.240
0.15	0.281	0.224	0.190	0.190
0.1	0.263	0.178	0.126	0.123
0.05	0.251	0.126	0.050	0.050
0.005	0.251	0.1	0.032	0.006

Table B1: Calibration coefficients $\tilde{a}$ for a flat interface for the plane strain case.

(a)

L_2/L	$\tilde{a}$							
	$E_1/E_2 = 2$		$E_1/E_2 = 10$		$E_1/E_2 = 100$		$E_1/E_2 = 1000$	
	$R = D$	$R = D/2$	$R = D$	$R = D/2$	$R = D$	$R = D/2$	$R = D$	$R = D/2$
0.25	0.316	0.316	0.295	0.295	0.282	0.282	0.282	0.282
0.2	0.295	0.295	0.269	0.269	0.251	0.251	0.251	0.251
0.15	0.282	0.282	0.224	0.224	0.204	0.204	0.204	0.204
0.1	0.263	0.263	0.178	0.178	0.141	0.141	0.135	0.141
0.05	0.251	0.251	0.126	0.126	0.066	0.066	0.059	0.059

(b)

L_2/L	$\tilde{a}$									
	$E_1/E_2 = 2$		$E_1/E_2 = 10$		$E_1/E_2 = 100$		$E_1/E_2 = 1000$		$E_1/E_2 = 1000000$	
	$R = D$	$R = D/2$	$R = D$	$R = D/2$	$R = D$	$R = D/2$	$R = D$	$R = D/2$	$R = D$	$R = D/2$
0.25	0.275	0.275	0.269	0.269	0.263	0.263	0.263	0.269	0.263	0.269
0.2	0.263	0.269	0.257	0.263	0.251	0.251	0.251	0.251	0.251	0.251
0.15	0.251	0.263	0.234	0.234	0.224	0.229	0.229	0.229	0.229	0.229
0.1	0.240	0.245	0.191	0.200	0.178	0.182	0.170	0.182	0.170	0.182
0.05	0.224	0.224	0.135	0.141	0.095	0.107	0.089	0.105	0.089	0.105
0.005	0.209	0.209	0.100	0.100	0.032	0.030	0.013	0.013	0.008	0.011

Table B2: Calibration coefficients $\tilde{a}$ for a circular interface $(R = D, R = D/2)$ for the plane strain (a) and the axisymmetric case (b).

(a)

L_2/L	$\tilde{a}$				
	$E_1/E_2 = 2$	$E_1/E_2 = 10$	$E_1/E_2 = 100$	$E_1/E_2 = 1000$	$E_1/E_2 = 1000000$
0.25	0.316	0.295	0.295	0.295	0.295
0.2	0.295	0.275	0.269	0.263	0.269
0.15	0.282	0.234	0.224	0.224	0.219
0.1	0.263	0.186	0.158	0.158	0.151
0.05	0.251	0.126	0.079	0.076	0.074

(b)

L_2/L	$\tilde{a}$				
	$E_1/E_2 = 2$	$E_1/E_2 = 10$	$E_1/E_2 = 100$	$E_1/E_2 = 1000$	$E_1/E_2 = 1000000$
0.25	0.275	0.269	0.269	0.263	0.263
0.2	0.269	0.263	0.263	0.257	0.257
0.15	0.263	0.245	0.240	0.240	0.240
0.1	0.251	0.209	0.200	0.195	0.195
0.05	0.234	0.162	0.132	0.126	0.126
0.005	0.224	0.112	0.040	0.022	0.022

Table B3: Calibration coefficients ã for an elliptical interface (a) plane strain (b) axisymmetric cases.

S_I/S_A	$E_1/E_2 = 2$				$E_1/E_2 = 10$				$E_1/E_2 = 100$				$E_1/E_2 = 1000$			
	FI	*CI*		*EI*	*FI*	*CI*		*EI*	*FI*	*CI*		*EI*	*FI*	*CI*		*EI*
L_2/L		*R=D*	*R=D/2*			*R=D*	*R=D/2*			*R=D*	*R=D/2*			*R=D*	*R=D/2*	
0.25	1.05	1.05	1.05	1.05	1.12	1.12	1.12	1.12	1.17	1.17	1.17	1.12	1.17	1.17	1.17	1.12
0.2	1.12	1.12	1.12	1.12	1.23	1.23	1.23	1.20	1.32	1.32	1.32	1.23	1.32	1.32	1.32	1.23
0.15	1.17	1.17	1.17	1.17	1.48	1.48	1.48	1.41	1.74	1.62	1.62	1.48	1.74	1.62	1.62	1.51
0.1	1.26	1.26	1.26	1.26	1.86	1.86	1.86	1.78	2.63	2.34	2.34	2.09	2.63	2.45	2.34	2.19
0.05	1.32	1.32	1.32	1.32	2.63	2.63	2.63	2.63	6.61	5.01	5.01	4.17	6.61	5.62	5.62	4.47

Table B4: Adhesion strength S^I/S^{punch} *for the flat and circular interfaces* $(R = D, R = D/2)$ *for the plane strain case.*

5 Summary

In the past decade numerous researchers have concentrated on developing reusable, reversible dry adhesives. They were successful in fabricating such structures and the patterned structures performed better than the unpatterned structures. Different shapes of tip endings such as straight punch, spherical, spatular and mushroom fibrils were examined and mushroom fibrils were showing better adhesion compared to other examined surfaces. There were continuous efforts by theoreticians to understand the mechanics of fibrillar adhesion by analytical and numerical studies but still some unanswered questions remain. Two such questions are addressed and discussed in detail in this thesis. First part focusses on examining how the mushroom cap geometry influences the stress distribution along the interface (where fibril comes in contact with probe) and adhesion strength. We have also suggested a way to improve the geometry to distribute the stresses more uniformly, which might help the fibril to increase adhesion. In the second part we have explored whether there is an alternative way to replicate the behaviour of the mushroom fibrils by varying the material modulus. The aim of the thesis was explained in detail in Chapter 2.5.

In Chapter 3 we discussed how the adhesion strength of mushroom fibrils is dependent on the shape of the fibril terminal. The adhesion strength is predicted based on the assumption that the detachment will occur from edge. It is assumed that the interface is perfectly bonded to a rigid substrate and no sliding can occur at the interface between the fibril and the substrate to which it is attached. Straight punch fibrils show lower adhesion strength when compared to mushroom and composite fibrils. Corner stress singularity is one of the main reasons for the early detachment of the straight punch and this behaviour can be observed in the normal stress along the fibril and rigid substrate interface in Figure 3.2. Due to the corner stress singularity, the detachment might be initiated in this area and this area might be prone to detachment under the assumption that there is no other defect along the interface. Experimental results also suggest that straight punch detaches from the edge and abruptly loses contact once the detachment is initiated.

In case of the mushroom fibrils, we have investigated and reported more than 100 different fibril geometry combinations i.e. for D_f/D and h/D_f. It is observed that the mushroom cap geometry

strongly influences the stress distribution along the interface. Even the smallest mushroom cap results in reduction of the amplitude of stress singularity when compared to the stress distribution of a straight punch. Further increase in D_f/D and decrease in h/D_f results in further reduction of amplitude of the stress singularity and at the same time the stress close to centre of the fibril is increased. The increase of stress close to centre might act as a crack initiating point and the edge crack is suppressed and this is only true when stress causes the failure when the fibril is not detached by a different mechanism for example: manufacturing or bonding defects. This claim is also supported by the experiments where the detachment of mushroom fibrils initiated close to the centre and propagated radially towards the edge.

Based on this analysis the optimum geometry of the mushroom fibril needs to have a mushroom cap with minimum thickness and minimum stalk diameter to suppress the edge detachment and initiate the centre detachment. This behaviour is limited by the tendency for detachment to occur near the centre of the fibril and, eventually, by the material strength.

In Figure 3.5 and Figure 3.6 one can observe a stress peak close to centre and we made efforts to improve the design to eliminate these stress peaks. We have introduced a fillet radius to smoothen the transition between fibril stalk and the mushroom cap; we were successful in eliminating the stress peak (which was seen in Figure 3.5 and Figure 3.6) close to centre and results can be seen in Figure 3.15. This inclusion has resulted in reduction of the adhesive strength of fibrils where it is controlled by the edge singularity. However, the adhesive strength associated with the detachment commencing near the centre of the fibril is improved. The scope of the work did not allow us to treat it further but a detailed study is necessary to identify the combination of the mushroom cap and the fillet radius to achieve the adhesive strength close to the cohesive stress at the interface.

As mentioned in Chapter 2.5 one of the other major questions tackled in this thesis was to explore if there was an alternative way to replicate the adhesive strength of mushroom fibrils by changing the material properties to overcome the difficulties and limitations in manufacturing mushroom fibrils. In Chapter 4 we have come up with a novel method of using composite structures as an alternative of mushroom fibrils which was discussed. The composite geometry has two materials where the stalk is stiffer and the tip is softer. The stiffer stalk gives the

structures mechanical stability and hence high aspect ratio fibrils can be manufactured by avoiding the fibril collapse. The softer tips will give high adaptability to the substrate. From the numerical and experimental investigations, it is evident that the concept of composite helps in reducing the amplitude of corner singularity and increases adhesive strength. The influence of two different parameters were studied, they are as follows:

- The effect of Young's modulus ratio (E_1/E_2) of stiff and soft tip.
- The influence of height of soft tip (L_2/L) by keeping the total height constant.
- The influence of different joining interfaces for soft tip and stiff stalk.

It was shown higher Young's modulus ratios (E_1/E_2) and smaller height ratios (L_2/L) lead to lower amplitudes of the corner singularity (Figure 4.7) and higher adhesive strength (Figure 4.8) when the detachment is controlled by the corner singularity. The experimental results show that the detachment mechanism for a thin soft layer results in fingering like cracks which lead to abrupt detachment.

When a curvature was introduced along the joining interface, the amplitude of the corner singularity increased and if the radius was changed from radius $R = D$ to $D/2$, the corner singularity further increased. The experimental results for $R = D/2$ show that the detachment mechanism for a thin soft layer is changed and centre detachment is provoked. There is a change in the crack initiation and the final detachment which might increase the final adhesive strength. Below a certain limit of L_2/L ratios a transition from edge crack to centre crack or finger cracks occurred in the experiments; these mechanisms are not yet part of the calculations.

The results show that the composite structures have the capability to be an alternative to the mushroom cap fibrils with higher adhesive strength. Mushrooms fibrils currently still show better adhesion than the composite fibrils but more detailed experimental investigations of composite fibrils are necessary to find their optimum. It can be concluded that the shape and material properties play an important role in achieving better adhesive strength.

List of figures

Figure 2.1: Penny crack in an infinite plate subjected to remote tensile load (Shi and Polycarpou, 2005). 6

Figure 2.2: Stresses near the tip of a crack in an elastic material (Shi and Polycarpou, 2005) 7

Figure 2.3: Plane strain approximation to simplify the three dimensional body (left) to a two dimensional body (right). 10

Figure 3.1: Schematics of (a) a straight punch shaped fibril without a mushroom cap and (b) a fibril with a mushroom cap, both adhered to a rigid substrate. 16

Figure 3.2: Normalised normal (σ_{22}) and shear (σ_{12}) tractions for the straight punch (corner to centre) for (a) plane strain and (b) axial symmetry. The remote applied stress is denoted by σ_A 19

Figure 3.3: Schematic of a small crack along the interface at the corner of the contact. 20

Figure 3.4: Comparison of the finite element results and the theoretical asymptotic results for the normal and shear tractions on the interface between the substrate and a specific mushroom capped fibril. The results are plotted from near the edge (left) to the fibril centre (right) for (a) plane strain and (b) axial symmetry. 23

Figure 3.5: Tensile stress along the interface between the substrate and a fibril having a mushroom cap for (a) plane strain and (b) axial symmetry for various values of the mushroom cap diameter, D_f, divided by the diameter, D, of the fibril stalk. Results are shown for a mushroom cap that has a thickness, h, equal to 0.008 times its diameter. 25

Figure 3.6: Tensile stress along the interface between the substrate and a fibril having a mushroom cap for axial symmetry for various values of the ratio of the cap thickness to its diameter h/D_f. Results are shown for a fibril having a mushroom cap whose diameter is twice that of its stalk. 26

Figure 3.7: Calibration coefficient, $\tilde{a}$, plotted as a function of the ratio of mushroom cap thickness to diameter, h/D_f, for various ratios of fibril mushroom cap diameter to fibril stalk diameter D_f/D for (a) plane strain and (b) axial symmetry. The dashed horizontal lines indicate the value of the calibration coefficients a_1 for a straight punch. 28

Figure 3.8: Calibration coefficient $\tilde{a}$ plotted as a function of the ratio of mushroom cap thickness to diameter, h/D_f, for 3 values of the ratio of fibril mushroom cap diameter to fibril stalk diameter D_f/D for axial symmetry. The dashed horizontal lines indicate the value of the calibration coefficient a_1 for a straight punch. The plot is extended to $h/D_f = 1$ to show how

the results for the mushroom capped fibril converge to that of the straight punch as the mushroom cap is thickened..... 29

Figure 3.9: Adhesion strength for edge initiated detachment for a fibril having a mushroom cap of thickness h and diameter D_f is shown for (a) plane strain and (b) axial symmetry. The adhesion strength, S^I, of the fibril with the mushroom cap is given in terms of the average stress on the interface and is normalised by the adhesion strength, S^{punch} of a straight punch fibril having the same diameter as the mushroom cap, with Young's modulus, adhesion energy and edge detachment length, l, the same for all fibrils..... 32

Figure 3.10: Adhesion strength, S^S (full lines), for edge initiated detachment fibrils having mushroom caps of thickness h and diameter D_f is plotted for (a) plane strain and (b) axial symmetry. In this case the adhesion strength is given in terms of the average stress applied to the mushroom fibril stalk of diameter D and is normalised by the adhesion strength, S^{punch}, for a straight punch fibril having the same diameter as the mushroom cap, with Young's modulus, adhesion energy and edge detachment length, l, the same for all fibrils. The detachment strength associated with the stress under the stalk reaching a critical value S_C^S is represented by the horizontal dashed lines, marked "Cohesive Strength S_C^S." The dashed line for Cohesive strength S_C^S is exemplary with an arbitrary position. 35

Figure 3.11: The magnitude of the local peak stress σ^{peak} near the centre of the fibril as depicted in the plots of interface stress in Figure 3.5 and Figure 3.6. The peak stress is normalised by the average interface stress σ^I and is therefore given as the stress concentration factor k. The result is shown as a function of h/D_f for various values of D_f/D. Note that a thin mushroom cap and a thin stalk will promote detachment at the centre by raising the local peak stress there. 38

Figure 3.12: Adhesion strength for a fibril having a mushroom cap predicted for detachment due to a defect at the edge of the mushroom cap ($\bar{S}^I$) and for detachment due to a defect at the location of high stress under the edge of the fibril stalk ($\bar{S}^P$). The ratio of fibril mushroom cap diameter to fibril stalk diameter $D_f/D = 1.41$ and the fibril is axisymmetric. The defect sizes are plotted for three different values of $(3.3D_f^{0.406}\ l^{0.094})/\sqrt{1.5\pi a} = 50, 100,$ and 200 where l is the size of the defect at the mushroom cap edge and $2a$ is the size of the defect at the location of the high stress. These curves are marked accordingly as $50, 100$ and 200..... 39

Figure 3.13: Comparison of published fibril shapes and present study: Tensile stress along the interface for a straight punch, a mushroom fibril (as in the current paper) and a wedge shaped mushroom cap (as in (Aksak et al., 2014)), all for the axisymmetric case. Adhesion controlled by edge detachment is superior for the mushroom shaped fibrils compared to that of the wedge shaped ones. 43

Figure 3.14: Schematic of a mushroom fibril with a fillet of radius R where $R/D_f = 0.083$.... 44

Figure 3.15: Tensile stress along the interface between the substrate and an axisymmetric mushroom cap fibril having a value of the radius of the fillet, R, that is effective at eliminating the high stress under the edge of the fibril stalk. Results are shown for a fibril having a mushroom cap whose diameter is 1.41 times that of its stalk and for various values of the ratio of the cap thickness to its diameter h/D_f. The fillet radius is such that $R/Df = 0.083$. 45

Figure 3.16: Calibration coefficients, $\tilde{a}$, for mushroom fibrils without fillet radii and, a_{fillet}, for mushroom fibrils with fillet radii, both plotted as a function of the ratio of mushroom cap thickness to diameter, h/D_f, for a ratio of fibril mushroom cap diameter to fibril stalk diameter $D_f/D = 1.41$ for axisymmetric fibrils. The fillet radius is such that $R/D_f = 0.083$..... 46

Figure 3.17: Adhesion strength for fibrils with and without fillet radii plotted versus h/D_f for a ratio of fibril mushroom cap diameter to fibril stalk diameter $D_f/D = 1.41$ for axisymmetric mushroom fibrils. Detachment in these cases is initiated at the edge of the mushroom cap. The adhesion strength is normalised by that for a punch shaped fibril. The fillet radius is such that $R/D_f = 0.083$. 48

Figure 4.1: Schematic of different composite fibril interfaces, namely a flat interface, two circular interfaces ($R = D$ and $R = D/2$) and an elliptical interface (where major axis is double the diameter) considered in the current work. The parameter R is the radius of curvature of the interface, D is the fibril diameter, L is the total height of the composite fibril, L_1 and L_2 are the thicknesses of the stiff stalk (#1, with modulus E_1) and the soft layer (#2, with modulus E_2) respectively. The composite fibrils adhere to a rigid substrate. For a remote tensile stress σ_A applied on the free end, the normal stress distribution is calculated along the fibril/substrate interface..... 53

Figure 4.2: Two-step manufacturing process of macroscopic composite fibrils. (a) The fibril stalk is manufactured by filling a prepolymer into a mould with a flat or curved bottom; after the backing layer is flattened using a razor blade, the material is crosslinked. Optical micrographs show exemplary stalk structures. (b) A softer layer is added in a second mould (flat interface). The layer thickness is determined by spacers (in black). The prepolymer of the soft material is covered with a Teflon coated glass slide (in grey) to obtain a flat surface after crosslinking. Optical micrographs show cross sections of final structures. For a more detailed description see (Fischer et al. 2016). 56

Figure 4.3: A Analysis of a composite fibril with flat interface (axisymmetric case). (a) Normalized tensile stress $\sigma_{22}/\sigma_{\mathrm{A}}$ along the fibril-substrate interface for different Young's modulus ratios E_1/E_2 at constant $L_2/L = 0.05$. (b) Plots for different combinations of L_2/L at constant $E_1/E_2 = 1000000$. (c) Calibration coefficient for different combinations of L_2/L and E_1/E_2 . The dashed black lines represent the straight homogeneous punch (SHP) results..... 60

Figure 4.4: Tensile stress σ_{22} along the fibril and substrate interface for a composite fibril with a circular interface ($R = D$) for different combinations of Young's modulus ratio E_1/E_2 and layer thickness ratio L_2/L. The results are reported for the axisymmetric case. The dashed black lines represent the straight homogeneous punch (SHP) results. The colours and symbol shapes reflect the varying parameters E_1/E_2 and L_2/L 63

Figure 4.5: Tensile stress σ_{22} along the fibril and substrate interface for a composite fibril with a circular interface ($R = D/2$) for different combinations of Young's modulus ratio E_1/E_2, layer thickness ratio L_2/L and the corresponding calibration coefficients. The results are reported for the axisymmetric case. The dashed black lines represent the straight homogeneous punch (SHP) results. The colours and symbol shapes reflect the varying parameters E_1/E_2 and L_2/L. 65

Figure 4.6: Tensile stress σ_{22} along the fibril and substrate interface for a composite fibril with an elliptical interface where the major axis length is double the diameter D for different combinations of Young's modulus ratio E_1/E_2, layer thickness ratio L_2/L and the corresponding calibration coefficients. The results are reported for the axisymmetric case. The dashed black lines represent the straight homogeneous punch (SHP) results. The colours and symbol shapes reflect the varying parameters E_1/E_2 and L_2/L. 67

Figure 4.7: Normalized stress $\sigma_{22}/\sigma_{\mathrm{A}}$ along the fibril-substrate interface for fibrils with different interface shapes, $E_1/E_2 = 1000$ and L_2/L = 0.25 (a) and 0.05 (b) (axisymmetric case). The dashed black lines represent the straight homogeneous punch (SHP) results. 68

Figure 4.8: Calculated influence of Young's modulus ratio on adhesive strength, normalized to that of a flat punch, with the following interface shapes: (a) flat, (b) circular with radius $R = D$, (c) $R = D/2$ and (d) elliptical. The dashed black lines represent the straight homogeneous punch (SHP) results. The different Young's modulus ratios are $E_1/E_2 = 2$ (orange, circles), 10 (grey, triangles), 100 (gold, squares), 1000 (green, diamonds) and 1000000 (blue, dashes)..... 70

Figure 4.9: Comparison of normalized adhesion strengths from experiments (symbols) and numerical calculations (lines) for composite fibrils with (a) flat interface and (b) circular interface ($R = D/2$) for $E_1/E_2 = 2$ and 350. The lines refer to calculations for a straight homogeneous punch (black, dashed), and a composite fibril with $E_1/E_2 = 2$ (orange, dashes and dots) and 350 (red, solid). Light green circles represent experiments with $E_1/E_2 = 2$ and dark green stars with $E_1/E_2 = 350$. Filled symbols represent pull-off forces, empty symbols crack initiation forces. Arrows indicate the samples for which the two forces differ significantly. Optical micrographs represent the characteristic detachment mechanisms that were observed for (a) flat and (b) circular interfaces depending on the soft layer thickness. The crack fronts are highlighted by red lines..... 75

Figure B1: Analysis of a composite fibril with a flat interface for plane strain. Tensile stress σ_{22} along the fibril and substrate interface for different combinations of (a) Young's modulus ratio E_1/E_2 of the top and bottom part of the fibril respectively for a constant $L_2/L = 0.05$, and (b) height of the soft portion L_2 normalised by total height L and constant $E_1/E_2 = 1000$. (c) Calibration coefficient for composite fibrils for different combinations of the ratio of height L_2/L and Young's modulus E_1/E_2. The dashed black lines represent the straight homogeneous punch (SHP) results. The colours and symbol shapes reflect the varying parameters E_1/E_2 and L_2/L. 87

Figure B2: Tensile stress σ_{22}along the fibril and substrate interface for a composite fibril with a circular interface ($R = D$) for different combinations of Young's modulus ratio E_1/E_2 and layer thickness ratio L_2/L and their respective calibration coefficients. The results are reported for the plane strain case. The dashed black lines represent the straight homogeneous punch (SHP) results. The colours and symbol shapes reflect the varying parameters E_1/E_2 and L_2/L. 89

Figure B3: Tensile stress σ_{22} along the fibril and substrate interface for a composite fibril with a circular interface ($R = D/2$) for different combinations of Young's modulus ratio E_1/E_2, layer thickness ratio L_2/L and their corresponding calibration coefficients. The results are reported for the plane strain case. The dashed black lines represent the straight homogeneous punch (SHP) results. The colours and symbol shapes reflect the varying parameters E_1/E_2 and L_2/L. 91

Figure B4: Tensile stress σ_{22} along the fibril and substrate interface for a composite fibril with an elliptical interface where the major axis length is double the diameter D by varying E_1/E_2 (a) and L_2/L. (b) and the corresponding calibration coefficients (c). The dashed black lines represent the straight homogeneous punch (SHP) results. The colours and symbol shapes reflect the varying parameters E_1/E_2 and L_2/L. The results are for plane strain ($2D$)..... 93

Figure B5: Normal stress σ_{22} along the fibril and substrate interface for fibrils with different interface shapes and with L_2/L ratio 0.05 for the plane strain case. The dashed black lines represent the straight homogeneous punch (SHP) results..... 94

Figure B6: Adhesion strength values for composite fibrils for different interfaces, and different combinations of height ratio L_2/L and Young's modulus E_1/E_2. The results are shown for a composite fibril with (a) flat interface, (b) circular interface where the radius R is equal to the diameter D of the fibril, (c) circular interface where the radius R is equal to half of the diameter and (d) elliptical interface with major axis is double the diameter D. The dashed black lines represent the straight homogeneous punch (SHP) results..... 96

List of tables

Table 3.1: Calibration coefficients a for plane strain fibrils having a mushroom cap of width D_f and thickness h. The width of the fibril stalk is D. 30

Table 3.2: Calibration coefficients $\tilde{a}$ for axially symmetric fibrils having a mushroom cap of diameter D_f, and thickness h where D is the diameter of the fibril stalk..... 30

Table 3.3: Calibration coefficients $\tilde{a}$ and normalised adhesion strength for axisymmetric fibrils with wedge shaped mushrooms as assumed by Aksak et al. (2014) ($S^I/S^{punch}\ Wedge$). For comparison, we list the adhesion strength of mushroom cap fibrils (S^I/S^{punch}) used in the current paper. The range of S^I/S^{punch} values refers to the mushroom fibrils with different h/D_f. 43

Table 3.4: Calibration coefficients $\tilde{a}$ for axisymmetric fibrils having a fillet radius that is effective at eliminating the high stress under the fibril stalk for mushroom caps with $D_f/D = 1.41$ where D_f and D are the diameter of mushroom cap and the stalk respectively and h is the thickness of the mushroom cap. The fillet radius $R/D_f = 0.083$..... 47

Table 4.1: Calibration coefficients $\tilde{a}$ for flat interface for the axisymmetric case. 61

Table 4.2: Adhesion strength values for different interfaces which include flat (FI), circular (CI) for two different radius $R = D$ and $D/2$ and elliptical (EI) represented as adhesion of composite fibrils normalised by that of a straight homogeneous punch. 71

Table B1: Calibration coefficients $\tilde{a}$ for a flat interface for the plane strain case. 97

Table B2: Calibration coefficients $\tilde{a}$ for a circular interface ($R = D, R = D/2$) for the plane strain (a) and the axisymmetric case (b). 98

Table B3: Calibration coefficients $\tilde{a}$ for an elliptical interface (a) plane strain (b) axisymmetric cases. 99

Table B4: Adhesion strength S^I/S^{punch} for the flat and circular interfaces ($R = D, R = D/2$) for the plane strain case. 100

References

Abaqus6.11, 2011. Documentation. Dassault Systems, Simulia Corporation, Providence, Rhode Island, USA.

Akisanya, A.R., Fleck, N.A., 1997. Interfacial cracking from the freeedge of a long bi-material strip. International Journal of Solids and Structures 34, 1645-1665.

Aksak, B., Hui, C.Y., Sitti, M., 2011. The effect of aspect ratio on adhesion and stiffness for soft elastic fibres. Journal of The Royal Society Interface 8, 1166-1175.

Aksak, B., Sahin, K., Sitti, M., 2014. The optimal shape of elastomer mushroom-like fibers for high and robust adhesion. Beilstein Journal of Nanotechnology 5, 630-638.

Alex, A.V., Kenneth, J.M., Tyler, M., Shashank, P., 2013. Biomimetic autonomous robot inspired by the Cyanea capillata (Cyro). Bioinspiration & biomimetics 8, 046005.

Arzt, E., Enders, S., Gorb, S., 2002. Towards a micromechanical understanding of biological surface devices. Zeitschrift Fur Metallkunde 93, 345-351.

Arzt, E., Gorb, S., Spolenak, R., 2003. From micro to nano contacts in biological attachment devices. Proceedings of the National Academy of Sciences 100, 10603-10606.

Autumn, K., Dittmore, A., Santos, D., Spenko, M., Cutkosky, M., 2006a. Frictional adhesion: a new angle on gecko attachment. Journal of Experimental Biology 209, 3569-3579.

Autumn, K., Liang, Y.A., Hsieh, S.T., Zesch, W., Chan, W.P., Kenny, T.W., Fearing, R., Full, R.J., 2000. Adhesive force of a single gecko foot-hair. Nature 405, 681-685.

Autumn, K., Majidi, C., Groff, R.E., Dittmore, A., Fearing, R., 2006b. Effective elastic modulus of isolated gecko setal arrays. Journal of Experimental Biology 209, 3558-3568.

Autumn, K., Peattie, A.M., 2002. Mechanisms of Adhesion in Geckos. Integrative and Comparative Biology 42, 1081-1090.

Autumn, K., Sitti, M., Liang, Y.A., Peattie, A.M., Hansen, W.R., Sponberg, S., Kenny, T.W., Fearing, R., Israelachvili, J.N., Full, R.J., 2002. Evidence for van der Waals adhesion in gecko setae. Proceedings of the National Academy of Sciences 99, 12252-12256.

Bae, W.-G., Kwak, M.K., Jeong, H.E., Pang, C., Jeong, H., Suh, K.-Y., 2013a. Fabrication and analysis of enforced dry adhesives with core-shell micropillars. Soft Matter 9, 1422-1427.

Bae, W.G., Kim, D., Kwak, M.K., Ha, L., Kang, S.M., Suh, K.Y., 2013b. Enhanced Skin Adhesive Patch with Modulus-Tunable Composite Micropillars. Advanced Healthcare Materials 2, 109-113.

Balijepalli, R.G., Begley, M.R., Fleck, N.A., McMeeking, R.M., Arzt, E., 2016. Numerical simulation of the edge stress singularity and the adhesion strength for compliant mushroom fibrils adhered to rigid substrates. International Journal of Solids and Structures 85–86, 160-171.

Bathe, K.J., 1996. Finite element procedures. Prentice Hall.

Boesel, L.F., Greiner, C., Arzt, E., del Campo, A., 2010. Gecko-Inspired Surfaces: A Path to Strong and Reversible Dry Adhesives. Advanced Materials 22, 2125-2137.

Canas, N., Kamperman, M., Volker, B., Kroner, E., McMeeking, R.M., Arzt, E., 2012. Effect of nano- and micro-roughness on adhesion of bioinspired micropatterned surfaces. Acta biomaterialia 8, 282-288.

Carbone, G., Pierro, E., 2012. Sticky bio-inspired micropillars: finding the best shape. Small (Weinheim an der Bergstrasse, Germany) 8, 1449-1454.

Chandrupatla, T.R., Belegundu, A.D., 2011. Introduction to Finite Elements in Engineering. Pearson Education.

del Campo, A., Arzt, E., 2007. Design parameters and current fabrication approaches for developing bioinspired dry adhesives. Macromolecular Bioscience 7, 118-127.

del Campo, A., Arzt, E., 2011. Generating Micro- and Nanopatterns on Polymeric Materials. Wiley.

del Campo, A., Greiner, C., Arzt, E., 2007. Contact shape controls adhesion of bioinspired fibrillar surfaces. Langmuir 23, 10235-10243.

Derks, D., Lindner, A., Creton, C., Bonn, D., 2003. Cohesive failure of thin layers of soft model adhesives under tension. Journal of Applied Physics 93, 1557-1566.

Fischer, S.C.L., Hensel, R., Arzt, E., 2016a. manuscript in preparation.

Fischer, S.C.L., Levy, O., Kroner, E., Hensel, R., Karp, J.M., Arzt, E., 2016b. Bioinspired Polydimethylsiloxane-Based Composites with High Shear Resistance against Wet Tissue. Journal of the Mechanical Behavior of Biomedical Materials.

Gao, H., Wang, X., Yao, H., Gorb, S., Arzt, E., 2005. Mechanics of hierarchical adhesion structures of geckos. Mechanics of Materials 37, 275-285.

Glassmaker, N.J., Jagota, A., Hui, C.-Y., Kim, J., 2004. Design of biomimetic fibrillar interfaces: 1. Making contact. Journal of The Royal Society Interface 1, 23-33.

Glassmaker, N.J., Jagota, A., Hui, C.Y., 2005. Adhesion enhancement in a biomimetic fibrillar interface. Acta biomaterialia 1, 367-375.

Gorb, S., 2007. Attachment Devices of Insect Cuticle. Springer Netherlands.

Gorb, S., Varenberg, M., Peressadko, A., Tuma, J., 2007a. Biomimetic mushroom-shaped fibrillar adhesive microstructure. Journal of The Royal Society Interface 4, 271-275.

Gorb, S., Varenberg, M., Peressadko, A., Tuma, J., 2007b. Biomimetic mushroom-shaped fibrillar adhesive microstructure. Journal of the Royal Society Interface 4, 271-275.

Gorb, S.N., 2008. Biological attachment devices: exploring nature's diversity for biomimetics. Philosophical Transactions of the Royal Society a-Mathematical Physical and Engineering Sciences 366, 1557-1574.

Gorb, S.N., Filippov, A.E., 2014. Fibrillar adhesion with no clusterisation: Functional significance of material gradient along adhesive setae of insects. Beilstein Journal of Nanotechnology 5, 837-845.

Greiner, C., 2008. Size and shape effects in bioinspired fibrillar adhesives. Universitätsbibliothek der Universität Stuttgart, Stuttgart.

Greiner, C., Buhl, S., del Campo, A., Arzt, E., 2009. Experimental Parameters Controlling Adhesion of Biomimetic Fibrillar Surfaces. The Journal of Adhesion 85, 646-661.

Greiner, C., del Campo, A., Arzt, E., 2007. Adhesion of Bioinspired Micropatterned Surfaces: Effects of Pillar Radius, Aspect Ratio, and Preload. Langmuir 23, 3495-3502.

Griffith, A.A., 1921. The Phenomena of Rupture and Flow in Solids. Philosophical Transactions of the Royal Society of London. Series A, Containing Papers of a Mathematical or Physical Character 221, 163-198.

Guo, Z.-G., Liu, W.-M., Su, B.-L., 2008. A stable lotus-leaf-like water-repellent copper. Applied Physics Letters 92, 063104-063103.

Guo, Z., Zhou, F., Hao, J., Liu, W., 2005. Stable Biomimetic Super-Hydrophobic Engineering Materials. Journal of the American Chemical Society 127, 15670-15671.

Hiller, U., 1968. Untersuchungen zum Feinbau und zur Funktion der Haftborsten von Reptilien. Z. Morph. Tiere 62, 307-362.

Hossfeld, C.K., Schneider, A.S., Arzt, E., Frick, C.P., 2013. Detachment Behavior of Mushroom-Shaped Fibrillar Adhesive Surfaces in Peel Testing. Langmuir 29, 15394-15404.

Huber, G., Gorb, S.N., Hosoda, N., Spolenak, R., Arzt, E., 2007. Influence of surface roughness on gecko adhesion. Acta biomaterialia 3, 607-610.

Huber, G., Gorb, S.N., Spolenak, R., Arzt, E., 2005a. Resolving the nanoscale adhesion of individual gecko spatulae by atomic force microscopy. Biology Letters 1, 2-4.

Huber, G., Mantz, H., Spolenak, R., Mecke, K., Jacobs, K., Gorb, S.N., Arzt, E., 2005b. Evidence for capillarity contributions to gecko adhesion from single spatula nanomechanical measurements. Proceedings of the National Academy of Sciences of the United States of America, U S A 102, 16293-16296.

Huber, G., Orso, S., Spolenak, R., Wegst, U.G.K., Enders, S., Gorb, S.N., Arzt, E., 2008. Mechanical properties of a single gecko seta. International Journal of Materials Research 99, 1113-1118.

Hui, C.-Y., Glassmaker, N.J., Tang, T., Jagota, A., 2004. Design of biomimetic fibrillar interfaces: 2. Mechanics of enhanced adhesion. Journal of The Royal Society Interface 1, 35-48.

Irwin, G.R., Naval Research Lab, W.D., 1956. Onset of Fast Crack Propagation in High Strength Steel and Aluminum Alloys. Naval Research Laboratory.

Jagota, A., Bennison, S.J., 2002. Mechanics of Adhesion Through a Fibrillar Microstructure. Integrative and Comparative Biology 42, 1140-1145.

Jagota, A., Bennison, S.J., Smith, C.A., 2000. Analysis of a compressive shear test for adhesion between elastomeric polymers and rigid substrates. International Journal of Fracture 104, 105-130.

Jagota, A., Hui, C.-Y., 2011. Adhesion, friction, and compliance of bio-mimetic and bio-inspired structured interfaces. Materials Science and Engineering: R: Reports 72, 253-292.

Jin, K., Tian, Y., Erickson, J.S., Puthoff, J., Autumn, K., Pesika, N.S., 2012. Design and Fabrication of Gecko-Inspired Adhesives. Langmuir 28, 5737-5742.

Kamperman, M., Kroner, E., del Campo, A., McMeeking, R.M., Arzt, E., 2010. Functional Adhesive Surfaces with "Gecko" Effect: The Concept of Contact Splitting. Advanced Engineering Materials 12, 335-348.

Khaderi, S.N., Fleck, N.A., Arzt, E., McMeeking, R.M., 2015. Detachment of an adhered micropillar from a dissimilar substrate. Journal of the Mechanics and Physics of Solids 75, 159-183.

Kim, S., Sitti, M., 2006. Biologically inspired polymer microfibers with spatulate tips as repeatable fibrillar adhesives. Applied Physics Letters 89, 261911-261913.

Kim, S., Sitti, M., Hui, C.-Y., Long, R., Jagota, A., 2007. Effect of backing layer thickness on adhesion of single-level elastomer fiber arrays. Applied Physics Letters 91, -.

Kroner, E., Blau, J., Arzt, E., 2012a. Note: An adhesion measurement setup for bioinspired fibrillar surfaces using flat probes. Review of Scientific Instruments 83.

Kroner, E., Kaiser, J.S., Fischer, S.C.L., Arzt, E., 2012b. Bioinspired polymeric surface patterns for medical applications. J Appl Biomater Funct Mater 10, 287-292.

Kwak, M.K., Jeong, H.-E., Suh, K.Y., 2011. Rational Design and Enhanced Biocompatibility of a Dry Adhesive Medical Skin Patch. Advanced Materials 23, 3949-3953.

Lafuma, A., Quere, D., 2003. Superhydrophobic states. Nature Materials 2, 457-460.

Liu, J., Hui, C.Y., Jagota, A., Shen, L., 2009. A model for static friction in a film-terminated microfibril array. Journal of Applied Physics 106, 053520.

Long, R., Hui, C.-Y., Kim, S., Sitti, M., 2008. Modeling the soft backing layer thickness effect on adhesion of elastic microfiber arrays. Journal of Applied Physics 104, 044301-044309.

Mengüç, Y., Yang, S.Y., Kim, S., Rogers, J.A., Sitti, M., 2012. Gecko-Inspired Controllable Adhesive Structures Applied to Micromanipulation. Advanced Functional Materials 22, 1246-1254.

Menon, C., Murphy, M., Sitti, M., 2004. Gecko Inspired Surface Climbing Robots, Robotics and Biomimetics, 2004. ROBIO 2004. IEEE International Conference on, pp. 431-436.

Micciché, M., Arzt, E., Kroner, E., 2014. Single Macroscopic Pillars as Model System for Bioinspired Adhesives: Influence of Tip Dimension, Aspect Ratio, and Tilt Angle. ACS applied materials & interfaces 6, 7076-7083.

Minsky, H.K., Turner, K.T., 2015. Achieving enhanced and tunable adhesion via composite posts. Applied Physics Letters 106, 201604.

Murphy, M.P., Aksak, B., Sitti, M., 2009. Gecko-Inspired Directional and Controllable Adhesion. Small (Weinheim an der Bergstrasse, Germany) 5, 170-175.

Nase, J., Derks, D., Lindner, A., 2011. Dynamic evolution of fingering patterns in a lifted Hele–Shaw cell. Physics of Fluids 23, 123101.

Nase, J., Lindner, A., Creton, C., 2008. Pattern Formation during Deformation of a Confined Viscoelastic Layer: From a Viscous Liquid to a Soft Elastic Solid. Physical Review Letters 101, 074503.

Neinhuis, C., W., B., 1997. Characterization and Distribution of Water-repellent, Self-cleaning Plant Surfaces. Annals of Botany 79, 667-677.

Noone, C.J., Torrilhon, M., Mitsos, A., 2012. Heliostat field optimization: A new computationally efficient model and biomimetic layout. Solar Energy 86, 792-803.

Orso, S., Wegst, U.G.K., Eberl, C., Arzt, E., 2006. Micrometer-scale tensile testing of biological attachment devices. Advanced Materials 18, 874-+.

Paretkar, D., Kamperman, M., Martina, D., Zhao, J., Creton, C., Lindner, A., Jagota, A., McMeeking, R., Arzt, E., 2013. Preload-responsive adhesion: effects of aspect ratio, tip shape and alignment. Journal of the Royal Society Interface 10.

Paretkar, D., Kamperman, M., Schneider, A.S., Martina, D., Creton, C., Arzt, E., 2011. Bioinspired pressure actuated adhesive system. Materials Science and Engineering: C 31, 1152-1159.

Peisker, H., Michels, J., Gorb, S.N., 2013. Evidence for a material gradient in the adhesive tarsal setae of the ladybird beetle Coccinella septempunctata. Nat Commun 4, 1661.

Persson, B.N.J., Gorb, S., 2003. The effect of surface roughness on the adhesion of elastic plates with application to biological systems. Journal of Chemical Physics 119, 11437-11444.

Persson, B.N.J., Tosatti, E., 2001. The effect of surface roughness on the adhesion of elastic solids. Journal of Chemical Physics 115, 5597-5610.

Purtov, J., Frensemeier, M., Kroner, E., 2015. Switchable Adhesion in Vacuum Using Bio-Inspired Dry Adhesives. ACS applied materials & interfaces 7, 24127-24135.

Quek, S.S., Liu, G.R., 2003. Finite Element Method: A Practical Course: A Practical Course. Elsevier Science.

Reddy, J., 2005. An Introduction to the Finite Element Method. McGraw-Hill Education.

Sathya, C., John, T., Kimberly, T., 2013. A microfabricated gecko-inspired controllable and reusable dry adhesive. Smart Materials and Structures 22, 025013.

Scholz, I., Baumgartner, W., Federle, W., 2008. Micromechanics of smooth adhesive organs in stick insects: pads are mechanically anisotropic and softer towards the adhesive surface. J Comp Physiol A 194, 373-384.

Seok, S., Wang, A., Chuah, M.Y., Hyun, D.J., Lee, J., Otten, D.M., Lang, J.H., Kim, S., 2015. Design Principles for Energy-Efficient Legged Locomotion and Implementation on the MIT Cheetah Robot. IEEE/ASME Transactions on Mechatronics 20, 1117-1129.

Shi, X., Polycarpou, A.A., 2005. Adhesive transition from noncontacting to contacting elastic spheres: extension of the Maugis–Dugdale model. Journal of Colloid and Interface Science 281, 449-457.

Shull, K.R., Creton, C., 2004. Deformation behavior of thin, compliant layers under tensile loading conditions. Journal of Polymer Science Part B: Polymer Physics 42, 4023-4043.

Sitti, M., Fearing, R.S., 2003. Synthetic gecko foot-hair micro/nano-structures as dry adhesives. Journal of Adhesion Science and Technology 17, 1055-1073.

Spolenak, R., Gorb, S., Arzt, E., 2005. Adhesion design maps for bio-inspired attachment systems. Acta biomaterialia 1, 5-13.

Spuskanyuk, A.V., McMeeking, R.M., Deshpande, V.S., Arzt, E., 2008. The effect of shape on the adhesion of fibrillar surfaces. Acta biomaterialia 4, 1669-1676.

Vajpayee, S., Long, R., Shen, L., Jagota, A., Hui, C.-Y., 2009. Effect of Rate on Adhesion and Static Friction of a Film-Terminated Fibrillar Interface. Langmuir 25, 2765-2771.

Varenberg, M., Gorb, S., 2007. Shearing of fibrillar adhesive microstructure: friction and shear-related changes in pull-off force. Journal of The Royal Society Interface 4, 721-725.

Yao, H., Gao, H., 2006. Mechanics of robust and releasable adhesion in biology: Bottom–up designed hierarchical structures of gecko. Journal of the Mechanics and Physics of Solids 54, 1120-1146.

Yoon, H., Kwak, M.K., Kim, S.M., Sung, S.H., Lim, J., Suh, H.S., Suh, K.Y., Char, K., 2011. Polymeric Nanopillars Reinforced with Metallic Shells in the Lower Stem Region. Small (Weinheim an der Bergstrasse, Germany) 7, 3005-3010.

Yurdumakan, B., Raravikar, N.R., Ajayan, P.M., Dhinojwala, A., 2005. Synthetic gecko foot-hairs from multiwalled carbon nanotubes. Chemical Communications, 3799-3801.

Zienkiewicz, O.C., Taylor, R.L., 2000. The Finite Element Method: Solid mechanics. Butterworth-Heinemann.